공학박사 학위논문

쇄빙패턴과 빙-선체 접촉조건을 고려한 빙저항 추정기법 연구

Ice Resistance Prediction Method Based on Icebreaking Pattern and Ice-Hull Contact Conditions

지도교수 최 경 식

2016년 2월

한국해양대학교 대학원

해양공학과

정 성 엽

본 논문을 정성엽의 공학박사 학위논문으로 인준함.

위원장 : 공학박사 서 영 교 (인)

위 원 : 공학박사 남 종 호 (인)

위 원 : 공학박사 김 문 찬 (인)

위 원 : 공학박사 김 현 수 (인)

위 원 : 공학박사 최 경 식 (인)

2016년 2월

한국해양대학교 대학원

해양공학과

정 성 엽

쇄빙패턴과 빙-선체 접촉조건을 고려한 빙저항 추정기법 연구

정 성 엽

한국해양대학교 해양공학과

공학박사 학위논문

초 록

평탄빙에서 선박의 저항은 설계 관점에서 매우 중요한 관심 사항이다. 따라서 빙-선체 상호작용과 쇄빙패턴, 압력-면적 효과를 포함하는 다양한 연구들이 수행되고 있으며, 선박에 작용하는 빙저항을 추정하기 위해 다양한 준 경험적 또는 해석적 방법들과 수치모델들이 개발되고 있다.

본 연구에서는 빙-선체 상호작용 현상에 관한 연구와 함께 쇄빙패턴과 빙-선체 접촉조건을 고려한 빙저항 추정용 수치모델을 개발하였다. 선형과 선속, 빙특성을 고려한 쇄빙패턴 특성이 분석되었고 빙-선체 충돌 시 삼각형 충돌과 다각형 충돌 같은 두 가지 빙-선체 접촉조건이 고려되었다. 또한 충돌에 따른 수직 관입변위는 관입에너지와 운동에너지와의 관계를 통해 계산되었다.

수직한 방향의 접촉력을 계산하기 위해 압력-면적 효과가 적용되었고 압력-면적 효과식에 사용되는 변수들은 2010년 북극 보퍼트해에서

쇄빙연구선 아라온호의 실선 빙하중 계측자료를 바탕으로 도출되었다. 빙판의 파괴기준을 정의하기 위해 빙판은 탄성기초 위 반무한평판으로 고려되었고 빙판의 파괴를 위한 최대하중이 정의되었다. 또한 수치모델에서는 선박의 운동과 빙저항 특성을 해석하기 위해 수치적분법이 적용되었다. 특히 개발된 모델을 통해 추정된 빙저항 결과는 모형시험 결과와 비교 시 비교적 우수한 상관성을 나타내었다.

본 연구에서 도출된 기법은 선박의 설계단계에서 선박의 빙성능과 빙저항 추정을 위한 연구에 활용이 가능하며, 개발된 수치모델은 선박해양플랜트연구소 빙해수조에서 다양한 빙상환경에 따른 선형을 고려한 선박의 초기 빙저항 추정 연구에 기여할 수 있을 것으로 판단된다.

검색어: 평탄빙에서의 저항 Resistance in Level Ice; 빙-선체 상호작용 Ice-Hull Interaction; 쇄빙패턴 Icebreaking Pattern; 압력-면적 효과 Pressure-Area Effect; 수치모델 Numerical Model

Ice Resistance Prediction Method Based on Icebreaking Pattern and Ice-Hull Contact Conditions

by

Seong-Yeob Jeong

Department of Ocean Engineering
Graduate School of Korea Maritime and Ocean University

Thesis submitted for the Degree of
Doctor of Philosophy

Abstract

A ship's resistance in level ice is a fairly significant concern from a design point of view, and thus many types of related research are underway, including studies of ice and hull interaction, icebreaking patterns, and pressure-area effects. Meanwhile, various semi-empirical or analytical methods and numerical models are being developed to predict a ship's resistance in ice.

This study investigates ice-hull interaction phenomena and develops a numerical model that can determine ice resistance based on icebreaking patterns and ice-hull contact conditions. The characteristics of icebreaking patterns for the hull form, ship speed, and ice properties are analyzed, and two ice-hull contact cases are considered: one for triangular and one for quadrilateral crushing during the ice-hull interaction. In addition, normal crushing displacement is

calculated based on the relationship between indentation energy and kinetic energy.

To calculate normal contact force, the pressure-area effect is applied and parameters used in the pressure-area equation are selected based on the full-scale ice load measurement results of the Korean icebreaker Araon, which operated in the Beaufort Sea in 2010. To determine the failure criteria of ice, an ice sheet is assumed to be a semi-infinite plate on an elastic foundation. The maximum load at which the ice fails is then determined. In the numerical model, a numerical integration method is used to analyze the ship's motions and the ice resistance characteristics. The predicted results from this model are compared with the model test results, showing relatively good correlation regarding the prediction of ship resistance in level ice.

The presented method should be useful for future studies of ship performance in ice and ice resistance prediction at the design stage of a vessel. In addition, the developed numerical model can contribute to the Korea Research Institute of Ships and Ocean Engineering (KRISO) ice tank, by helping to predict the preliminary ice resistance of vessels, given various ice conditions and hull forms.

KEY WORDS: Resistance in Level Ice; Ice-Hull Interaction; Icebreaking Pattern; Pressure-Area Effect; Numerical Model

감사의 글 (Acknowledgements)

우선 본 논문을 마칠 수 있도록 지혜와 능력주신 하나님께 감사드립니다.

학부과정부터 극지공학연구실에서 다양한 연구를 수행할 수 있도록 지원해 주시고 학위논문 작성 시 주제 선정과 함께 보다 정확한 결과를 도출할 수 있도록 연구 방향에 관해 많은 조언을 해주신 최경식 지도 교수님께 진심으로 감사의 말씀을 드립니다. 특히 연구자로서의 기본자세와 빙역학 분야의 연구 기반을 다져주신 점 가슴 속 깊이 감사드립니다. 또한 논문심사와 함께 연구 내용에 관해 값진 조언을 주신 해양공학과 서영교 교수님, 조선해양시스템공학부 남종호 교수님, 부산대학교 조선해양공학과 김문찬 교수님, 인하공업전문대학 조선해양과 김현수 교수님께도 진심으로 감사의 말씀을 드리며, 대학원 수학기간 동안 학사업무를 도와준 천은지 박사과정을 비롯한 극지공학연구실원들에게도 감사의 마음을 전합니다.

대학원 수학기간 동안 전공분야에 대한 많은 가르침을 주신 해양공학과 박한일 교수님, 김재수 교수님과 조선해양시스템공학부 현범수 교수님, 조효제 교수님께도 진심으로 감사의 말씀을 드립니다.

연구소 입소 후 대학원 박사과정에 진학할 수 있도록 배려를 해주신 김기섭 박사님, 반석호 박사님, 이동곤 박사님, 이경중 박사님, 안종우 박사님, 문일성 박사님, 김 진 박사님, 안해성 박사님, 박철수 박사님, 김광수 박사님을 비롯한 미래선박연구부 여러 선배님들께도 진심으로 감사의 말씀을 드립니다.

빙해수조에 근무하면서 많은 조언과 격려를 해주신 강국진 박사님, 이춘주 박사님, 이창용 책임기술원께도 진심으로 감사의 말씀을 드리며, 추운환경에서 모형시험을 준비하고 도와준 염종길 선임연구원, 오은진 연구원, 후배 하정석 연구원에게도 감사의 인사를 드립니다.

빙해선박의 모형시험 및 해석에 관해 많은 조언을 주신 현대중공업 선박성능연구실 박경덕 수석께도 진심으로 감사의 말씀을 드립니다.

끝으로, 저를 위해 항상 기도해 주시는 부모님께 진심으로 감사의 말씀을 드리며, 타국에 있어 자주 만나지는 못하지만 항상 학구적인 모습으로 저에게 좋은 본보기를 보여주신 누나에게도 감사의 말씀을 드립니다. 또한 논문작성 기간 동안 저를 응원해주고 믿어준 아내와 사랑스런 딸 유림에게도 감사의 마음을 전합니다.

2016년 1월 15일

대전 연구실에서

정 성 엽

Table of Contents

List of Tables

List of Figures

Nomenclature

R_{tot}	Total resistance in ice
R_{ice}	Ice resistance
R_{ow}	Open-water resistance
$T_{net}(v)$	Net thrust
$T_{tot}(v)$	Total thrust
t	Thrust deduction
V, v	Ship speed
v_{ow}	Maximum ship speed in ice-free condition
T_{pull}	Thrust at bollard condition
l	Breaking radius
h, h_i	Ice thickness
$\overline{h}$	Empirical constant in icebreaking pattern
l_c	Characteristic length of ice
E	Elastic modulus of ice
ρ_w, ρ_s	Density of water and solution
g	Acceleration gravity
C_l, C_v	Empirical parameters in icebreaking radius
v_n^{rel}	Relative normal velocity
D, l_{cusp}	Ice cusp depth
C_1, C_2, $\widehat{C}_1$, $\widehat{C}_2$	Empirical constants in ice cusp depth
k'	Proportionality constant in ice cusp depth
l_{water}	Waterline length from the bow to the maximum beam breadth
$l_{water,seg}$	One waterline segment length
$n_{ice\ cusps}$	The number of ice cusps

l_{br}	Breaking length in forward direction
A, b_0, h_c, θ, $\overline{AA'}$, d_c, ϕ, R_1, $\overline{OC'}$, c, B	Contact area calculation parameters as shown in Figure 18
A_c, t_c, θ_c, θ_s, θ_{wf}, θ_{wb}	Contact area calculation parameters as shown in Figure 19
A_c, L_h, L_c, ϕ	Contact area calculation parameters as shown in Figure 20
$\breve{A}$, $\breve{\alpha}$, x, y	Contact area calculation parameters as shown in Figure 21
ζ_{n_i}, ϕ_i, β_i, α_i	Normal crushing displacement, buttock angle, frame angle, and waterline entrance angle at the $i-th$ contact point
n_1, n_2, n_3	Direction cosines in x, y, and z directions
F_n	Normal contact force
σ_c	Uniaxial crushing strength of ice
A_n	Normal contact area
p_0, A_0	Reference pressure and area
k, e	Parameters in pressure-area effect
M_e	Equivalent mass of the ship
V_n	Normal velocity at the impact point
M_x, M_y, M_z, j_{xx}, $j_{yy,}$ j_{zz}	Added mass in surge, sway, heave, roll, pitch, and yaw
R_{xx}^2, R_{yy}^2, R_{zz}^2	Mass radii of gyration in roll, pitch, and yaw
l, m, n	Direction cosines
λl, μl, ηl	Moment arm in roll, pitch, and yaw
C_o	Mass deduction coefficient
T, B, L	Ship draft, breadth, and length
C_{wp}	Water plane coefficient
C_b	Block coefficient
C_m	Midship section coefficient
β'	Normal frame angle
F_x, F_y, F_z	Force components in x, y, and z directions

F_X, F_Y, F_Z	Total force components in x, y, and z directions
μ	Frictional coefficient between the hull surface and the ice
P_f	Failure load
θ	Opening angle of the ice wedge
C_f	Empirical parameter in failure load
S_N	Strength number
F_N	Froude number
σ_f	Flexural strength of ice
ρ_i	Ice density
$P_{\max}$	Maximum load
R_b	Crushing and breaking components
R_s	Submersion component
h_{tot}	Total ice and snow thickness
$[M]$, $[A]$, $[C]$, $[K]$	Mass, hydrodynamic added mass, ,damping and hydrostatic resorting matrices
$\{\ddot{x}(t)\}$, $\{\dot{x}(t)\}$, $\{x(t)\}$	Acceleration, velocity, and displacement vectors
$\{F(t)\}$	Excitation force vector
F_X^i, F_Y^i, M_N^i	Forces and moment in ice
c_1, c_2	Coefficients in numerical integrating
$\lfloor \overline{M} \rfloor$	Effective mass matrix
P, L', w	Failure load, length of beam and width of beam
ν	Poisson's ratio
k''	Specific weight of water
$\triangle P$	Deviation of load
$\triangle\omega$	Deflection
γ	Euler constant
W_i, $W_{\triangle w}$	Model ice weight and weight of excreted solution
F_μ	Friction force

N	Normal load
W	Weight of ice
P_D	Delivered power
η_D	Propulsion efficiency in ice
n	Propeller revolution
Q	Propeller torque
a, b	Parameters in correction formula
$R_{i,meas}$, $R_{i,corr}$	Measured and corrected ice resistance
$H_{i,meas}$, $H_{i,target}$	Measured and target ice thickness
x	Exponent in correction formula
$\sigma_{f,target}$, $\sigma_{f,meas}$	Target and measured flexural strength of ice
T	Propulsion thrust
TF	Towed force
T_{meas}, TF_{meas}, $P_{D,meas}$	Measured propulsion thrust, towed force, and delivered power
T_{corr}, TF_{corr}, $P_{D,corr}$	Corrected propulsion thrust, towed force, and delivered power
λ	Scale ratio
R^{level}	Level ice resistance
$R^{pre-sawn}$	Pre-sawn ice resistance
δ	Deviation
$R^1_{predictions}$	Predictions derived from the present model
$R^2_{predictions}$	Predictions derived from the Lindqvist's model
$R_{measured}$	Ice model test results

Chapter 1 Introduction

1.1 Objectives

In recent years, the summer melt season for the Arctic Ocean has begun earlier than in past decades and the sea ice extent has been declining. These phenomena allow increased transit between Europe and Asia using the Northern Sea Route (NSR) for Arctic-going vessels. In particular, Russian authorities have issued permits to 652 ships for NSR transit voyages in 2015 (www.nsra.ru), a slight increase over last year. This tendency is expected to increase for the time being.

To increase the efficiency of ship performance in ice-covered waters, optimizing hull forms and propulsion systems is the most important concern. Ship performance in ice is related to propulsion efficiency and ice resistance. In particular, the magnitude of ice resistance resulting from icebreaking process play a major role in determining of propulsion power. Determining ice resistance is more complicated than determining open-water resistance because of the properties of ice and ice-hull interaction phenomena. In addition, predicting ship resistance in level ice is a fundamental research area to evaluate ship performance in ice. Therefore, many researchers have focused on ice–hull interaction to better understand icebreaking phenomena.

To ensure the ice navigation of a vessel in actual service conditions, propulsion power and ice resistance should be determined at the design stage of a vessel. In such situations, model/full-scale data can provide important information for the hull form development and the required propulsion capacity. The data obtained from full-scale ice field trials will be useful, but field trials present several technical problems in gathering ice properties and data synchronization. Therefore, a model-scale test in an ice tank could be an alternative approach for obtaining required information.

Empirical and analytical approaches can provide valuable information in relation to various ice conditions and ship particulars. Recently, numerical simulation models have been also investigated and can give a quantitative value for the prediction of ice resistance (e.g. Valanto, 2001; Liu et al., 2006; Martio, 2007; Su et al., 2010; Aksnes, 2010; Sawamura et al., 2010; Lubbad and Loset, 2011; Zhou et al., 2013; Tan et al., 2013; Erceg et al., 2014). However, empirical parameters in the model or model/full-scale results are needed to improve the degree of accuracy for these approaches.

The objectives of the thesis are to investigate the icebreaking phenomena and to predict the ice resistance of a vessel in level ice conditions. The numerical model for predicting ice resistance is developed. In the present study, the author clarifies ice-hull contact conditions and icebreaking patterns during the ice-hull interaction process. The characteristics of icebreaking patterns for the hull form, ship speed, and ice properties are analyzed, and two ice-hull contact conditions are considered. In particular, new semi-empirical icebreaking patterns are derived from the model test results in the ice tank of the Korea Research Institute of Ships and Ocean Engineering (KRISO), and the pressure-area effect is considered to calculate the normal contact force. A revised failure criterion of ice sheets is defined in this study. Using the numerical model, ship resistance components in ice are calculated, and the results are compared with those of experimental tests in the KRISO ice tank.

Defining the icebreaking pattern and the parameters used in this study will be useful for future studies of ship performance in ice. The detailed procedures of the model test can also help in analyzing the model test results. In addition, the developed numerical model enables us to predict ice resistance in the design stage of ice-going vessels with various ice conditions and hull forms.

1.2 Approaches and Methodology

To understand the icebreaking phenomena, ice-hull interactions are investigated, and icebreaking patterns are determined. In particular, this study discusses the relationship between the depth of ice cusps and the ratio of the characteristic length of ice and the ship speed.

Regarding ice-hull contact conditions, two cases are considered—one for triangular crushing and one for quadrilateral crushing. Normal crushing displacement is calculated based on the relationship between indentation energy and kinetic energy. To calculate contact forces, the pressure-area relationship is applied. Parameters of the pressure-area formula are selected based on the full-scale ice load measurement of the Korean icebreaker, Araon that operated in the Beaufort Sea in 2010.

To determine the failure criteria of ice, an ice sheet is assumed to be a semi-infinite plate on an elastic foundation, and the relationship between the strength number and the Froude number is considered to determine the maximum load at which the ice fails. To analyze the ship motions and the ice resistance characteristics during ice-hull interaction, a numerical integration method called the Newmark-β method is applied.

1.3 Organization of Thesis

The remainder of this thesis is organized as follows. In Chapter 2, a literature review on the various empirical, analytical and numerical approaches is provided and the main concept for predicting ice resistance is discussed.

In Chapter 3, the icebreaking patterns and the ice-hull contact conditions are introduced, and contact force is calculated based on the pressure-area effect. The failure criterion of ice is defined to determine the icebreaking phenomena. In the calculation of ship resistance in ice, a submersion component is calculated based on the Lindqvist formula, whereas the crushing and breaking components are calculated based on the model developed in this study.

In Chapter 4, the experimental test concepts, detailed procedures and results are described. The ice model tests were conducted in the KRISO ice tank to determine ice resistance. In particular, towed propulsion tests were conducted. The ice model test results are compared with the calculated results derived from the developed model in order to evaluate the degree of accuracy and application probability.

In Chapter 5, conclusions and recommendations for further study are provided.

Chapter 2 Reviews on Ice Resistance Prediction

As mentioned, the prediction of icebreaking performance and resistance in level ice is important. Therefore, many researchers have focused on ice-hull interaction to understand the icebreaking phenomena. Empirical, analytical, and numerical approaches have been used to determine the resistance of ships in ice.

2.1 Empirical and Analytical Approaches

Kashteljan et al. (1968) described a detailed empirical formula to analyze the level ice resistance from the model/full-scale data for the Ermak. They separated ship resistance in ice into several components based on some physical background information.

Lewis and Edwards (1970) established an ice resistance prediction formula composed of three aspects—icebreaking and friction, ice buoyancy, and momentum interchange between ship and broken ice pieces. They presented empirical parameters for the equation based on full/model-scales data. White (1970) proposed a analytical model and an efficient bow form for polar icebreakers. In particular, White's bow form was used in the design stage of the Manhattan. Enkvist (1972) developed a semi-empirical formula based on an analytical approach, dimensional analysis, and assumptions. He also proposed a pre-sawn ice test technique in 1983. Based on this concept, breaking component in terms of total resistance in ice can be estimated. He obtained that the breaking term was very important parameter in the full-scale condition. Milano (1973) derived a theoretical ice resistance prediction formula based on a Lagrangian approach. He separated the total energy as five terms: E_1, transit through broken ice; E_2, impact and breaking of ice; E_3, hull motion through ice; E_4, hull falling through ice; and E_5, ice submergence. This analytical approach was compared with full-scale data for the Mackinaw. In addition, he defined the icebreaking pattern during ice-hull interaction. Vance (1975) proposed an empirical formula based on the five full/model-scales datasets for the Mackinaw, the Moskva, the Finncarrier, the Staten Island, and the Ermak. The empirical formula consisted of three parts—submergence, breaking and velocity. Edwards et al. (1976) presented a non-dimensional equation based on the full-scale ice trial data for the Louis S. St. Laurent.

Kotras et al. (1983) proposed a semi-empirical formula and icebreaking pattern. In his approach, four empirical coefficients in the formula were determined from the full-scale data for the Katmai Bay, the Mackinaw, the Radisson, the Staten Island, and the Manhattan. Lindqvist (1989) presented a relatively simple analytical model consisting of main dimensions, hull form, ice thickness, ice strength, and friction. The wedged bow shape was considered and the ice resistance was divided into three categories—crushing, breaking, and submersion. Lindqvist's model assumed that the ice resistance increased linearly with the ship speed and the empirical constants in the velocity term were used for calculate the total ice resistance. Riska et al. (1997) investigated the prediction of ice resistance. The formulation of ice resistance was based on the studies of Ionov and Kämäräinen (1988, 1993 cited in Riska et al., 1997), and Lindqvist (1989). The empirical coefficients in this model were derived from the full-scale data of a number of ships in the Baltic Sea. The concept of energy consideration has also been studied to estimate the collision force. Daley (1999) considered the relationship between indentation energy and kinematic energy and proposed different analytical formulas to calculate ice collision force. This method is able to predict the ice force for several geometric contact cases.

Spencer and Jones (2001) investigated a method to predict ice resistance and proposed the component-based ice resistance prediction method. They derived the total ship resistance into four components: open-water resistance; ice buoyancy resistance; ice clearing resistance; ice breaking resistance. Especially, the ice breaking component of the total ice resistance can be obtained by subtracting the resistance in pre-sawn ice from the total ice resistance. This method is used in the National Research Council of Canada-Ocean, Coastal, and River Engineering (NRC-OCRE, formerly NRC-IOT) ice tank to determine ice resistance for model-scale and full-scale icebreaking vessels.

2.2 Numerical Approaches

Recently, numerical models have been introduced to evaluate ship performance in ice. These models estimated ice force and resistance during ice-hull interaction in the time domain. Valanto (2001) proposed a 3-D numerical simulation model based on the semi-empirical model of Lindqvist (1989). This model can predict the forces that affect ice-hull interaction at a ship's waterline and simulate the response of the floating ice cover and the surrounding fluid to an advance of the icebreaking vessel. The results obtained using the developed model were compared with the results obtained for the icebreaker Otso.

Liu et al. (2006) introduced a mathematical model to simulate a ship's maneuvering performance in ice. In this model, the ice forces were breaking force, buoyancy force, and clearing force and were calculated using the linear sum of the force components. The ice crack pattern was based on Kotras et al. (1983). The results were compared with the model test results of NRC-IOT to verify the developed model.

Martio (2007) presented a numerical simulation model to predict ship's maneuvering performance in uniform ice conditions. The theoretical background was based on Lindqvist's model, but this model was expanded to 3-D. The forces were composed of hydrodynamic force, hull force due to ship motion, and ice force in this model. The number of ice cusps and length were considered. The simulated results were compared with the model test results of MT Uikku and USCGC Mobile Bay to validate the developed model.

Su et al. (2010) also introduced a 3-degree of freedom (DOF) numerical model based on Lindqvist's model. This model can simulate both continuous ice forces and ship motions. The ice-hull contact area was determined to estimate the ice-breaking forces. They considered rudder and propeller force, hydrodynamic force, and ice force in the ice resistance calculation. In addition, the icebreaking pattern were similar to those in Wang (2001). In this model, the icebreaking pattern was sensitive to ice thickness. To determine the failure load Kashtelian's work was applied and the empirical constant in the failure load formula derived from the results of Lindqvist's model. To validate the numerical results, full-scale ice trial data for the Tor Viking II were used.

Aksnes (2010) developed a one dimensional mathematical model to estimate the response of moored ships in level ice conditions with a constant drift direction. In particular, this model dealt with the surge response of a vessel in the interaction between the moored ship and drifting level ice. They considered the hydrodynamic, mooring and, ice forces. In particular, hydrodynamic forces were derived from potential theory, but the mooring force was assumed to be a proportional to surge motions and ice force was composed of breaking, rotating and sliding terms. To calculate the deflection of the ice during the penetration process, ice sheet was assumed a semi-finite elastic beam on the elastic foundation.

Sawamura et al. (2010) presented a numerical method to calculate the ice load acting on a ship during maneuvering in level ice. A 3-DOF equation was applied to describe the ship motions. In this model, a circle contact algorithm was applied to determine the contact position during ice-hull interaction, and circular arc cusps were adopted. The ice breaking force was calculated from the numerical resulted in FE fluid-structural interaction and ship maneuvering with the ship moving ahead was simulated.

Lubbad and Løset (2011) introduced a numerical model that can determine ship performance in ice. They only considered two ice conditions—level and broken ice. In addition, failure criterion for a semi-infinite plate resting on elastic foundation was considered, and the icebreaking process consisted of circumferential and radial cracks. This model composed of two modules-rigid body motion module and ice breaking module. The former module calculated the response of the unbreakable ice floes and ship motions, and latter module calculated the contact force between the breakable floes and the ship's hull. The deflection and maximum bending stress were derived from the new analytical closed form solution.

Zhou et al. (2013) presented a simulation model to predict the dynamic ice loads acting on an icebreaker in level ice. An ice accumulation process was considered, and the total force consisted of restoring force, drag force, icebreaking force, and submersion force. A comparison of the results from the numerical simulations and the ice tank tests was performed to validate the developed model.

Tan et al. (2013) introduced a numerical model to simulate ice-hull interaction. The main frame of this model was based on Su et al. (2010), and Wang's (2001) failure criterion was adopted. However, this model extended one by Su et al. (2010) to a 6-DOF model, and the icebreaking pattern was idealized based on Milano (1973). The pressure-area effect was considered to calculate the contact force. Moreover, interaction between ship motion and the icebreaking pattern was investigated.

Erceg et al. (2014) developed a quasi-static numerical model to simulate the icebreaking pattern in level ice. They focused on an icebreaking pattern based on circumferential crack formation. A discretized level ice sheet was used to simulate the irregular ice cusp shape, and ice sheets were assumed a semi-infinite beam on elastic foundation. In this model, the failure criterion was the flexural strength of ice; therefore, when the maximum bending stress reached the bending failure criterion, the ice beam failed. However, this model did not include ship motion in the simulation.

Based on the literature reviews on the ice resistance prediction, the following conclusions can be drawn:

1) Generally, ship resistance in ice can be composed into two terms. The velocity-independent term includes the fracture portion and gravity portion, and the velocity-dependent term includes the inertia portion.

2) During a continuous icebreaking process, an icebreaking pattern may develop around the vessel's waterline, related to ice wedge formation and consisting of radial and circumferential cracks; it can affect the failure criteria of ice during the contact between ice and ship. These ice failure phenomena can have a significant effect on ship resistance in ice. In particular, the icebreaking pattern can be strongly affected by ice thickness and ship speed; therefore, this relationship should also be investigated.

3) The breaking resistance term comprises a large proportion of the total resistance in ice. Accordingly, the breaking resistance is the most significant parameter in ice resistance prediction. Recently, the hull form of icebreaking vessels has become more diverse in terms of efficient icebreaking performance. As a result, the hull form should be considered in the calculation of the breaking resistance.

4) To understand the icebreaking phenomena, failure criteria of ice during ice-hull interaction should be determined, and the beam or plate theory can be applied to derive the failure stress. When calculating the contact force, the uniaxial compressive strength of ice should be considered, but this concept is quite a rough approach to modeling crushing pressures. Therefore, the pressure-area effect can be used as an alternative approach. In such cases, full-scale ice trial data is needed to define the pressure-area effect. Moreover, the contact area should be determined to calculate contact force during ice-hull contact.

Chapter 3 Development of Ice Resistance Prediction Model

3.1 Ship Resistance in Ice

When a ship navigates ice-covered waters, ice resistance occurs at the bow, stern and sides due to the interaction between the ship's hull and ice (see Fig. 1). Therefore, ship performance in ice is influenced by these phenomena. Ship performance in ice is a critical concern of shipbuilders, and thus many researchers have focused on ice-hull interaction to determine ice resistance and to provide important background information for ship designers.

Full-scale ice trials with ice-going vessels provide opportunities to determine ship performance in ice, but ice trials do not allow direct measurement of ice resistance. Therefore, ship resistance in ice can be inferred from the measurement of ice conditions, ship speed, shaft thrust, and torque. Model-scale test in ice tank can be an alternative method to predict ice resistance. In addition, model test data provide valuable information about ice resistance under various ice conditions, such as ice thickness and strength. Such data is difficult to obtain from full-scale ice trials of vessels.

The total resistance in ice is the sum of two components, open-water resistance and ice resistance (ITTC, 2005). In particular, open-water resistance can be determined using a towed model test in calm water, and ice resistance can be determined by subtracting the open-water resistance from total resistance in ice. The total resistance in ice can be determined as

$$R_{tot} = R_{ice} + R_{ow} \tag{1}$$

where R_{tot} is total resistance in ice, R_{ice} is ice resistance, and R_{ow} is open-water resistance.

The ice resistance is equal to the thrust available to overcome design conditions, such as design speed and ice conditions, and does not include the hydrodynamic resistance associated with open-water resistance, $R_{ow}(v)$. Therefore, the net thrust, $T_{net}(v)$, can be defined as (Juva and Riska, 2002):

$$T_{net}(v) = T_{tot}(v)(1-t) - R_{ow}(v) \tag{2}$$

where $T_{tot}(v)$ is the total thrust and t is the thrust deduction. The thrust deduction is taken into account using the thrust deduction fraction.

The net thrust can be calculated as a function of ship speed using estimated bollard thrust (Riska et al., 1997):

$$T_{net}(v) = T_{pull}\left(1 - \frac{v}{3v_{ow}} - \frac{2}{3}\left(\frac{v}{v_{ow}}\right)^2\right) \tag{3}$$

where v and v_{ow} are the ship speed and maximum ship speed in ice-free conditions, respectively, and T_{pull} is the thrust at bollard conditions. When the ship speed is zero, the net thrust is equal to bollard pull (see Fig. 2).

In previous studies, ice resistance is often discussed by dividing it into components, such as direct resistance which is independent of speed, and velocity-dependent resistance. Direct resistance consists of the fracture portion due to breaking ice and the gravity portion due to ice buoyancy. Velocity-dependent resistance is the inertia force due to clearing ice. The breaking resistance comprises a large proportion of total resistance in ice; thus, the breaking resistance is the most significant parameter in predicting ship resistance in ice.

The interaction between ship hull and ice is a critical parameter in calculating the crushing and breaking components. This process involves a combination of ice crushing and shearing until sufficient contact area is generated to break the ice sheet by flexure and is related to the icebreaking pattern. Therefore, it is necessary to define the icebreaking pattern and contact area between a ice and hull to predict the crushing and breaking components in total resistance.

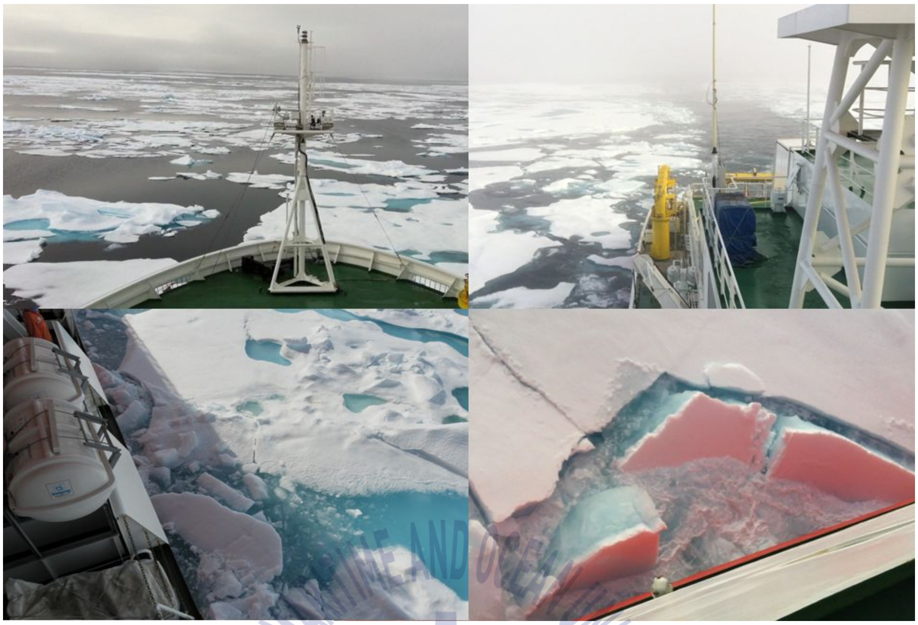

Fig. 1 Ice and hull interaction phenomena of ice-going vessel in the ice-covered waters (photographs by the author)

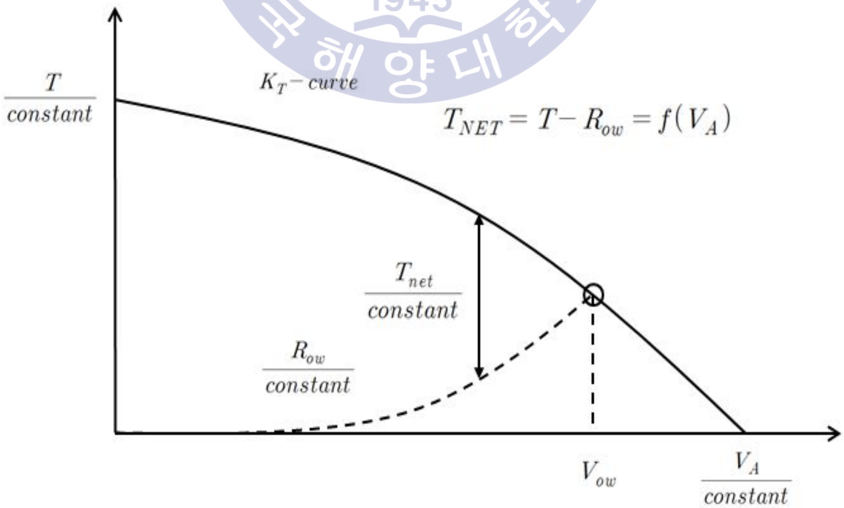

Fig. 2 Definition of net thrust (redrawn form Riska, 1997)

3.1.1 Icebreaking Pattern in Level Ice

Knowledge about icebreaking phenomena during ice-hull interaction can provide important background information for the development of ice resistance prediction model. In particular, defining the icebreaking pattern is a significant parameter in the present study. The icebreaking pattern can be influenced by ice properties and ship speed. Many researchers have idealized the icebreaking phenomena based on a simplified icebreaking process.

Kashteljan (1968) studied the icebreaking pattern around the bow based on field observations of a continuous icebreaking process. The icebreaking pattern is depicted in Fig. 3. Enkvist (1972) defined the icebreaking pattern at the bow area. The icebreaking pattern had a constant radius (l), as shown in Fig. 4. A schematic of the icebreaking pattern based on the results of the model tests and full-scale ice trials was provided. Milano (1973) idealized the icebreaking pattern based on the plate bending theory and field observations and defined the depth and length of ice cusps (see Fig. 5).

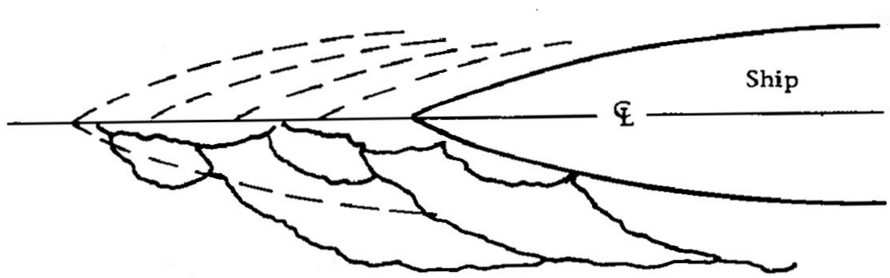

Fig. 3 Idealized icebreaking pattern around the icebreaker bow (Kashteljan, 1968)

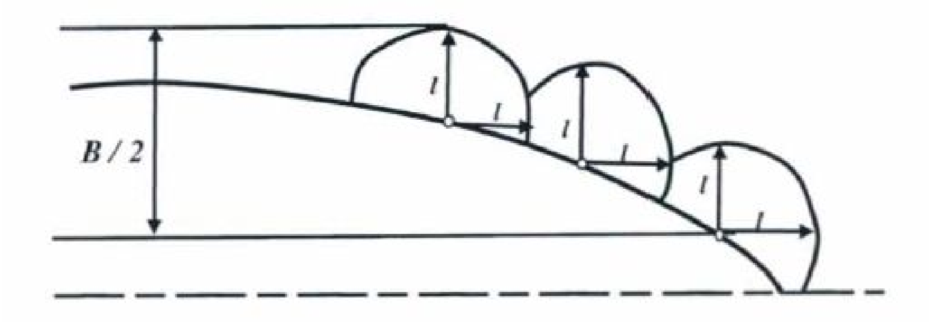

Fig. 4 Schematic icebreaking pattern during ice and ship contact (Enkvist, 1972)

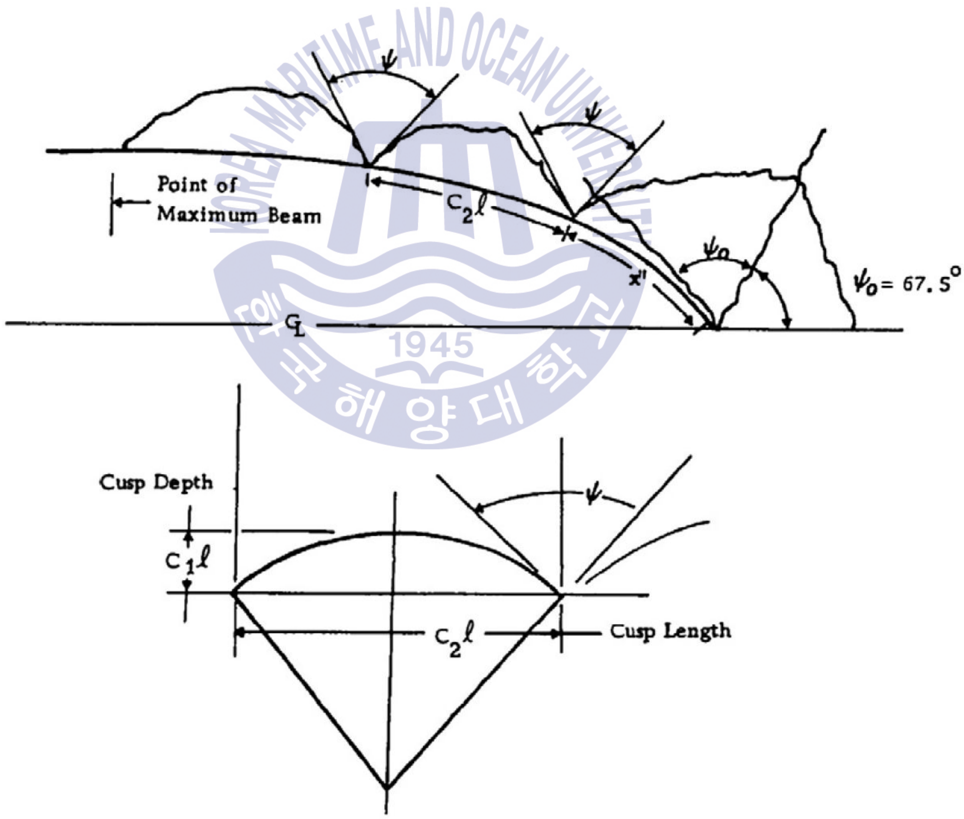

Fig. 5 Idealized ice cusp length and depth (Milano, 1973)

Naegle (1980) investigated the icebreaking patterns produced from full-scale ice trials and derived an empirical equation for the relationship between the depth of ice cusps and the characteristic length of ice. In particular, he assumed that the number of rows of cusps depends on the ice characteristic length, on the hull form, and on the beam (see Fig. 6).

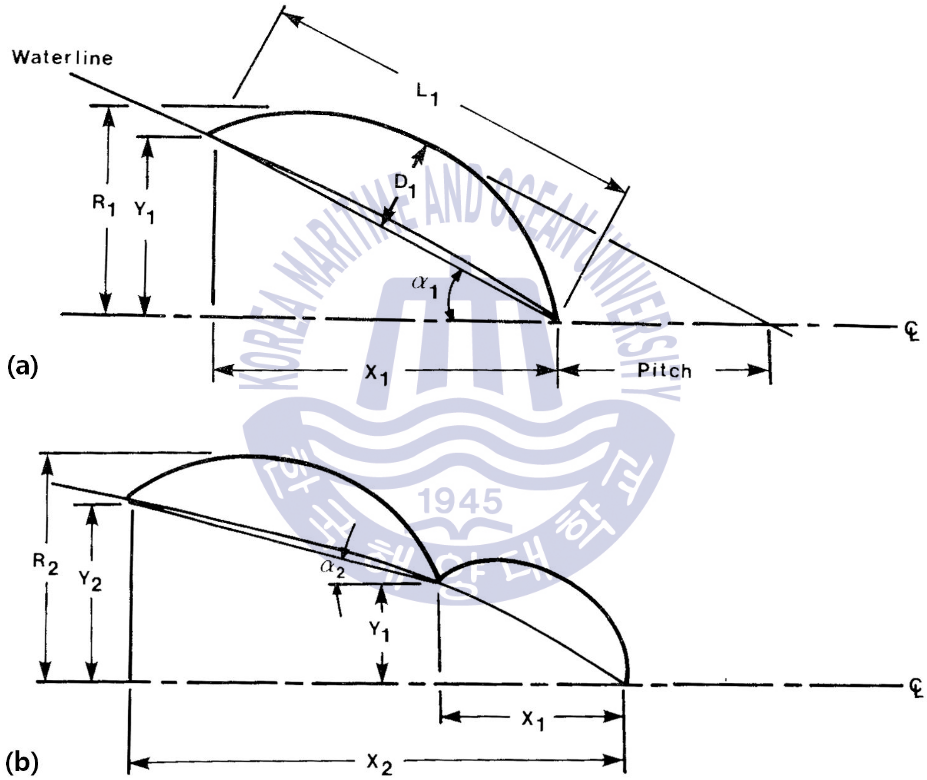

Fig. 6 Idealized breaking pattern for ice; (a) denotes the row 1 breaking pattern, (b) denotes the row 2 breaking pattern (Naegle, 1980)

Kotras et al. (1983) studied the idealization of icebreaking patterns based on full-scale trials and proposed a detailed icebreaking pattern that considered cusp width and ice thickness (See Fig. 7). This relationship can be expressed as follows:

$$\frac{W}{D} = \sqrt{\frac{\bar{h}}{h}} \tag{4}$$

where h is the ice thickness in meters, and $\bar{h}$ is an empirical constant determined from the statistical data of full-scale observations. According to Kotras et al. (1983), $\bar{h}$ is defined as 10.0m.

Fig. 7 Observed ice cusp shape in ice trials (Kotras et al., 1983)

Ettema et al. (1991) discussed the applicability of chaos theory to continuous-mode icebreaking in the model test for the Polar Class icebreaker ship model. The icebreaking pattern is depicted in Fig. 8.

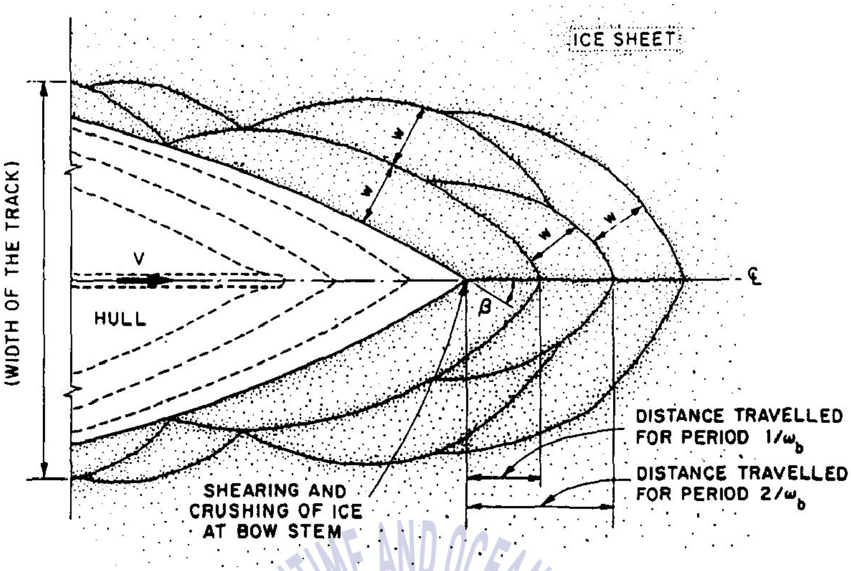

Fig. 8 Schematic icebreaking pattern (Ettema et al., 1991)

Yamaguchi et al. (1997) discussed the ice crack patterns of three different bows in a model test. Figure 9 shows the schematic crack patterns of different ship bows. They determined the relationship between the stem angle and the ice crack pattern and between icebreaking resistance and the ice crack pattern.

Lau et al. (1999) determined the average breaking depth, D, as a function of characteristic length of ice, l_c.:

$$D = 0.2 l_c,\ \ l_c = \sqrt[4]{\frac{Eh^3}{12\rho_w g(1-\nu^2)}} \tag{5}$$

where l_c is the characteristic length of ice. E is the elastic modulus of ice, h is the ice thickness, ρ_w is the density of water, g is the acceleration due to gravity, and ν is the Poisson's ratio.

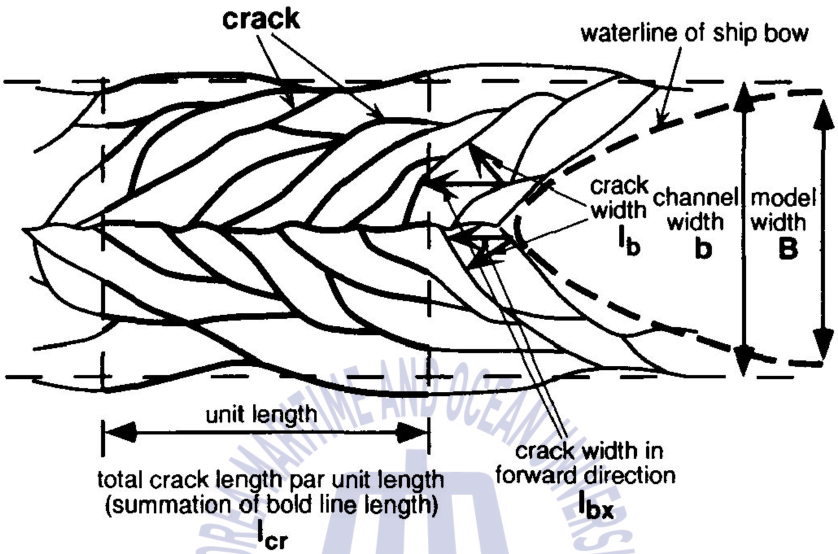

Fig. 9 Schematic icebreaking pattern from the model test (Yamaguchi et al., 1997)

Wang (2001) determined the icebreaking radius based on the bending cracks. The size of cusps was considered to be dependent on speed and the characteristic length of ice (l_c). Su et al. (2010) and Tan et al. (2013) adopted Wang's method. The icebreaking radius is expressed as

$$R = C_l l_c (1.0 + C_v v_n^{rel}) \tag{6}$$

where C_l and C_v are empirical parameters and v_n^{rel} is the relative normal velocity between the ice and hull nodes.

Liu (2009) took into account the ship velocity effect on the icebreaking process based on the results of Varsta (1983), Enkvist (1972), and Yamaguchi et al. (1994). In his study, the ice cusp depth, D, can be expressed as

$$D = \frac{0.2\, l_c}{(C_1 + C_2 V)} \tag{7}$$

where V is the velocity of the ship during the icebreaking process. C_1 and C_2 are two constants determined from the experimental data. C_1 is 0.75 and C_2 is 0.3.

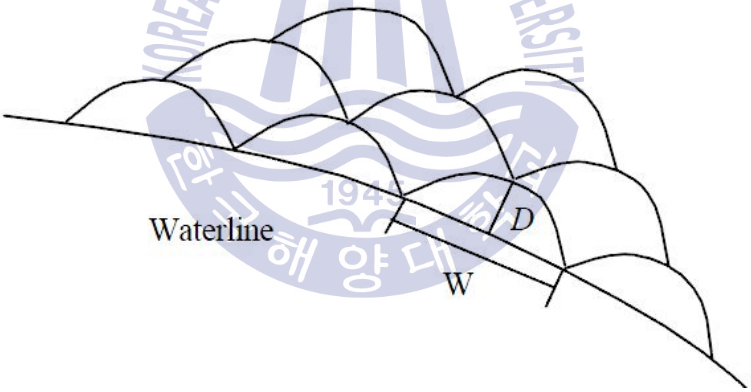

Fig. 10 Schematic ice cusp pattern (Liu, 2009)

Sawamura et al. (2010) developed a numerical method to calculate the ice load of a ship maneuvering in level ice. They proposed an icebreaking process based on the formation of wedge-shaped ice. The broken ice area was assumed to be a circle, and the radius of the broken ice cusp was predicted based on the database of the ice wedge bending problem (see Fig. 11).

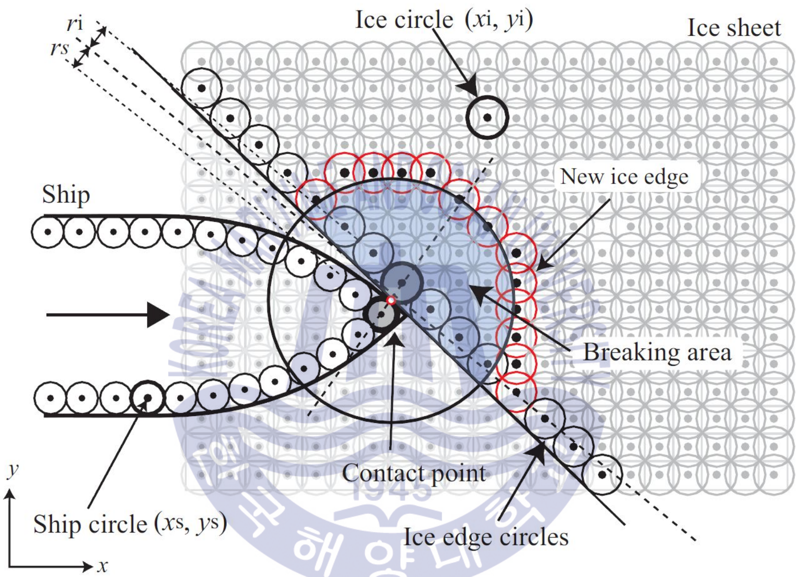

Fig. 11 Schematic circle contact detection (Sawamura et al., 2010)

Lubbad and Løset (2011) determined the cracking pattern during ice-hull interaction. They adopted the theory of a semi-infinite plate resting on an elastic foundation to determine the failure criterion of an ice floe. The maximum bending stresses at the free edge under the loaded area were established in Kerr and Kwak, Wyman and Abramowitz and Stegun (1993, 1950, 1972, cited in Lubbad and Løset, 2011). When these stresses reach the failure criterion, the wedge will be broken. Once a radial crack forms, circumferential cracks will occur (see. Fig. 12).

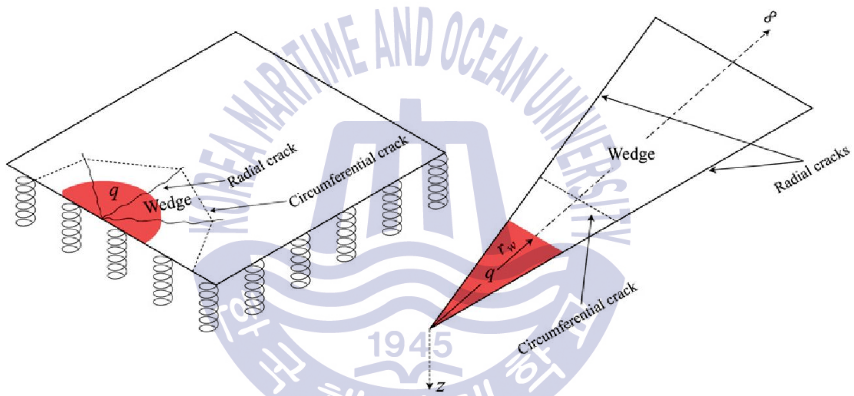

Fig. 12 Idealized ice cracking pattern model (Lubbad and Løset, 2011)

Tan et al. (2013) illustrated the icebreaking pattern, as shown in Fig. 13. Here, ice was discretized into nodes too on the edge based on the shape of the ice edge from the previous time step or any given initial condition.

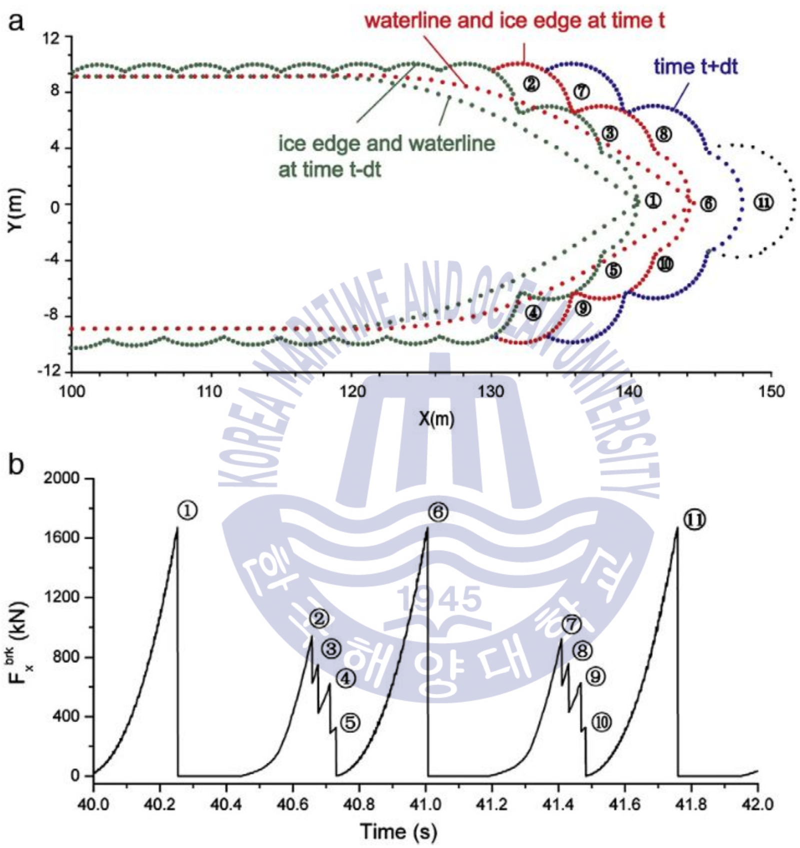

Fig. 13 Process of ice-ship contact and the characteristic breaking force for each contact procedure (Tan et al., 2013)

Erceg et al. (2014) focused on the icebreaking pattern based on the circumferential crack formation. To simulate the irregular shape of ice cusps, a discretized level ice sheet was used. The breaking length was dependent on the ice thickness and elastic modulus of ice in the calculation. Figure 14 shows the ice cusp formation process. A new ice cusp was formed after ice beam failure.

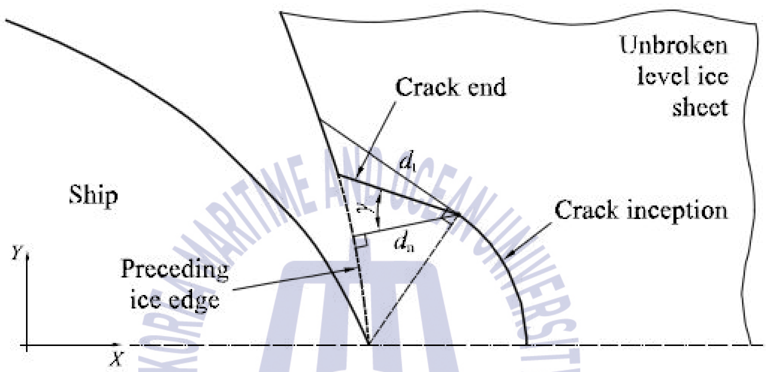

Fig. 14 Ice cusp formation process (Erceg et al., 2014)

In the present study, the semi-empirical icebreaking pattern is derived from the relationship between the characteristic length of the ice, l_c, and the ship speed, v,; thus, the ice cusp depth, D, can be defined as

$$l_{cusp} = \widehat{C_1}\left(\frac{l_c}{v}\right)^{\widehat{C_2}} \tag{8}$$

where l_{cusp} is the depth of ice cusp and parameters $\widehat{C_1}$ and $\widehat{C_2}$ are empirical coefficients derived from the model tests in a ice tank.

The number of ice cusps in the waterline length, l_{water}, from the bow to the maximum beam breadth can be connected to the number of the waterline segment, $l_{water,seg}$; thus, one waterline segment length can be defined as

$$l_{water,seg} = l_{water}/n_{ice\ cusps} \tag{9}$$

In the calculation, the number of ice cusps, $n_{ice\ cusps}$, can vary from 3 to 5. In addition, the breaking length in forward direction, l_{br} can be defined as

$$l_{br} = \frac{l_{cusp}}{\sin\alpha} \tag{10}$$

where α is the waterline entrance angle of the model ship.

The definitions of the ice breaking pattern and the breaking length in this study are depicted in Figs. 15 and 16.

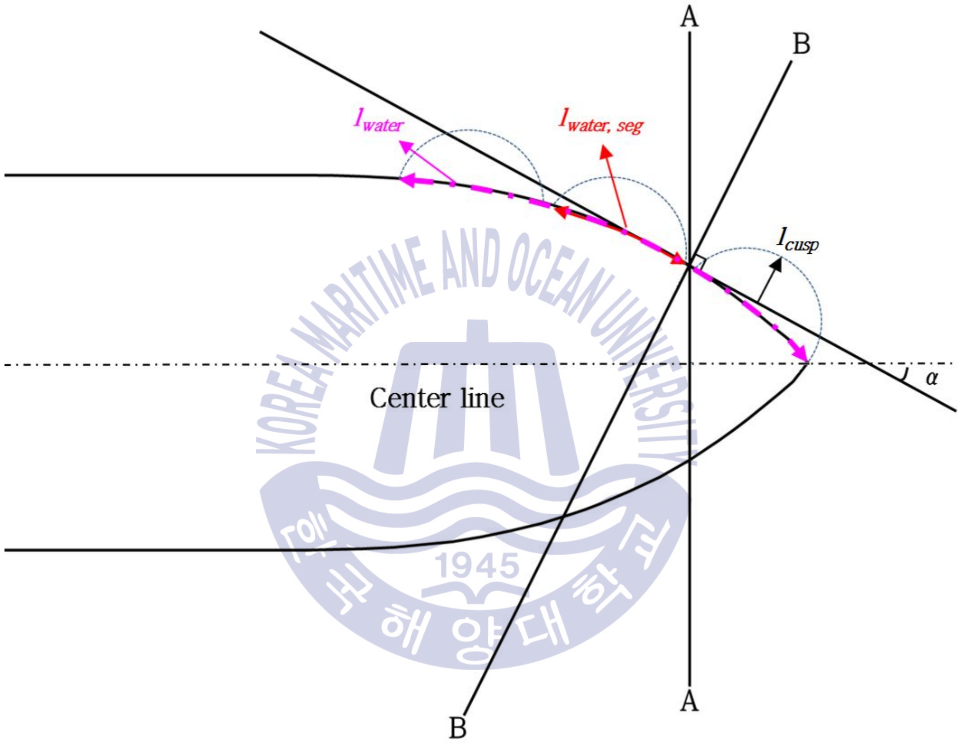

Fig. 15 Idealized icebreaking pattern during ice-ship interaction

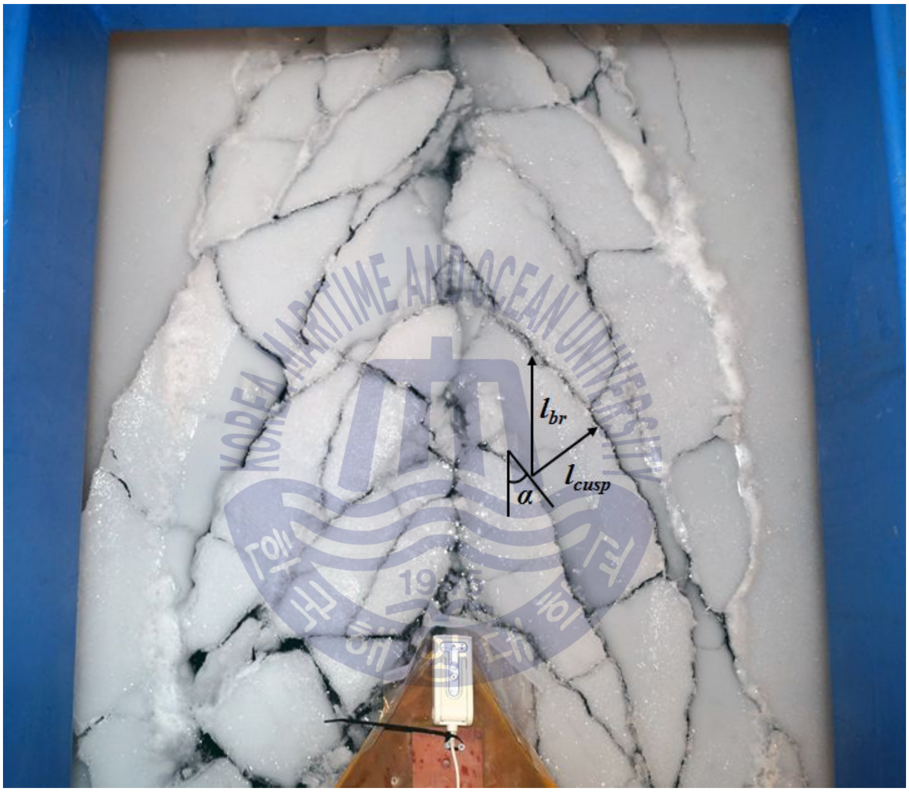

Fig. 16 Definition of ice cusp depth and breaking length (photograph by the author)

3.1.2 Definition of Ice and Hull Contact Conditions

To determine the ice resistance the crushing, breaking, and submersion components should be considered. Figure 17 shows crushing, breaking, and submersion phenomena in the model test. When an icebreaker model encounters an ice sheet, crushing occurs at the stem, and the contact area continues to increase until bending failure of the ice sheet occurs. After bending failure, the broken ice pieces are rotated and submerged along the ship bottom. This cycle is repeated during the icebreaking process.

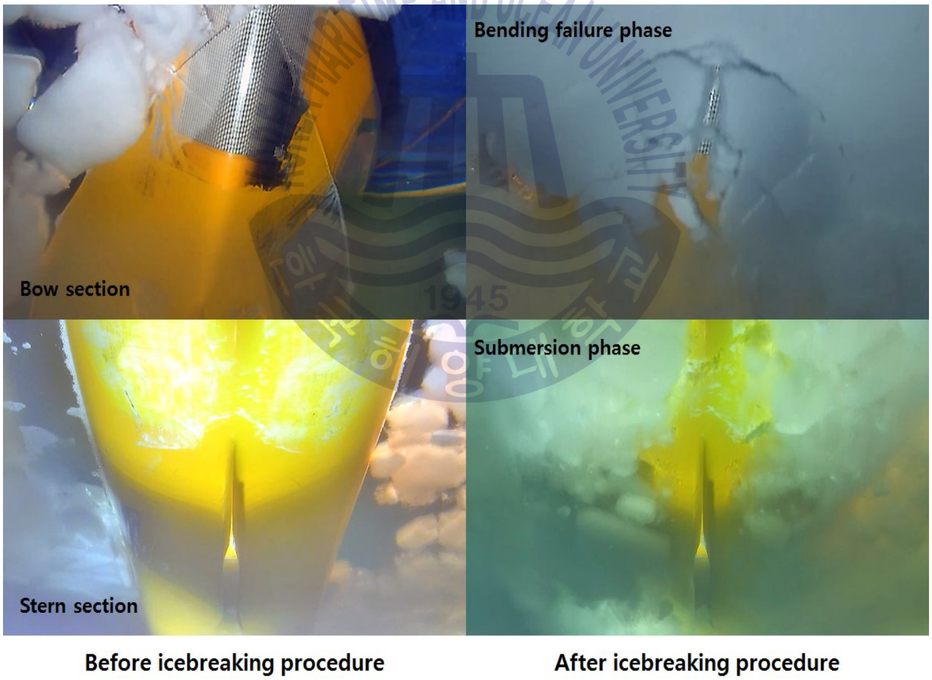

Fig. 17 Icebreaking phenomena in the model test (Jeong et al., 2014)

Noble et al. (1979) developed a mathematical model to predict ship performance in ice. To calculate the ice force, three aspects of ice-hull contact were considered—the angular floe edge, the round floe edge, and the triangular edge due to the indentation of a ship's bow. The three contact interfaces are shown in Fig. 18.

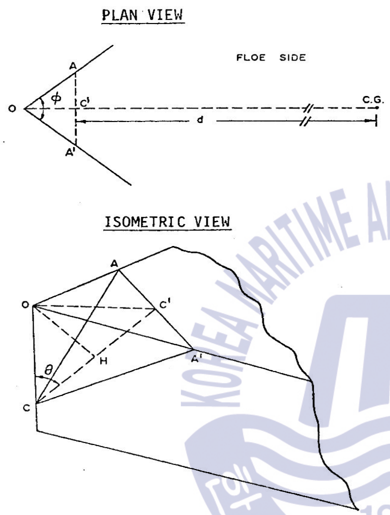

$$A = b_0 h_c / \cos\theta$$
$$b_0 = (\overline{AA'}/2) = d_c \tan\phi/2 \tag{11}$$

(a) Angular edge floe

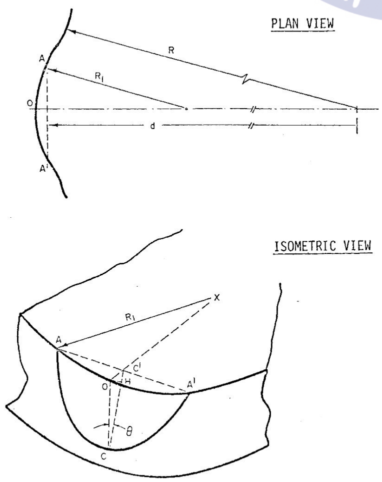

$$A = \frac{4b_0 h_c}{3\cos\theta}$$
$$b_0 = (\overline{AA'}/2) = \sqrt{R_1^2 - (R_1 - d_c)^2}$$
$$h_c = d_c / \tan\theta$$

d_c=horizontal distance crushed ($\overline{OC'}$) (12)

(b) Round edge floe

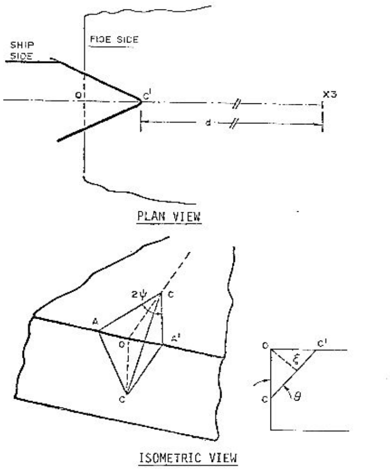

$$A = \frac{cBh_c}{\cos\theta} \tag{13}$$

(c) Triangular edge floe

Fig. 18 Various ice and ship contact aspects (Noble et al., 1979)

Sawamura et al. (2010) defined the contact points between a ship and the level ice edge (see Fig. 19). The contact area was calculated using a circle contact technique based on the results of Dimglina et al. (2000, cited in Sawamura et al., 2010). The accuracy of the contact detection depends on the circle radius, and thus the optimized circle radius was selected in the previous study (Sawamura et al., 2009). The crushing area can be calculated as

$$\begin{aligned} A_c &= \frac{1}{2\sin\theta_s}(\tan\theta_{wf} + \tan\theta_{wb})(vt_c\cos\theta_c)^2, \ \ 0 < t_c < \frac{h_i\tan\theta_s}{v\cos\theta_c} \\ A_c &= \frac{1}{2\cos\theta_s}(\tan\theta_{wf} + \tan\theta_{wb})(2vt_c h_i\cos\theta_c - h_i^2\tan\theta_s)^2, \ \ t_c > \frac{h_i\tan\theta_s}{v\cos\theta_c} \end{aligned} \tag{14}$$

where t_c is time of a ship penetrating in an ice, h_i is the ice thickness, θ_c is the contact angle of a ship, θ_s is a ship's hull angle at the contact plane, and θ_{wf} and θ_{wb} are the fore side and back side wedge angles of ice, respectively.

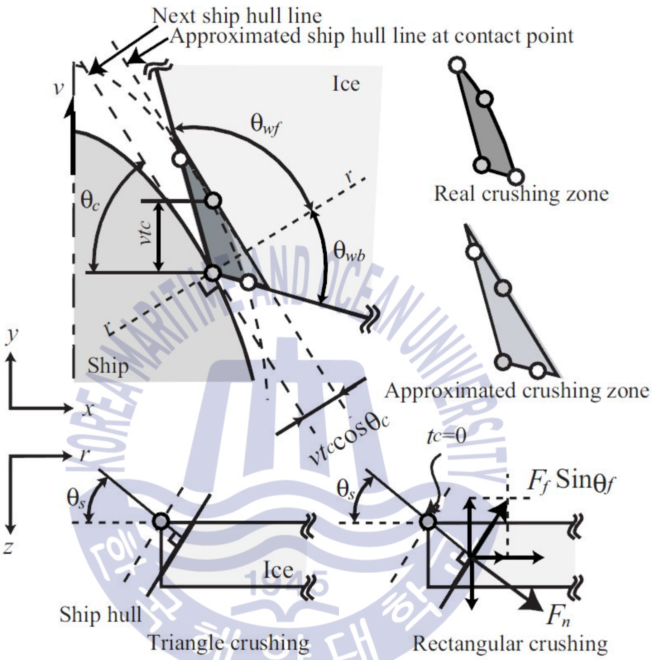

Fig. 19 Ice and ship contact condition (Sawamura et al., 2010)

Su et al. (2010) idealized the hull and ice interaction, including the full-size waterline of the ship and the ice edge. They calculated the contact area using the contact length and indentation depth. Two contact cases were considered in the calculation of contact area, as follows (see Fig. 20):

$$A_c = \frac{1}{2} L_h \frac{L_c}{\cos(\phi)}, \quad L_c \tan(\phi) \le h_i \tag{15}$$

$$A_c = \frac{1}{2}\left(L_h + L_h\frac{L_c - h_i/\tan(\phi)}{L_c}\right)\frac{h_i}{\sin(\phi)},\ L_c\tan(\phi) > h_i$$

where ϕ is a slope angle of varying values at different hull zones. L_h and L_c are depicted in Fig. 20.

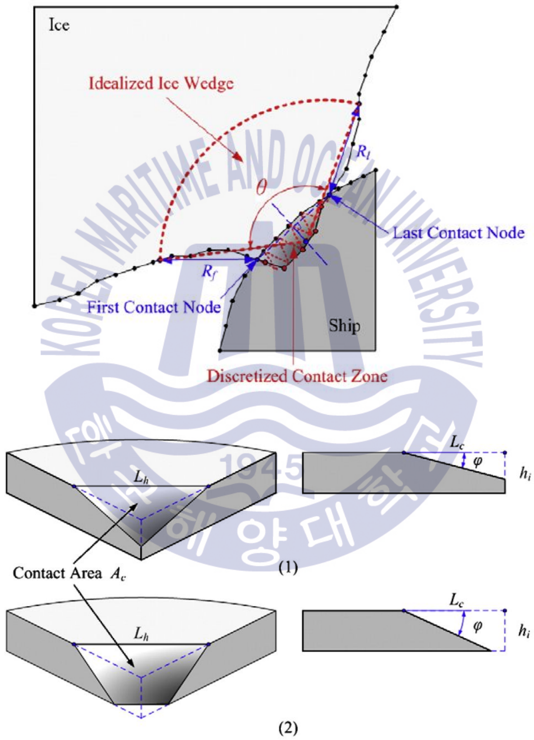

Fig. 20 Definition of ice and ship contact condition (Su et al., 2010)

Lubbad and Løset (2011) determined the contact area between ice and ship. The surface of the ship and the ice was surrounded by a two-dimensional polygon. The contact area was calculated at each time step. The contact area of the polygon can be calculated as (see Fig. 21)

$$\breve{A} = \frac{1}{2}\sum_{i=0}^{n-1}(x_i y_{i+1} - x_{i+1} y_i),\ x_n = x_0,\ y_n = y_0$$
$$A = \frac{\breve{A}}{\cos\breve{\alpha}} \tag{16}$$

where $\breve{A}$ is the contact area projected onto the horizontal plane, $\breve{\alpha}$ is the slope angle between the hull and the horizontal plane averaged over the contact area, and x and y are the coordinates of the vertices of the interaction polygon.

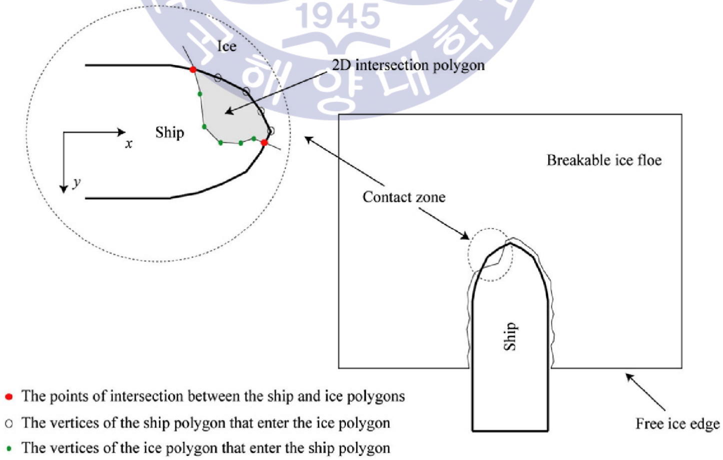

Fig. 21 The intersection polygon area between ice floe and ship (Lubbad and Løset, 2011)

In the present study, the failure mode of an ice floe is divided into two alternative phases, crushing-shearing and crushing-bending, and is related to the ice and hull contact area. During an icebreaking procedure, if the force derived from the contact area is less than what would cause bending failure of the ice, the failure mode of the ice floe consists of the crushing and the shearing phases, but when the force derived from the contact area is sufficiently large, bending failure occurs in the ice floe. After bending failure, broken ice pieces are submerged under the ship's bow and bottom, causing friction force against the ship (see Fig. 17).

The calculation of the ice and hull contact area is an important aspect of this study. Therefore, to determine the projected contact area after impact, the ice floe is assumed to be level ice and the occurrence of ice-hull contact can be regarded as a symmetrical collision. This assumption allows two ice-hull contact cases to be considered (see Fig. 22), one for triangular crushing and one for quadrilateral crushing at the stem (Eqs. 17 and 18).

Case I (triangular crushing, $0 < \dfrac{\zeta_{n_i}}{\cos\phi_i} \leq h$)

$$A_{n_i} = \frac{\zeta_{n_i}^2}{\sin\phi_i \cos\phi_i}\frac{1}{\cos\beta_i} \tag{17}$$

Case II (quadrilateral crushing, $\dfrac{\zeta_{n_i}}{\cos\phi_i} > h$)

$$A_{n_i} = \frac{\zeta_{n_i}^2 \cos\phi_i (2 - \cos^2\phi_i)}{\sin\phi_i}\frac{1}{\cos\beta_i} \tag{18}$$

where ζ_{n_i} is the normal crushing displacement, and ϕ_i and β_i are the buttock angle and frame angle. Subscript i denotes the $i-th$ contact point information.

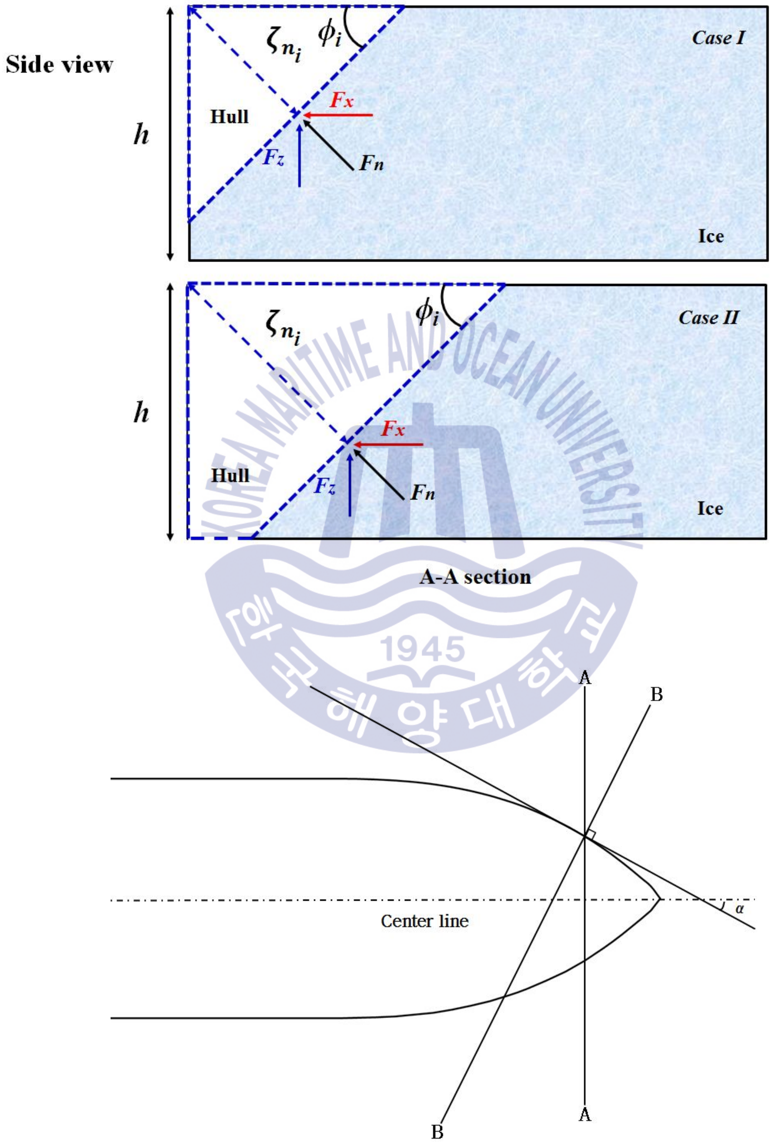

Fig. 22 Ice-hull contact case (Jeong et al., 2013)

3.2 Calculation of Ship Resistance in Ice

As mentioned in the Introduction, a numerical model to predict resistance in level ice is developed. This model can determine a ship's resistance in level ice condition based on Lindqvist's model. The submersion component is calculated using Lindqvist's formula, but the crushing and breaking components are newly determined in this study. The formulation of the breaking resistance of ice is discussed in this section.

3.2.1 Contact Force and Pressure-Area Effect

The geometry of a bow should be defined by the hull angles (see. Fig. 23). The equation of the plane tangential to the hull can be used to derive the unit vector perpendicular to the plane and can be used for semi-empirical formulae to predict ship resistance in ice. This method was introduced in previous studies (Kashteljan and Ryvlin, 1966; Enkvist, 1972; Edward and Nawwar, 1978). The hull geometry coefficients can be determined by the direction cosines of the unit vector and the hull angles (Noble and Bulat, 1981). It is a function of bow angles α and β, as follows:

$$
\begin{aligned}
n_1 &= \frac{\tan\alpha}{\sqrt{1+\tan^2\alpha+\tan^2\beta}} \\
n_2 &= \frac{1}{\sqrt{1+\tan^2\alpha+\tan^2\beta}} \\
n_3 &= \frac{\tan\beta}{\sqrt{1+\tan^2\alpha+\tan^2\beta}}
\end{aligned}
\tag{19}
$$

where n_1, n_2, and n_3 denote direction cosines in the x, y, and z directions, respectively (see Fig. 24).

During ice-hull interaction, normal contact force occurs. This force assumes that the strength of ice is constant throughout the ice-hull interaction. Normal contact force, F_n, can be calculated as

$$F_n = \sigma_c A_n \tag{20}$$

where σ_c is the uniaxial crushing strength of ice and A_n is the normal contact area.

This concept does not reflect the ice-hull interaction phenomena and would lead to erroneous results in the calculation of contact force. Therefore, pressure-area effects can be used. As discussed by Lewis et al. (1983) and Tan et al. (2013), normal contact force can be calculated using a pressure-area relationship and should be proportional to resistance through its direction cosine, n_1.

$$F_n = p_0 \left(\frac{A_n}{A_0} \right)^e A_n n_1 = p_{av} A_n n_1 \tag{21}$$

In $p_{av} = p_0 \left(\frac{A_n}{A_0} \right)^e = k A_n^e$ above, p_0 and A_0 are the reference pressure and area. k and e are parameters, and e has a negative value.

The values for p_0 and A_0 were determined from a full-scale ice trial of the Korean icebreaker, Araon in the Beaufort Sea. The calculated maximum ice pressure derived from the influence coefficient method was 2.12 MPa, and the area was 0.25 m^2 (Lee et al., 2013). To determine the normal contact force, the author assumes that the ship's motion has only a small role in the process of icebreaking; thus, potential energy derived from heave and pitch motions can be ignored. As discussed in Daley (1999), the maximum crushing displacement is calculated based on the relationship between indentation energy and kinetic energy. In particular, the kinetic energy is related to the effective mass and the normal velocity of the ship. The indentation energy is the integral of the normal contact force on the normal crushing displacement. Based on this, the normal crushing displacement can be determined at each contact point. In

$$IE_{ice} = KE_{ship} \rightarrow \int_N F_n d\zeta_N = \frac{1}{2} M_e V_n^2 \tag{22}$$

M_e and V_n denote the equivalent mass of the ship and normal velocity at the impact point, respectively. Herein, the equivalent mass is a function of the inertial properties of ship. This equivalent mass is linearly proportional to the mass of the ship (M_e). Other parameters were defined by Popov et al. (1969).

Equivalent mass $M_e = M/C_o$

Added mass in surge $M_x = 0$

Added mass in sway $M_y = 2T/B$ (23)

Added mass in heave $M_z = 2/3(BC_{wp}^2)/(TC_b(1+C_{wp})$

Added mass in roll $j_{xx} = 0.25$

Added mass in pitch $j_{yy} = B/T(3-2C_{wp})(3-C_{wp})$

Added mass in yaw $j_{zz} = 0.3 + 0.05L/B$

Mass radii of gyration in roll $R_{xx}^2 = C_{wp}B^2/(11.4C_m) + H^2/12$

Mass radii of gyration in pitch $R_{yy}^2 = 0.07C_{wp}L^2$

Mass radii of gyration in yaw $R_{zz}^2 = L^2/16$

Direction cosine $l = \sin(\alpha)\cos(\beta')$

Direction cosine $m = \cos(\alpha)\cos(\beta')$

Direction cosine $n = \sin(\beta')$

Moment arm in roll $\lambda l = ny - mz$

Moment arm in pitch $\mu l = lz - nx$

Moment arm in yaw $\eta l = mx - ly$

Mass reduction coefficient

in

$$
\begin{aligned}
C_o = {} & l^2/(1+M_x) + m^2/(1+M_y) + n^2/(1+M_z) + \\
& \lambda l^2/(R_{xx}^2(1+j_{xx})) + \mu l^2/(R_{yy}^2(1+j_{yy})) + \eta l^2/(R_{zz}^2(1+j_{zz}))
\end{aligned}
$$

T is the ship draft, B is the ship breadth, L is the ship length, C_{wp} is the water plane coefficient, C_b is the block coefficient, and C_m is the midship section coefficient. x, y and z denote the length from the centre of the ship to the impact point. z coincides with the waterline. β' is the normal frame angle.

The three force components for the x, y, and z directions can be determined as

$$F_x = F_n n_1 = p_{av} A_n n_1^2$$
$$F_y = F_n n_2 = p_{av} A_n n_1 n_2 \qquad (24)$$
$$F_z = F_n n_3 = p_{av} A_n n_1 n_3$$

The total force components can be calculated by summing each force component over the waterline, as follows:

$$F_X = \sum_{waterline} p_{av} A_{n_i} n_{1_i}^2$$
$$F_Y = \sum_{waterline} p_{av} A_{n_i} n_{1_i} n_{2_i} \qquad (25)$$
$$F_Z = \sum_{waterline} p_{av} A_{n_i} n_{1_i} n_{3_i}$$

During the ice-hull interaction, the influence of friction between hull surface and ice is a significant parameter; thus, friction should be considered. The friction force acts on the horizontal plane at the waterline level in the direction of the tangent to the waterline; therefore, only components in the $x-$ and the $y-$ direction can be considered. The friction force can be written as

$$F_\mu = \mu p_{av} A_n n_1 \qquad (26)$$

where μ is the frictional coefficient between the hull surface and the ice.

The components of this force in x and y direction can be expressed as

$$
\begin{aligned}
F_{\mu} &= \mu p_{av} A_n n_1 \sin\alpha \ \text{(in } x \text{ direction)} \\
F_{\mu} &= -\mu p_{av} A_n n_1 \cos\alpha \ \text{(in } y \text{ direction)}
\end{aligned}
\tag{27}
$$

Finally, the total force components considering the friction in each direction can be expressed as

$$
\begin{aligned}
F_X &= \sum_{waterline} p_{av} A_{n_i} n_{1_i} (n_{1_i} + \mu \sin\alpha_i) \\
F_Y &= \sum_{waterline} p_{av} A_{n_i} n_{1_i} (n_{2_i} - \mu \cos\alpha_i) \\
F_Z &= \sum_{waterline} p_{av} A_{n_i} n_{1_i} n_{3_i}
\end{aligned}
\tag{28}
$$

where α_i denotes the $i-th$ waterline entrance angle.

3.2.2 Failure Criterion of Ice

The vertical component, F_Z, and the horizontal component, F_X, are related to the failure criterion of the ice sheet and the ship resistance in ice. In order to define the failure mode of the ice floe in the present model, the failure criterion should be determined. The failure phenomena of an ice sheet consists of two main parts—the crushing/shearing and the bending/buckling of an ice wedge. These are related to the contact area between the hull and the ice. The contact area is a critical factor and changes as a function of penetration depth. In particular, the strength parameter used in the failure criteria is associated with the bending strength of ice sheet.

The failure that occurs after the crushing stage determines the contact force. This failure can take place by bending, buckling, or shearing. The bending mode is dominant when vertical force is applied. This approach can be used in predicting the bearing capacity of a floating plate subjected to a load of short duration. Kashteljan (1960) determined the failure load, P_f, for an infinite plate, and the relationship is expressed as

$$P_f = 2.08\left(\frac{\theta}{\pi}\right)\sigma_f h^2 \tag{29}$$

where θ is the opening angle of the ice wedge and σ_f is the flexural strength of ice.

Kerr (1975) also generalized formulae for the failure load, P_f, of a floating ice wedge plate of opening angle, θ, and the relationship is expressed as (See. Fig. 25)

$$P_f = C_f\left(\frac{\theta}{\pi}\right)^2 \sigma_f h^2 \tag{30}$$

where C_f is an empirical parameter

Su et al. (2010) studied the effect of the empirical parameter. He recognized that the empirical parameter should be related to the magnitude of icebreaking force. In his study, the empirical parameter selected for 3.1 based on the value of Lindqvist’s ice resistance component. Hu and Zhou (2015) also focused on the effect of the empirical parameter. They considered the empirical parameter as a function of vessel speed, ice thickness, and gravity acceleration. Herein, the speed of the vessel was regarded as 1.0 m/s. The empirical parameter may be affected by the strength number and the Froude number, F_N, because it should be related to the strength of ice. Therefore, the strength number may be more significant than the Froude number and is thus considered in this study. The strength number was discussed by Spencer and Jones (2001) and is defined as

$$S_N = \frac{V}{\sqrt{\dfrac{\sigma_f h}{\rho_i B}}} \tag{31}$$

where ρ_i denotes the density of ice.

In this study, the revised failure criteria of a ice wedge plate subjected to the load of ice-hull interaction is defined as

$$P_f = \frac{S_N}{F_N}\left(\frac{\theta}{\pi}\right)^2 \sigma_f h^2 \tag{32}$$

The opening angle, θ, can vary from the $\pi/3$ to $\pi/5$. The determination of the maximum load, $P_{\max}$, at which ice fails is determined using the criterion.

$$P_{\max} = P_f \tag{33}$$

The present model is based on assuming a plate on an elastic foundation is subject to a vertical load at one of its ends. The vertical load causing bending failure is calculated during ice-hull interaction, which yields a corresponding peak horizontal load. In the calculation, if the maximum concentrated load $P_{\max}$ is larger than the F_Z, the failure mode of the ice sheet is mainly composed of the crushing and shearing phases, but when the F_Z sufficiently exceeds $P_{\max}$, a bending failure occurs. Based on these assumptions, the crushing and breaking components, R_b, can be determined.

3.2.3 Resistance Components in Ice

In this study, the submersion component is calculated based on Lindqvist's model, whereas the crushing and breaking components are calculated based on the present model. In Lindqvist's model, the submersion component, R_s, is defined as

$$R_s = (\rho_w - \rho_{ice}) g h_{tot} B\left(T\frac{B+T}{B+2T} + k\right)$$

$$k = \mu\left(\begin{array}{l} 0.7L - \dfrac{T}{\tan\phi} - \dfrac{B}{4\tan\alpha} + \\ T\cos\phi\cos\psi\sqrt{\dfrac{1}{\sin^2\phi} + \dfrac{1}{\tan^2\alpha}} \end{array}\right), \quad \psi = \arctan\frac{\tan\phi}{\sin\alpha} \qquad (34)$$

where h_{tot} is the total ice and snow thickness.

Lindqvist's model assumed that the ice resistance, R_{ice}, increased linearly with the ship speed. This assumption is applied in the present model; therefore, the ice resistance at each time step is expressed as

$$R_{ice}(t) = R_b(t) + R_s\left(1 + \frac{9.4v}{\sqrt{gL}}\right) \qquad (35)$$

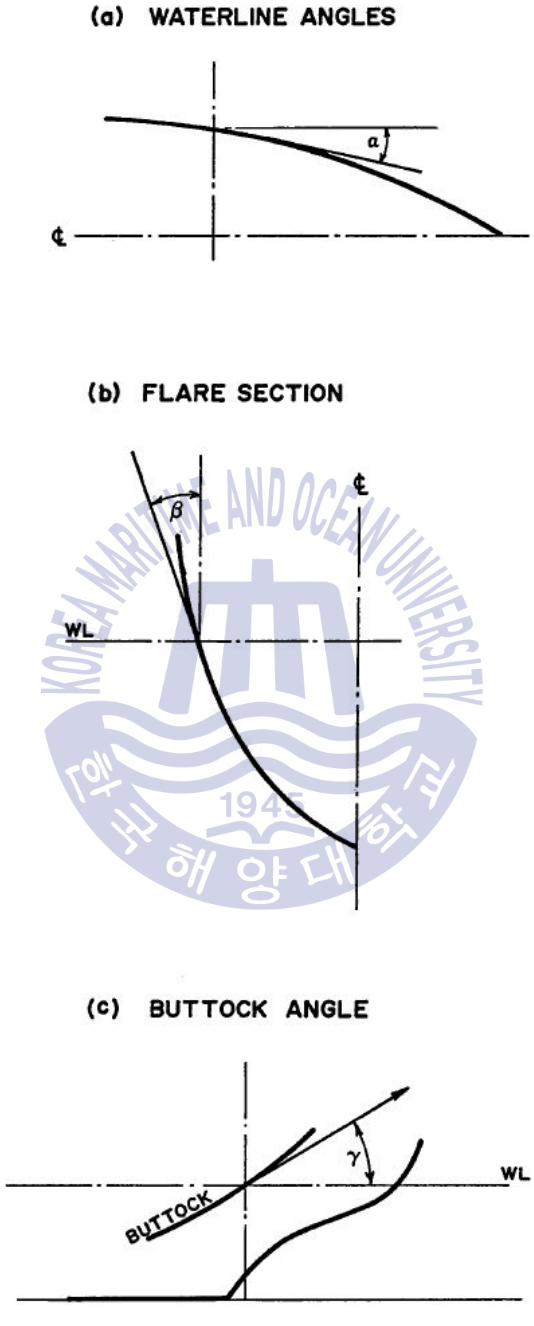

Fig. 23 Definition of hull angles (Lewis et al., 1983)

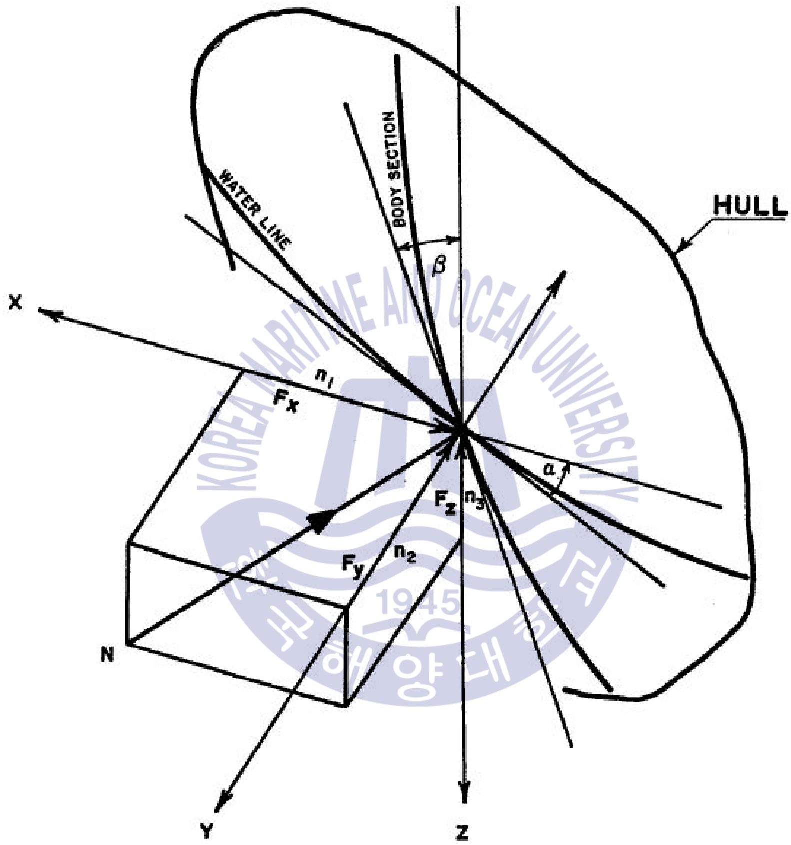

Fig. 24 Definition of direction cosines (Lewis et al., 1983)

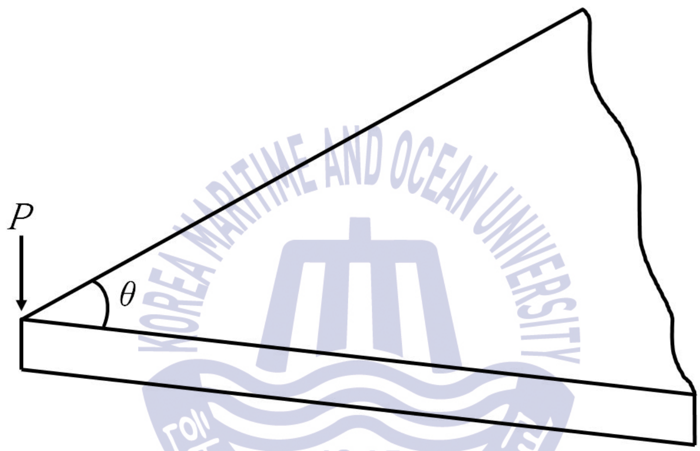

Fig. 25 Floating wedge subjected to a load at its apex (redrawn from Kerr, 1976)

3.3 Motion Analysis by Numerical Integration

To analyze the ship motions, a general equation of motion is used. Let (x, y, z) be a right-handed coordinate system fixed with respect to the mean position of the ship with z vertically upward through the center of gravity of the ship, x in the direction of the forward motion, and the origin in the plane of the un-disturbed free surface. Under the assumption that the responses are linear and harmonic, six linear coupled differential equations of motion can be written using subscript notation in the following abbreviated form

$$[M+A]\{\ddot{x}(t)\}+[C]\{\dot{x}(t)\}+[K]\{x(t)\}=\{F(t)\} \tag{36}$$

where $[M]$, $[A]$, $[C]$, and $[K]$ are the mass, hydrodynamic added mass, damping and hydrostatic resorting matrices for the system, and $\{\ddot{x}(t)\}$, $\{\dot{x}(t)\}$, and $\{x(t)\}$ refer to the acceleration, velocity, and displacement vectors, respectively. $\{F(t)\}$ is the excitation force vector.

The simulation is performed in 3-DOF (namely surge, sway and yaw), and the ship has lateral symmetry. The mass and added mass matrices are

$$M=\begin{bmatrix} M_{11} & 0 & 0 \\ 0 & M_{22} & 0 \\ 0 & 0 & I_{66} \end{bmatrix} \text{ and } A=\begin{bmatrix} A_{11} & 0 & 0 \\ 0 & A_{22} & A_{26} \\ 0 & A_{62} & A_{66} \end{bmatrix} \tag{37}$$

where M_{11} and M_{22} are the mass of the ship, and I_{66} is the moment of inertia in z direction. M_{11} and M_{22} are 7579 tons, I_{66}=4.27507×10^6 tons/m^2. A_{11}, A_{22} and A_{66} are 377.2 tons, 5433.6 tons, and 2.13549×10^6 tons/m^2.

The excitation force caused by ice-hull interaction is

$$F = \begin{bmatrix} F_X^i \\ F_Y^i \\ M_N^i \end{bmatrix} \tag{38}$$

where F_X^i, F_Y^i, M_N^i are forces and moment. Propeller, rudder, and hydro-dynamic forces were excluded from the calculation.

In this study, a numerical integration method called the Newmark-β method is used to analyze the motion of the ship and the ice resistance characteristics. The Newmark-β method is based on the assumption that the acceleration varied linearly between two instants of time. In the Newmark-β method, velocity and displacements are given by

$$\begin{aligned} \{\dot{x}_{t+\triangle t}\} &= \{\dot{x}_t\} + \triangle t\left[(1-c_1)\{\ddot{x}_t\} + c_1\{\ddot{x}_{t+\triangle t}\}\right] \\ \{x_{t+\triangle t}\} &= \{x_t\} + \triangle t\{\dot{x}_t\} + \frac{\triangle t^2}{2}\left[(1-2c_2)\{\ddot{x}_t\} + 2c_2\{\ddot{x}_{t+\triangle t}\}\right] \end{aligned} \tag{39}$$

The coefficients c_1 and c_2 indicate how much the acceleration enters into the velocity and displacement equations at the end of the interval $\triangle t$. When $c_1 = 1/2$ and $c_2 = 1/6$, Equation (39) corresponds to the linear acceleration method and can be rewritten in the following form

$$\begin{aligned}
\{\ddot{x}_{t+\triangle t}\} &= \frac{6}{\triangle t^2}\{x_{t+\triangle t} - x_t\} - \frac{6}{\triangle t}\{\dot{x}_t\} - 2\{\ddot{x}_t\} \\
\{\dot{x}_{t+\triangle t}\} &= \frac{3}{\triangle t}\{x_{t+\triangle t} - x_t\} - 2\{\dot{x}_t\} - \frac{\triangle t}{2}\{\ddot{x}_t\}
\end{aligned} \tag{40}$$

Equation (36) can be employed to obtain a solution for displacements, velocities, and accelerations at time $t+\triangle t$. Thus, by substituting the expressions for displacements and velocities from Equation (40) into the governing differential equation of motion (Equation (36)).

$$\{x_{t+\triangle t}\} = \lfloor \overline{M} \rfloor^{-1}\{\overline{F}_{t+\triangle t}\} \tag{41}$$

where the effective mass matrix $\lfloor \overline{M} \rfloor$ and the effective force vector $\{\overline{F}_{t+\triangle t}\}$ are given by

$$\begin{aligned}
\lfloor \overline{M} \rfloor &= \left(\frac{6}{\triangle t^2}[M+A]\right) + \frac{3}{\triangle t}[C] + [K] \\
\{\overline{F}_{t+\triangle t}\} &= \{F_{t+\triangle t}\} + \begin{bmatrix} [M+A]\left(\frac{6}{\triangle t^2}\{x_t\} + \frac{6}{\triangle t}\{\dot{x}_t\} + 2\{\ddot{x}_t\}\right) + \\ [C]\left(\frac{3}{\triangle t}\{x_t\} + 2\{\dot{x}_t\} + \frac{\triangle t}{2}\{\ddot{x}_t\}\right) \end{bmatrix}
\end{aligned} \tag{42}$$

From Equation (41), $\{x_{t+\triangle t}\}$ should be calculated, and then acceleration and velocity at time $t+\triangle t$ should be calculated from Equation (40). The damping and stiffness coefficients are assumed to be zero in the calculation.

The iteration is continued until the change in the excitation from one interaction to the next is small enough. The conversion criterion can be expressed by

$$\frac{\sqrt{(\overline{F}_{t+\triangle t}-\overline{F}_t)^2)}}{\sqrt{(\overline{F}_t)^2}} \leq \varepsilon \tag{43}$$

where ε is of the order 10^{-3}.

The present model is implemented in a FORTRAN program. The flowchart of the calculation procedure is illustrated in Fig. 26.

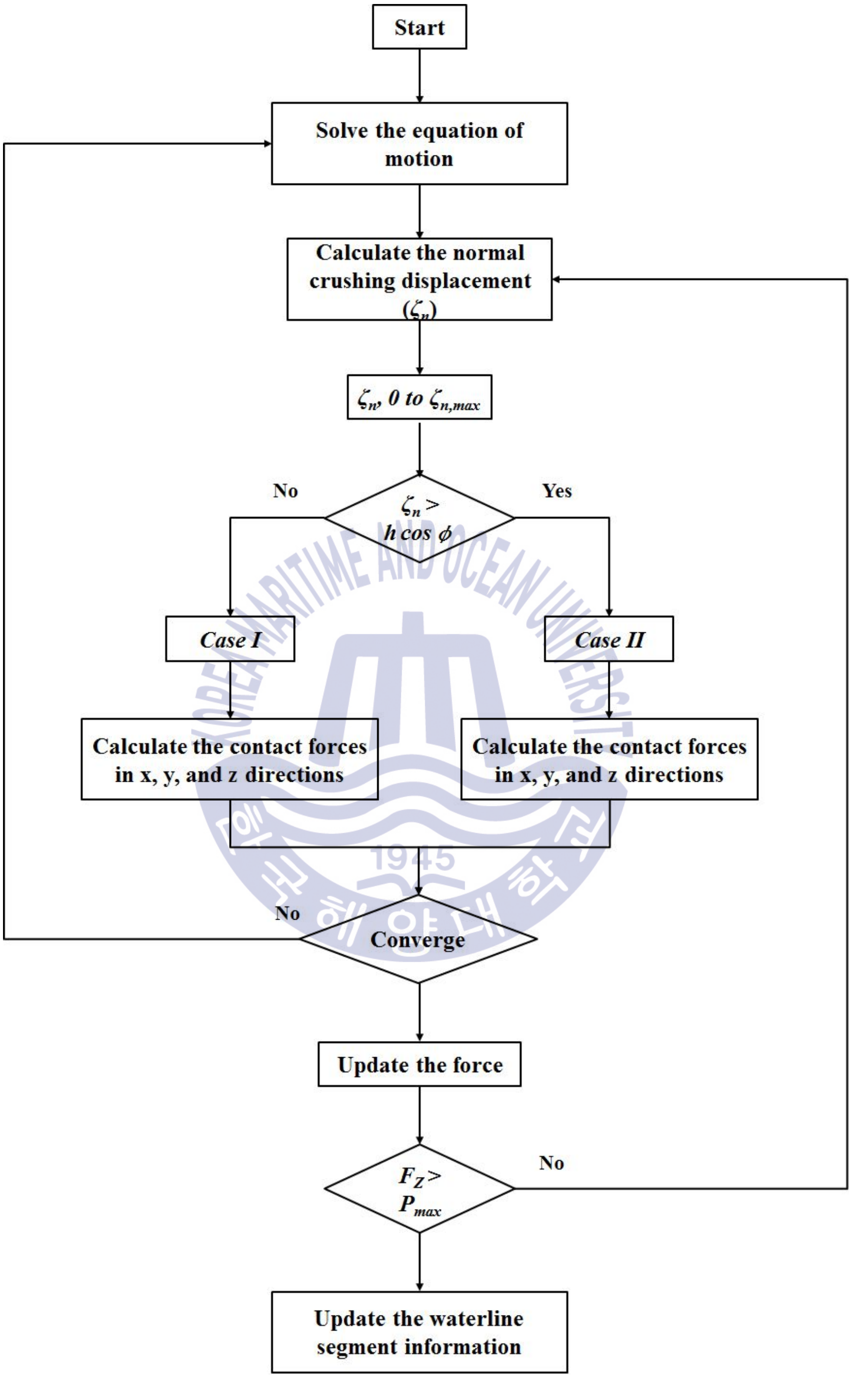

Fig. 26 Flowchart of the calculation procedure for the present model

Chapter 4 Comparison of Ice Resistance between Predictions

4.1. Experimental Test in Ice Tank

Generally, the model tests conducted in an ice tank can be used to quantify ice resistance and propulsion performance and to evaluate the efficiency of the hull form and the propulsion system. In this study, the objectives of the tests are to understand icebreaking phenomena observed around ship hulls, to obtain the parameters of the pressure-area effect, and to confirm the results of the present model.

4.1.1 Overview of Test Facility

The KRISO ice tank is a square-type ice tank. The size and shape of the tank are designed to enhance the model test capabilities of arctic offshore structures and the maneuvering performance of ice-going vessels. In particular, the KRISO ice tank permits a model ship to complete a full turning circle test. In a typical ship resistance and/or propulsion test, the 32 m of available ice width allows more than five or six parallel test channels within one ice sheet. The dimensions of the ice tank are as follows: 42 m (length) × 32 m (width) × 2.5 m (depth) (see Fig. 27).

- Trimming tank size: 10 m (length) × 32 m (width)
- Usable ice sheet size: 32 m (length) × 32 m (width)
- Model ice type: ethylene glycol (EG)/aliphatic detergent (AD)/controlled density (CD)
- Crystal structure of model ice: columnar type
- Micro-bubble generation system to control the density of model ice

The KRISO ice tank is using EG/AD-CD model ice. Herein, EG, AD, and CD denote ethylene glycol, aliphatic detergent, and controlled density, respectively. The model ice is a dilute aqueous solution of EG and AD in an approximate ratio of 0.39/0.036 %. By fine-tuning model ice preparation techniques, model ice up to 100 mm thick can be produced, with an allowance of about ±5.0 % accuracy. The model ice production procedures are similar to those used for the NRC-OCRE ice tank.

The KRISO ice tank is equipped with a main X-Y towing carriage system consisting of an X-carriage and a Y-carriage. The X-carriage can tow models through the ice sheet or the ice sheet against the model, which is fixed or moored to the bottom of the tank. The Y-carriage is suspended beneath the main X-towing carriage and can move throughout its length. A service carriage is installed for model ice production and treatment of the ice in the model test. After the model test in ice, six movable blades installed on the service carriage push the broken ice sheets into an ice-melting pit. The main particulars of the towing carriage system are as follows:

- X-carriage speed: max: 3.0 m/s and min: 0.005 m/s
- Y-carriage speed: max: 1.5 m/s
- Towing force capability: X-direction, 50 kN; Y-direction, 3 kN
- Service carriage speed: 1.5 m/s

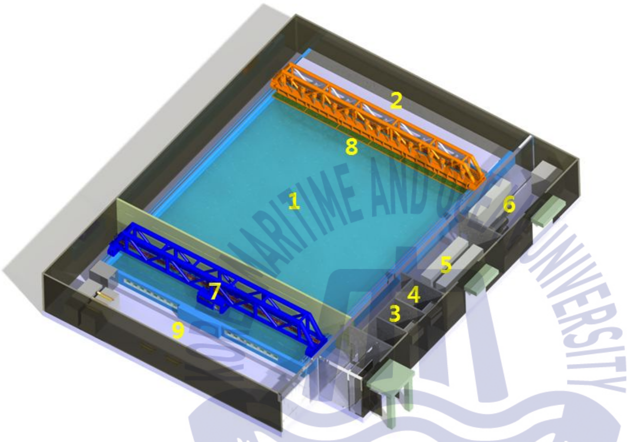

Fig. 27 Layout of the KRISO ice tank

The KRISO ice tank is equipped with an air cooling system and uses natural convection to generate the model ice sheet. This is a very effective method to produce an ice sheet with uniform thickness and strength for model tests.

- Air temperature control range: from −18 ℃ to +15 ℃
- Minimum temperature changing rate: 5 ℃/h
- Ice growth rate: 2.3 mm/h at −18±0.5 ℃
- Maximum ice thickness: 100 mm

4.1.2 Preparation of Model Ice and Material Properties Measurement

The preparation of the model ice sheet begins with a wet-seeding procedure. The model ice is grown at a temperature of -18±0.5 ℃. The growth rate during this period is expected to be approximately 2.3 mm/h. After the level ice thickness reaches the target value, the air temperature is increased to +2 ℃ to control the strength of the ice. The target ice strength is achieved via tempering processing.

The properties of the model ice are routinely measured for each ice sheet, and a database of model ice properties is maintained for quality control and prediction. Micro-bubbles are uniformly discharged from the bottom of the ice tank over the entire ice-grown area during the entire freezing and tempering process to adjust the model ice density to simulate that of the Arctic sea ice range. Figure 28 shows the model ice preparation process in the KRISO ice tank.

The thickness of the model ice is usually measured immediately after a test along the broken channel every 2.5 m using digital Vernier calipers to obtain the longitudinal profile of the level ice channel.

The measurement of the flexural strength of the model ice is carried out for each test channel before the test. The flexural strength is determined using an in-situ cantilever beam test with the proportions of thickness:width:length of 1:2:5. The tip of the beam is loaded using a digital push-pull gauge until the beam fails with downward loading and upward loading (see Fig. 29). This procedure is carried out for each test channel during the tempering phase and after the test. Several beams are prepared in one spot. The flexural strength is determined using linear elastic beam theory as:

$$\sigma_f = \frac{6PL'}{wh^2} \tag{44}$$

where P, L', and w denote the failure load, length of beam, width of beam, respectively.

The elastic modulus of model ice is determined by the plate deflection method of the ice sheet. The theory of a rectangular plate on the elastic foundation is used to get the relation equation between the effective elastic modulus and the ice sheet deflection by applying the characteristic length concept (see Fig. 30). The elastic modulus is determined from the equation. In

$$\begin{aligned} E &= \frac{12(1-\nu^2)k'' l_c^4}{h^3} \\ l_c &= \left(\frac{\triangle P}{\triangle \omega}\right)\frac{1}{8k''}Z \\ Z &= 1 + \frac{\alpha^2}{2\pi}\left(\ln\frac{\gamma\alpha}{2} - \frac{5}{4}\right),\ \alpha = \frac{\gamma}{l_c} \end{aligned} \tag{45}$$

k'' is the specific weight of water (=10kN/m^3), $\triangle P$ is the deviation of load, $\triangle\omega$ is deflection and γ is the Euler constant (=0.5772). when $\alpha < 0.2$, $Z = 1$.

The compressive strength of model ice can be determined using the uniaxial compressive test. The specimen dimension is the proportion of thickness:width: length of 1:1:5. Figure 31 shows the uniaxial compressive test process of model ice. In

$$\sigma_c = \frac{P}{A} \tag{46}$$

A is the loaded area.

The density of model ice is determined using the weight method (see Fig. 32). The ice sample is floated in a beaker filled with solution. When the model ice is submerged, the weight of the excreted solution is measured. The density is determined using the equation

$$\rho_i = \frac{W_i \times \rho_s}{W_{\triangle w}} \tag{47}$$

where W_i is the model ice weight, $W_{\triangle w}$ is the weight of excreted solution, and ρ_s is the density of the solution. Herein $\rho_s = 1.0025\, g/cm^3$.

The frictional coefficient between the surface of the model hull and the ice is determined using the friction test. A wooden plate that had been painted at the same time as the model was used for the friction test. The ice sample is held in place by a load cell, and the normal load is provided by dead weight. The model surface is moved underneath at a uniform speed, and the friction force is measured in both directions of the model surface movement (see Fig. 33). All friction tests are carried out in the preparation section of the KRISO ice tank, where temperatures range from -1 ℃ to 0 ℃ during testing. The frictional coefficient, μ, is determined as the slope of a graph of friction force, F_μ, against normal load, N, and the weight of ice, W.

$$\mu = \frac{F_\mu}{N+W} \tag{48}$$

(a) Cooling phase

(b) Seeding phase

(c) Freezing phase

(d) Tempering phase

Fig. 28 Model ice preparation process in the KRISO ice tank

Fig. 29 Flexural strength measurement using an in-situ cantilever beam test

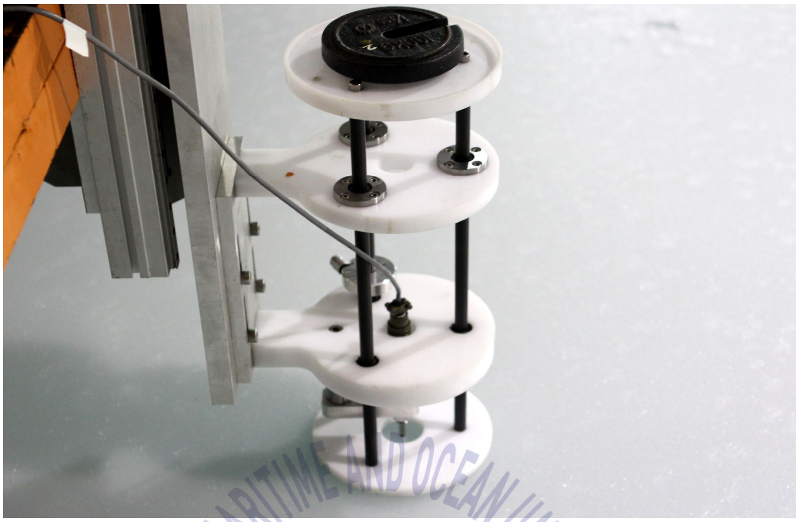

Fig. 30 Photograph of elastic modulus measurement

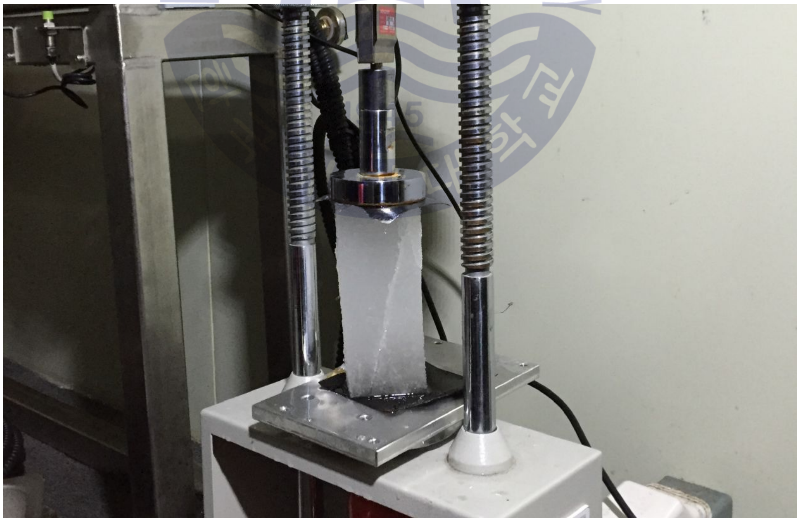

Fig. 31 Photograph of compressive strength measurement

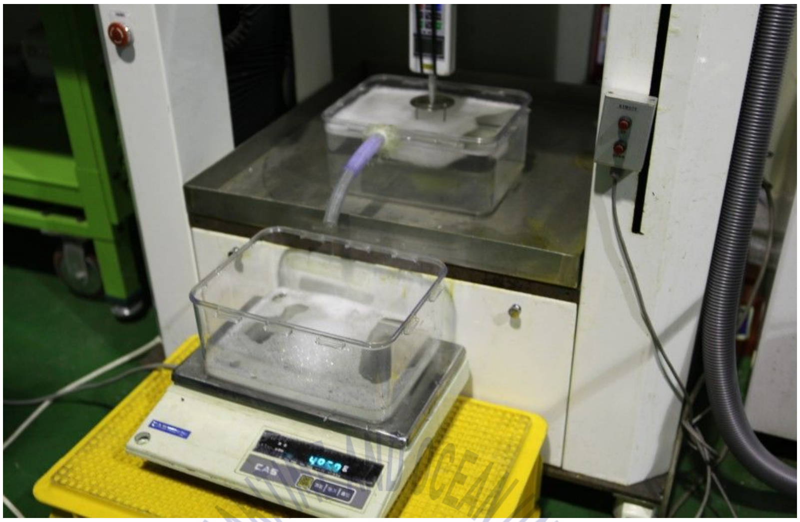

Fig. 32 Photograph of ice density measurement

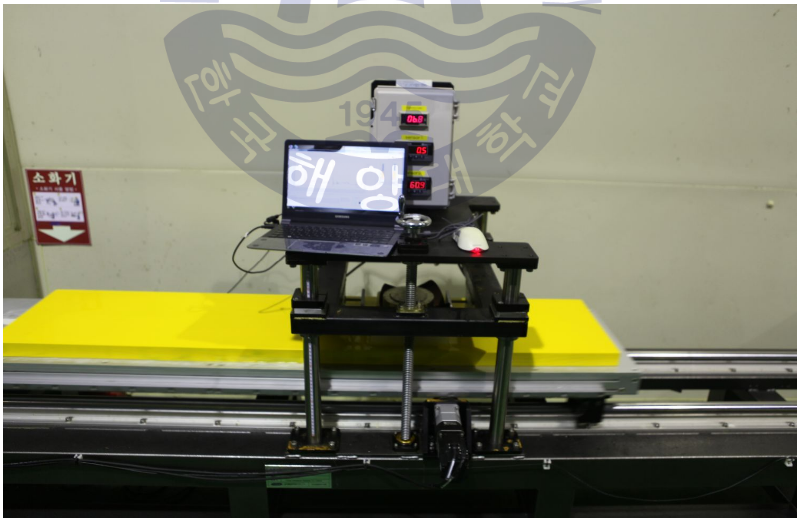

Fig. 33 Photograph of frictional coefficient measurement

4.1.3 Description of Model Ships and Test Conditions

Model tests were conducted with two different model ships, a Korean icebreaker and an Arctic Platform Supply Vessel (PSV). Towed propulsion tests were carried out for a design draft in level ice conditions. In the tests, the mechanical properties of model ice were correctly scaled in order to simulate those of sea ice. The model ice was prepared based on the standard procedure of the KRISO ice tank (KRISO, 2015). In the tests, the surface of the model hull was painted with a special painting technique to achieve the required friction coefficient between the surface of the model hull and the ice. To evaluate the performance of the ship models, the series of model tests listed below were carried out:.

a)	Hull Form 1	:	Icebreaker
	Ice conditions	:	Level ice, Pre-sawn ice
	Direction	:	Ahead
	Load Condition	:	Design
b)	Hull Form 2	:	Arctic PSV
	Ice conditions	:	Level ice, Pre-sawn ice
	Direction	:	Ahead
	Load Condition	:	Design

As mentioned above, hull form 1 is the model of the Korean icebreaker, Araon. The icebreaker model is designed to navigate the Arctic and other ice-covered areas where she is going to encounter first-year ice. This model was manufactured to the scale of λ=18.667 and has two azimuth units. The total propulsion power is 10 MW, and the icebreaking capacity is approximately 3.0 knots in 1.0 m level ice in continuous icebreaking mode, with a flexural strength of no less than 630 kPa (AARI, 2010).

Hull form 2 is the concept design model of the Arctic PSV. It is designed to supply an oil and gas platform operating in ice-covered waters. This model was manufactured to the scale of λ=19.587 and also has two azimuth units. The total propulsion power is 13 MW, and the icebreaking capacity is about 3.0 knots in 1.0 m level ice in continuous icebreaking mode. The main particulars of the vessels are summarized in Table 1. Figure 34 shows the model ships, and Table 2 shows the model test conditions.

Table 1 Main particulars of the test model ship

Hull Form No.	1		2	
	Ship	Model	Ship	Model
Waterline length (m)	95.0	5.09	96.0	4.9
Breadth (m)	19.0	1.02	24.0	1.2
Draught (m)	6.8	0.36	7.5	0.38
Stem angle (deg)	35.0	35.0	30.0	30.0

Fig. 34 Model ships used in the tests (top four photos: hull form 1, bottom four photos: hull form 2)

Table 2 Model ice conditions

Test No.	Parameters	Target Value	Measured Value	Remarks
1	E/σ_f	> 2000	> 2200	Hull form 1, level, pre-sawn
	h(mm)	30.0	28.7	
	σ_f(kPa)	30.0	27.1	
	μ	0.05	0.05	
	ρ_i(kg/m^3)	870	868	
2	E/σ_f	> 2000	> 2450	Hull form 1, level
	h(mm)	30.0	29.1	
	σ_f(kPa)	15.0	16.7	
	μ	0.05	0.05	
	ρ_i(kg/m^3)	870	872	
3	E/σ_f	> 2000	> 2100	Hull form 1, level
	h(mm)	50.0	53.2	
	σ_f(kPa)	25.0	25.0	
	μ	0.05	0.05	
	ρ_i(kg/m^3)	870	852	
4	E/σ_f	> 2000	> 2250	Hull form 1, level
	h(mm)	50.0	53.6	
	σ_f(kPa)	15.0	17.8	
	μ	0.05	0.05	
	ρ_i(kg/m^3)	870	870	
5	E/σ_f	> 2000	> 2700	Hull form 1, level, pre-sawn
	h(mm)	40.0	40.3	
	σ_f(kPa)	20.0	18.4	
	μ	0.05	0.05	
	ρ_i(kg/m^3)	870	870	
6	E/σ_f	> 2000	> 2700	Hull form 2, level, pre-sawn
	h(mm)	51.1	48.6	
	σ_f(kPa)	29.1	34.4	
	μ	0.05	0.05	
	ρ_i(kg/m^3)	870	890	

4.1.4 Analysis Procedures of Model Tests

The towed propulsion tests were conducted in the ice model tests. In a towed propulsion test, the ship model is towed by the main carriage running at a constant speed, and the motor in the ship model derives the propeller through dynamometer. During the tests, the following quantities were measured:

- Propeller revolution rate: The propeller revolution rate is measured by the encoder of the motor.
- Speed of the ship model: The ship model is towed by the main carriage in the model tests. The speed of the ship model is assumed to be equal to the main X-carriage speed.
- Towed force: The ship model is towed by a double-hinge type pulling bar and the towed force is measured by a load cell.
- Propeller thrust and torque: The propeller thrust and torque are measured by a dynamometer.

The towed force, propeller thrust, propeller torque, and model ship speed were recorded when the model ship achieved a steady speed in ice. The ship model is towed by a double-hinge type pulling bar, which is located on the bow of the ship model, and the towed force is measured by a load cell, which is located on the edge of the pulling bar. Pulling bar constrains the only surge motion of the model (see Fig. 35). The motor controller is set to deliver a constant propeller revolution rate and is gradually changed to reach the self-propulsion point in the test. In the towed propulsion test, the following variables were determined:

- Total resistance in ice
- Developed thrust at self-propulsion point
- Delivered power at self-propulsion point
- Propulsion efficiency in ice

In the model test, the rate of revolution can be changed three or four steps in each test channel to determine the self-propulsion point. The total resistance in ice can be obtained when the propeller thrust vanishes based on the linear regression in the relationship between the towed force and developed propulsion thrust. The self-propulsion point can be determined when the towed force vanishes. The delivered power (P_D) can then be obtained for the developed thrust at the self-propulsion point based on the relationship between the delivered power. The propulsion efficiency in ice can be obtained based on the total resistance in ice and the delivered power. The propulsion efficiency in ice, η_D, is defined by:

$$\eta_D = R_{tot} \times V / P_D \tag{49}$$

Fig. 35 Towed propulsion test in the KRISO ice tank (top: bow towing, bottom: stern towing)

4.1.4.1 Correction of Deviations in Ice Thickness and Strength

The correction formula for deviations between the target condition and the actual condition can be calculated as

$$R_{i,\,corr} = \left(aR_{i,\,meas} + b\frac{\sigma_{f,target}}{\sigma_{f,meas}}R_{i,meas}\right)\left(\frac{H_{i,\,target}}{H_{i,\,meas}}\right)^{x} \tag{50}$$

where $R_{i,\,meas}$ and $R_{i,\,corr}$ denote measured and corrected ice resistance, and $H_{i,\,meas}$ and $H_{i,\,target}$ denote measured and target ice thickness, respectively. The exponent, x, in the formula can be obtained from the model test results. The parameters a and b are the weight coefficients and can also be determined from model test results. $\sigma_{f,\,target}$ and $\sigma_{f,\,meas}$ denote the target and measured flexural strength of ice, respectively (ITTC, 2014).

The propulsion thrust (T), towed force (TF), and delivered power (P_D) have to be adjusted in the same manner. In

$$T_{corr} = \left(aT_{meas} + b\frac{\sigma_{f,target}}{\sigma_{f,meas}}T_{meas}\right)\left(\frac{H_{i,\,target}}{H_{i,\,meas}}\right)^{x}$$

$$TF_{corr} = \left(aTF_{meas} + b\frac{\sigma_{f,target}}{\sigma_{f,meas}}TF_{meas}\right)\left(\frac{H_{i,\,target}}{H_{i,\,meas}}\right)^{x} \tag{51}$$

$$P_{D,\,corr} = \left(aP_{D,\,meas} + b\frac{\sigma_{f,target}}{\sigma_{f,meas}}P_{D,meas}\right)\left(\frac{H_{i,\,target}}{H_{i,\,meas}}\right)^{1.5x}$$

T_{meas}, TF_{meas}, and $P_{D,\,meas}$ denote measured values and T_{corr}, TF_{corr}, and $P_{D,\,corr}$ denote corrected values.

4.1.4.2 Correction of Scale Effect

In the full-scale prediction, ice resistance is found by multiplying the obtained ice resistance by λ^3. The delivered power is found by multiplying the obtained delivered power by $0.96 \times \lambda^{3.5}$. Herein, a 4% allowance is applied to the model scale values in the full-scale prediction.

$$\begin{aligned} R_{i,\,full} &= \lambda^3 \times R_{i,\,\mathrm{model}} \\ T_{full} &= \lambda^3 \times T_{\mathrm{model}} \\ TF_{full} &= \lambda^3 \times TF_{\mathrm{model}} \\ P_{D,\,full} &= 0.96 \times \lambda^{3.5} \times P_{D,\,\mathrm{model}} \end{aligned} \tag{52}$$

These correction methods are similar to those used for the Hamburgische Schiffbau-Versuchscanstalt GmbH (HSVA) ice tank. The compensated values derived from the KRISO method and the HSVA method in correction are presented in Appendix B.

4.2. Discussions

In this section, the characteristic of icebreaking pattern is analyzed and the towed propulsion test results are summarized. Calculated results derived from the present model and model test results in an ice tank are compared, and the accuracy of the present model is discussed. The pressure-area effect is an important aspect of the prediction of ship resistance in ice. Figure 36 shows the pressure-area curve for parameters k and e with both the full-scale ice trial data of seven ice-going vessels (Jeong, 2008) and the data of the Korean icebreaker, Araon. In Fig. 36, the full-scale data of the Korean icebreaker is located in the middle region of the datasets for other ice-going vessels. The characteristic of ice resistance is investigated for the variation of those parameters in the pressure-area effect in sections 4.2.2 and 4.2.4.

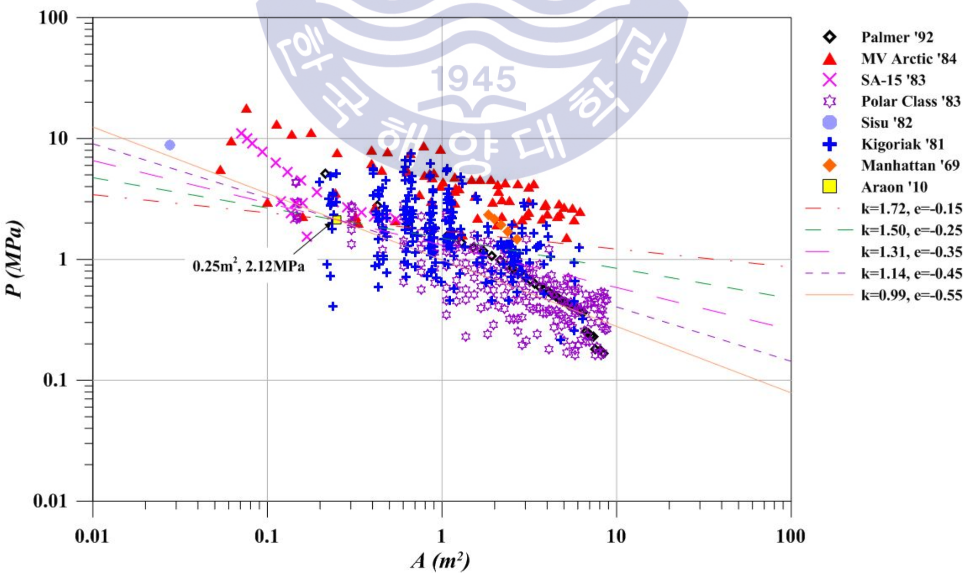

Fig. 36 Pressure and area relationship for parameters k and e with full-scale ice trial data of seven ice-going vessels and data of the Korean icebreaker

4.2.1 Analysis of Icebreaking Patterns

The icebreaking pattern can be associated with the ice thickness and ship speed, and it can significantly affect ship resistance in ice. To investigate the characteristics of icebreaking patterns, three different icebreaking model ships, the Korean icebreaker model, the Arctic PSV model, and the Arctic LNGC model, were used. In this study, the main particulars of the Arctic LNGC model and model test results were excluded. This information was confidential within the shipyard.

As mentioned above, ice cusp formation is related to the characteristic length of the ice; thus, these relations are depicted in Figs. 37 to 39 and are summarized in Table 3. In Fig. 37, the relation between the depth of the ice cusps and the characteristic length of ice can be assumed to be a linear relation, while the depth of the ice cusps and the ship speed are inversely proportional in Fig. 38. These relations should be attributable to the icebreaking phenomena. When the ship speed is low, the ice and hull contact area slowly increases, so the loading area will also slowly increase, but at higher speeds, the contact area will increase in a shorter time. In such case, the depth of the ice cusps will decrease. As a result, the depth of the ice cusps has a decreasing tendency in higher speed regions. The relation between the depth of ice cusps and the ratio of the characteristic length of ice and the ship speed is depicted in Fig. 39. Herein, the obtained parameters $\widehat{C}_1$ and $\widehat{C}_2$ are 0.211 and 0.425.

Table 3 Summary of icebreaking pattern

Test No.	V (m/s)	l_c (m)	l_{cusp} (m)	l_c/V
1	0.238	0.064	0.126	0.268
	0.357	0.063	0.112	0.177
	0.476	0.060	0.095	0.126
2	0.238	0.053	0.109	0.225
	0.357	0.060	0.085	0.167
	0.476	0.054	0.074	0.114
3	0.238	0.099	0.127	0.416
	0.357	0.097	0.121	0.271
	0.476	0.095	0.111	0.200
4	0.238	0.087	0.137	0.366
	0.357	0.086	0.130	0.240
	0.476	0.095	0.120	0.199
5	0.238	0.069	0.127	0.290
	0.357	0.077	0.105	0.216
	0.476	0.072	0.094	0.152
6	0.116	0.096	0.143	0.824
	0.349	0.100	0.121	0.286
	0.581	0.099	0.097	0.171
7	0.183	0.062	0.140	0.339
	0.211	0.064	0.132	0.306
	0.289	0.067	0.106	0.232

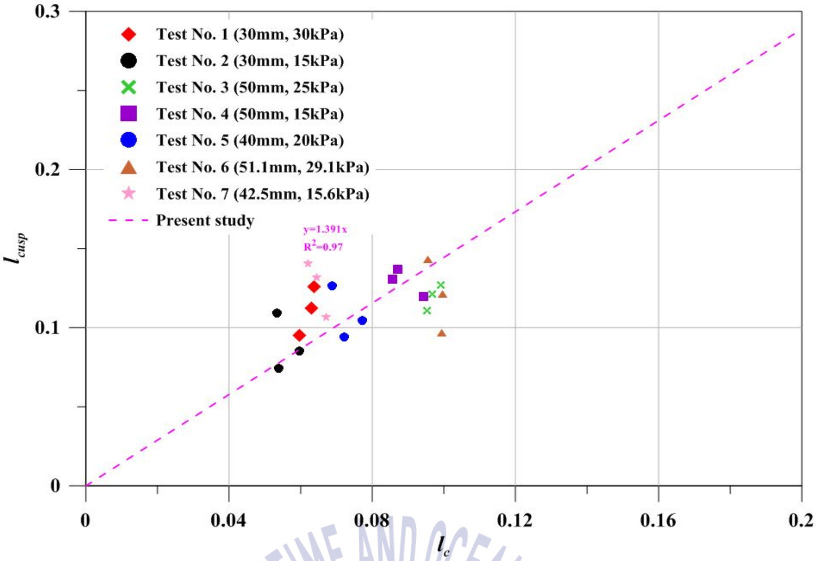

Fig. 37 The relation between the depth of ice cusps and the characteristic length of ice

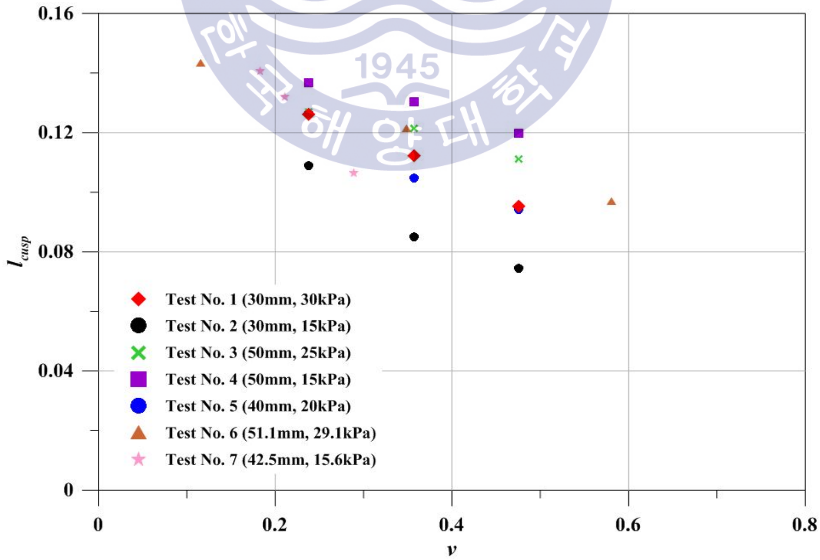

Fig. 38 The relation between the depth of ice cusps and the ship speed

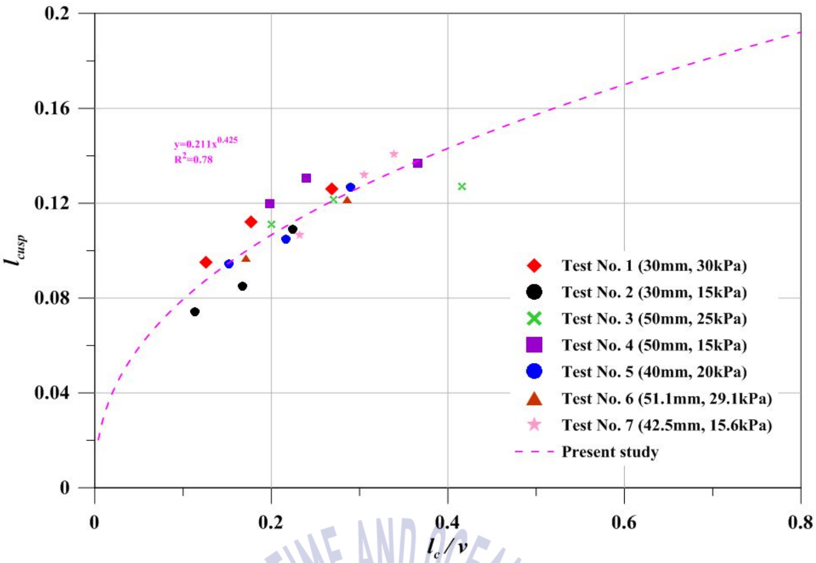

Fig. 39 The relation between the depth of ice cusps and the ratio of the characteristic length of ice and the ship speed

4.2.2 Effect of Number of Ice Cusps

The magnitude of crushing and breaking components can be affected by the icebreaking pattern and is related to the number of ice cusps in the calculation. The characteristics of these components for the number of ice cusps are considered for the Korean icebreaker model. Figure 40 shows the magnitude of these components for the number of ice cusps.

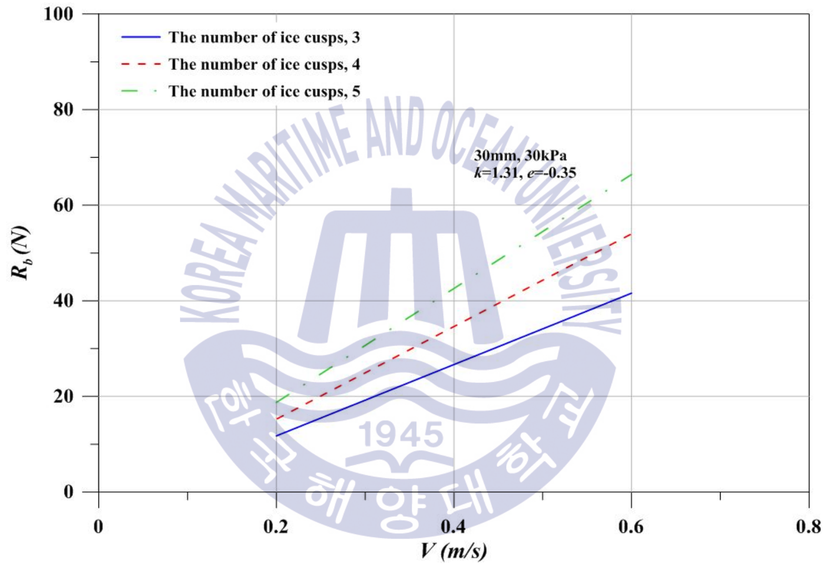

Fig. 40 The relationship between the magnitude of crushing and breaking components and the number of ice cusps for the Korean icebreaker model

In Fig. 40, when the number of ice cusps increases, the crushing and breaking components also increase. This phenomenon is caused by the ice-hull interaction. During the icebreaking process, the crushing and breaking components are associated with the contact area. When the contact area increases, the momentum energy also increases; therefore, these components will increase in this phase. In the calculation, the average number of ice cusps is 4.01 and 4.00 at the portside and starboard sides along the waterline from bow to maximum beam breadth. The number of ice cusps for the parameters (namely k and e) in the pressure-area effect is summarized in Table 4. Herein, there are no significant connections between these parameters and the number of ice cusps during ice-hull interaction.

Table 4 The number of ice cusps with various ice thicknesses and strengths in the calculation

Test No.	k	e	The number of ice cusps	
			Port	Stbd.
1	0.99	-0.55	3.99	4.00
	1.14	-0.45	4.02	4.01
	1.31	-0.35	3.98	3.99
	1.5	-0.25	4.01	3.99
	1.72	-0.15	4.01	4.00
2	0.99	-0.55	4.00	4.01
	1.14	-0.45	4.02	4.00
	1.31	-0.35	4.00	4.01
	1.5	-0.25	4.00	4.00
	1.72	-0.15	4.01	3.98
3	0.99	-0.55	4.00	4.01
	1.14	-0.45	4.01	4.00
	1.31	-0.35	4.00	3.97
	1.5	-0.25	3.99	3.99
	1.72	-0.15	4.01	4.01
4	0.99	-0.55	4.03	4.02
	1.14	-0.45	4.03	4.02
	1.31	-0.35	4.02	3.98
	1.5	-0.25	4.03	3.99
	1.72	-0.15	3.99	4.01
5	0.99	-0.55	4.05	3.99
	1.14	-0.45	4.01	4.01
	1.31	-0.35	4.01	4.01
	1.5	-0.25	4.01	4.01
	1.72	-0.15	3.99	4.00
Average			4.01	4.00

4.2.3 Open-water and Ice Resistance Characteristics

Before the ice test, a bollard pull test and an open-water resistance test were conducted in ice-free water. In the bollard pull test, the model ship was fixed on the towing carriage and the towing force was measured for different propeller revolutions at the zero speed condition of the model ship. In the open-water resistance test, the model ship speed was less than 2.0 m/s (about 17.0 knots in full scale). The bollard pull results and open-water resistance characteristics are summarized in Table 5 and depicted in Figs. 41 to 44.

Table 5 Bollard pull results for the design draft condition

Hull Form No.	N^2 $(1/n^2)$	T (N)	Q (N)	TF (N)	P_D (W)
1	1	2.04	0.06	1.82	0.36
	9	16.02	0.51	10.44	9.71
	25	45.19	1.40	41.41	43.98
	49	89.21	2.74	89.07	120.44
	81	148.06	4.49	145.91	254.13
	121	223.78	6.72	218.02	464.44
2	1	1.67	0.10	1.66	0.62
	9	16.51	0.56	14.32	10.60
	25	44.95	1.31	42.07	41.07
	49	86.44	2.64	84.56	115.90
	81	148.63	4.38	141.12	247.66
	121	221.60	6.52	219.12	450.56

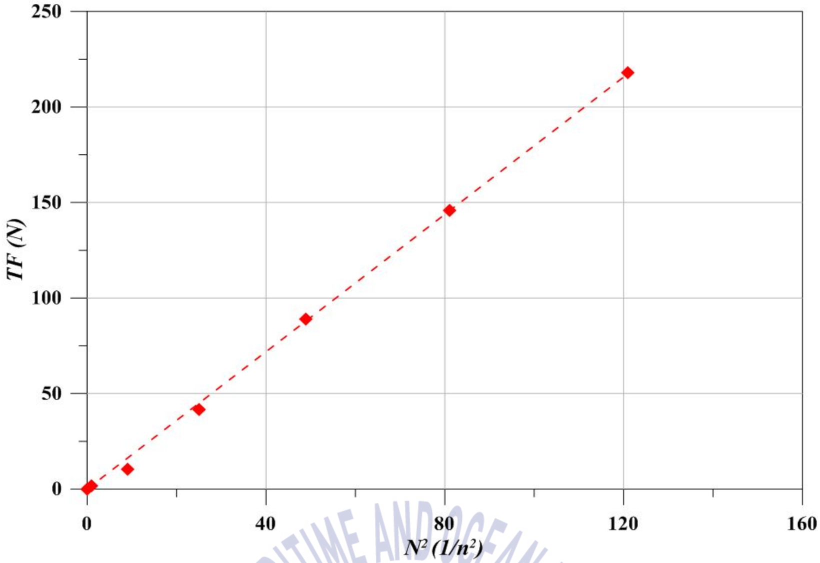

(a) TF vs N

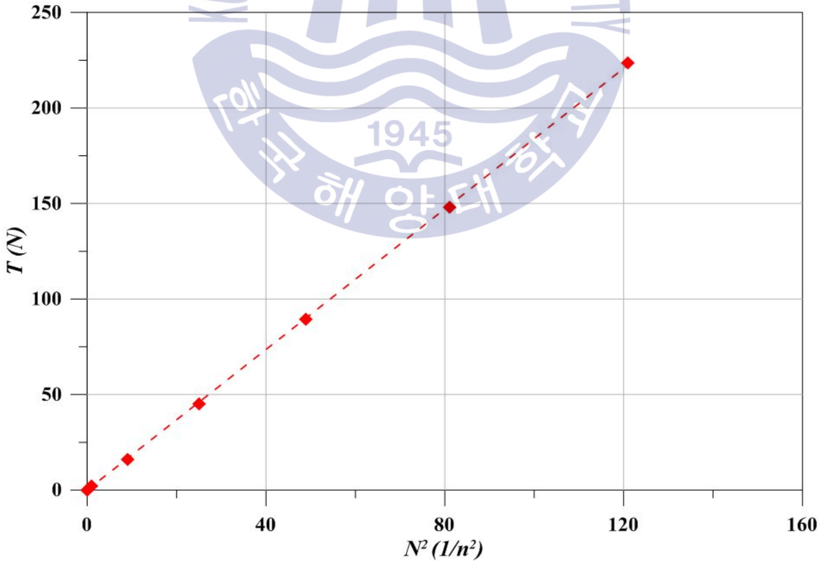

(b) T vs N

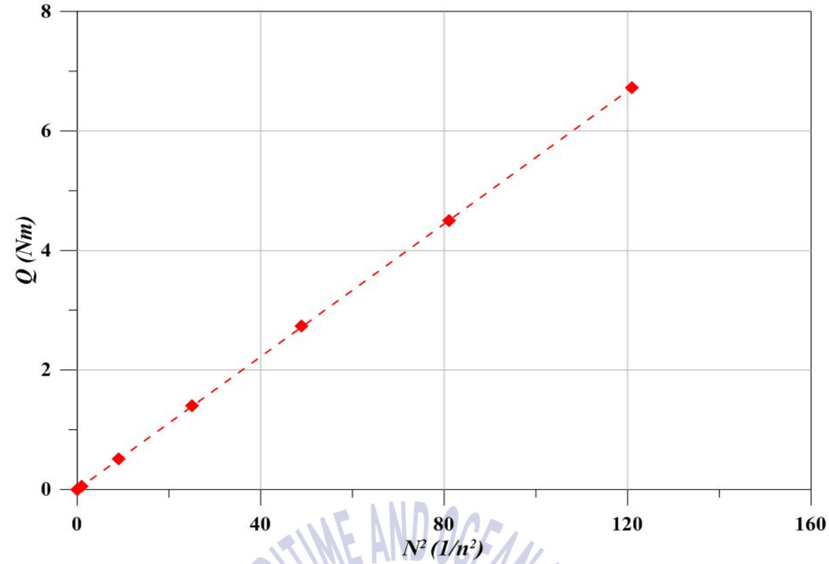

(c) Q vs N

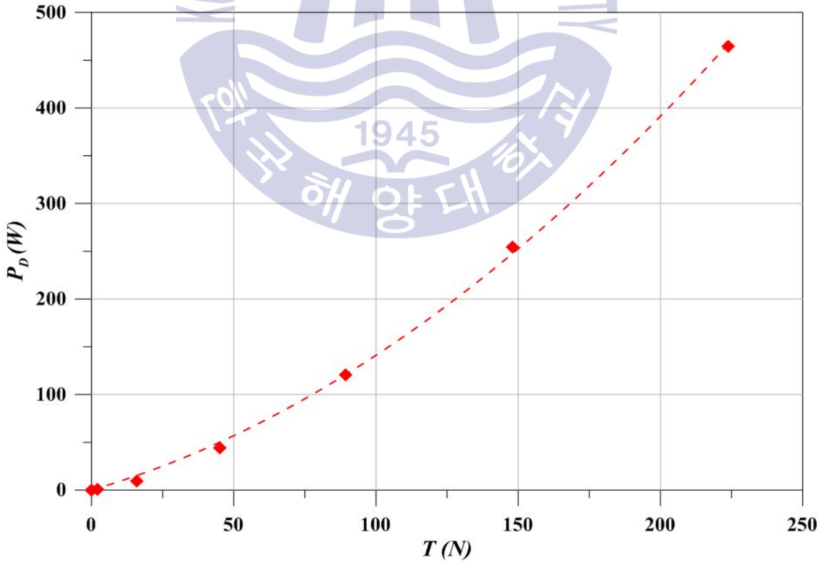

(d) P_D vs T

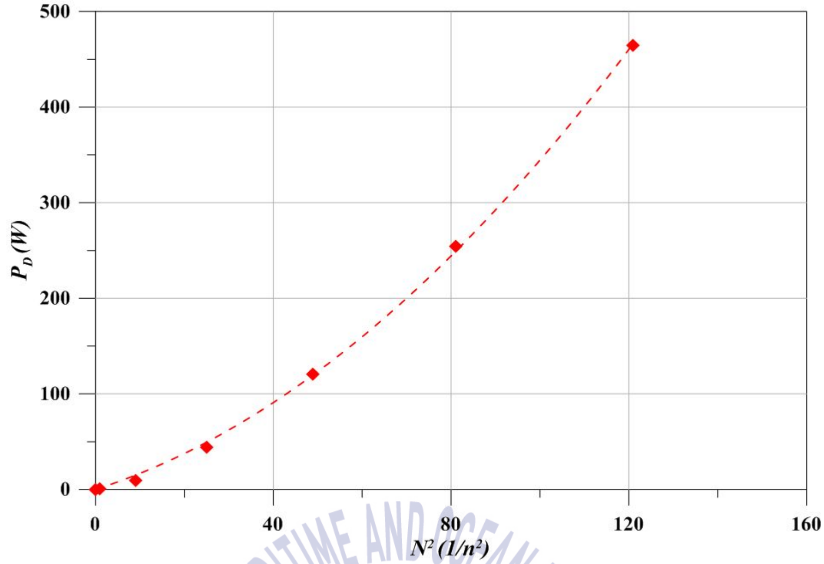

(e) P_D vs N

Fig. 41 Results of bollard pull test for the Korean icebreaker model

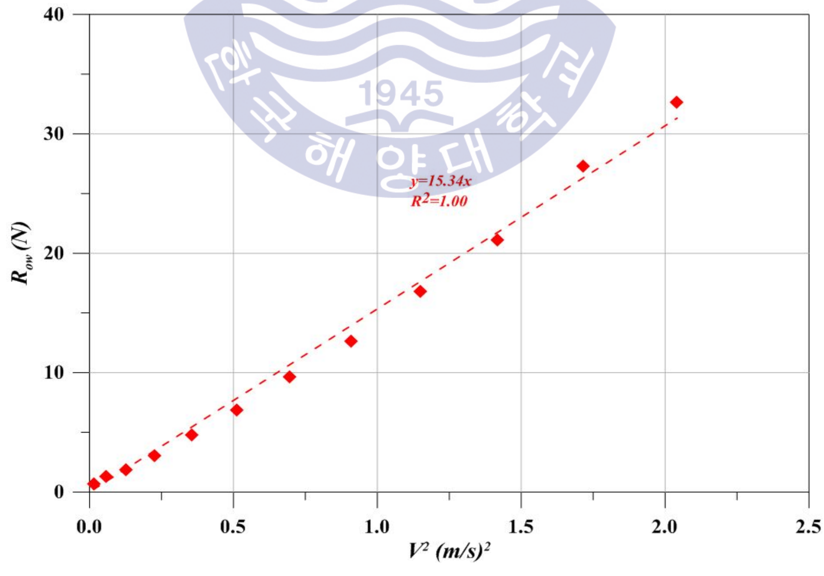

Fig. 42 Results of open-water test for the Korean icebreaker model

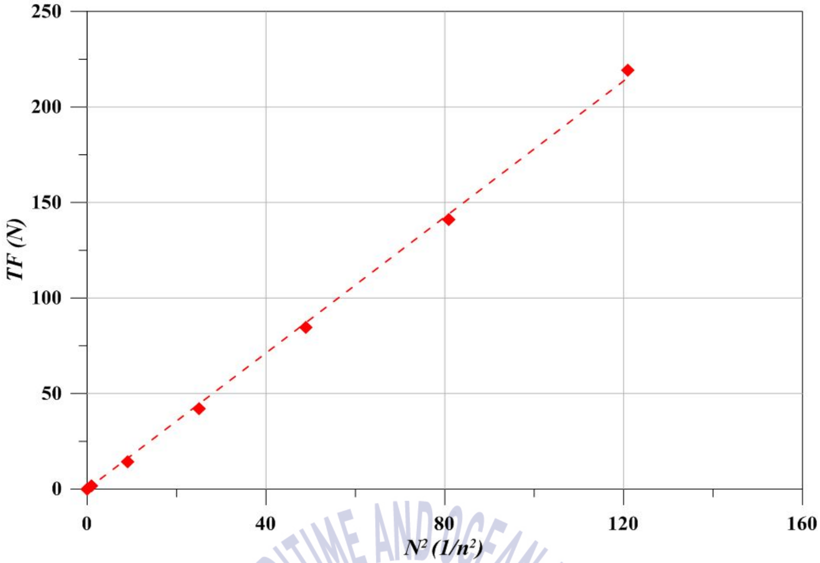

(a) TF vs N

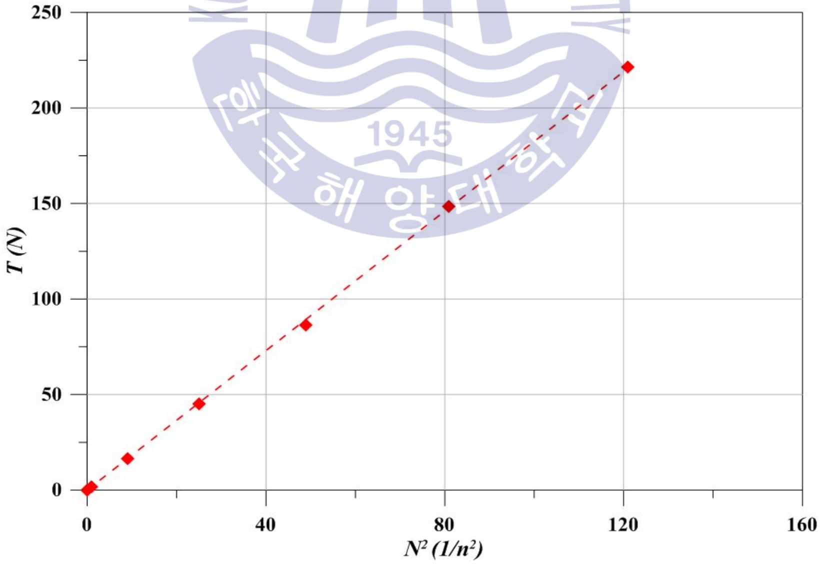

(b) T vs N

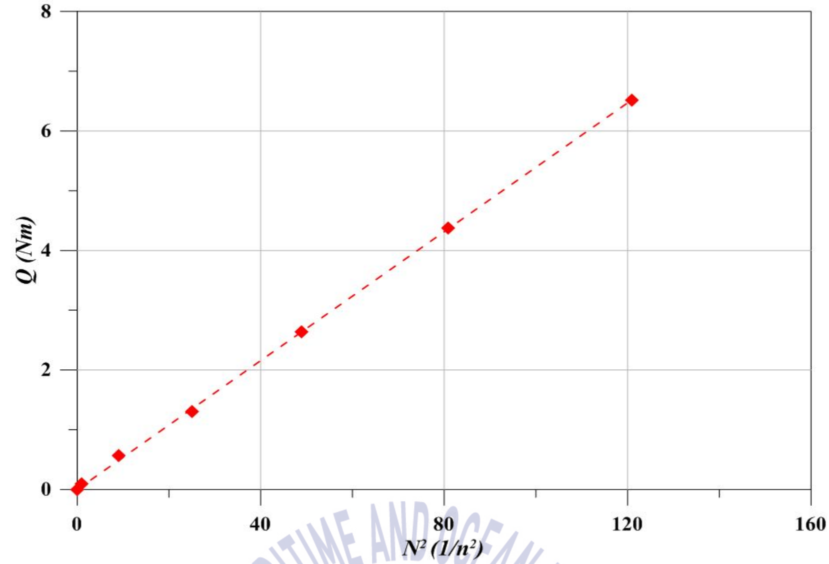

(c) Q vs N

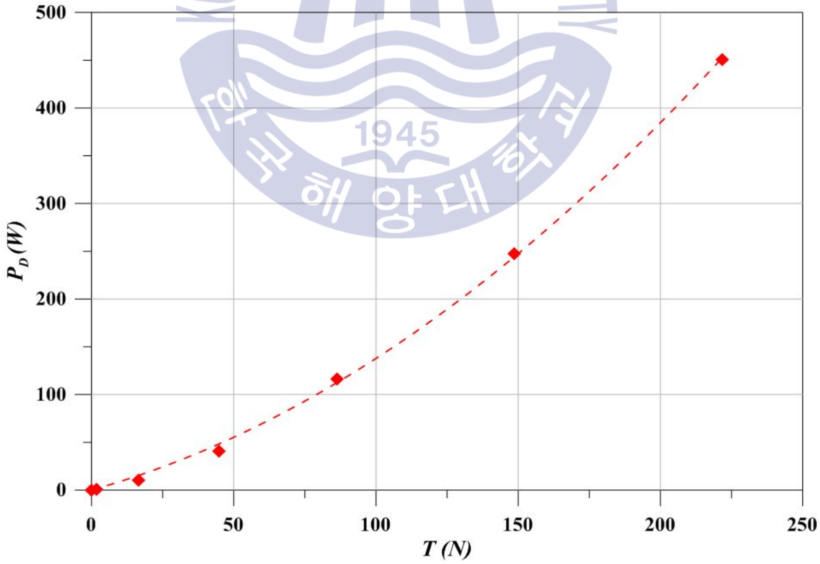

(d) P_D vs T

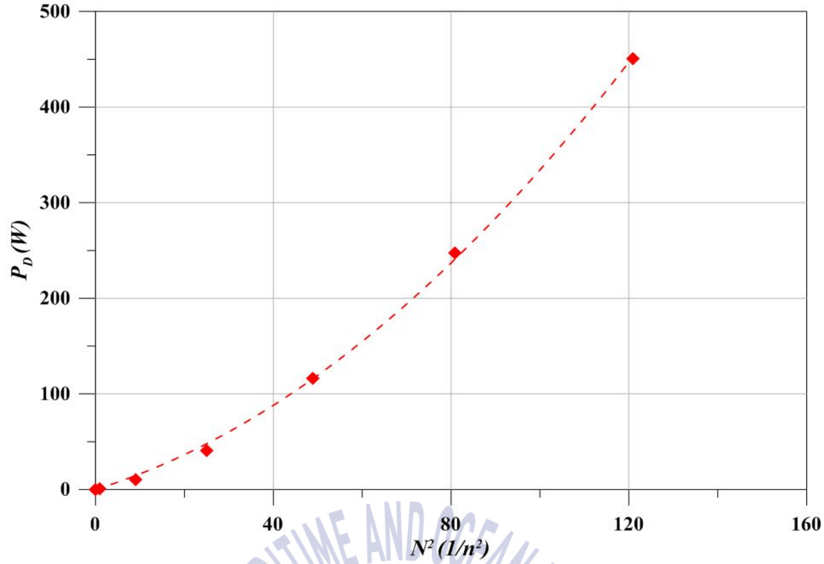

(e) P_D vs N

Fig. 43 Results of bollard pull test for the Arctic PSV model

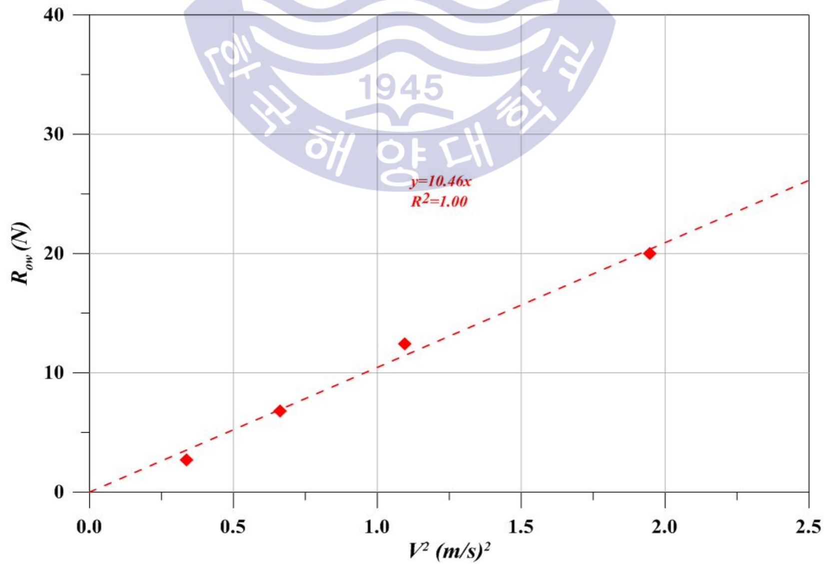

Fig. 44 Results of open-water test for the Arctic PSV model

The model tests were conducted at ship speeds of 0.238, 0.357, and 0.476 m/s (2, 3, and 4 knots in full scale) for the Korean icebreaker model and 0.116, 0.349, and 0.581 m/s (1, 3, and 5 knots in full scale) for the Arctic PSV model. The ice model test results are summarized in Table 6. The characteristics of ice resistance and Froude number for ice thickness and strength are depicted in Fig. 45. Generally, the magnitude of ice resistance is related to ice thickness and strength. When the ice is thick, the difference of ice resistance for ice strength is much larger than for thin ice. It is shown that ice thickness is a more significant variable than ice strength in ice resistance. In the simulation, ice-hull contact mainly involves triangular crushing. Quadrilateral crushing rarely occurs when ice is thin or when ship speeds are high.

Figures 46 and 47 show the model test results in level ice and pre-sawn ice conditions. In Fig. 46, the ratio of pre-sawn ice resistance in total resistance is approximately 40 %; therefore, the proportion of the breaking resistance is 60 % in total resistance in ice. Enkvist (1983) mentioned that the breaking resistance was more important than other resistance components in a full-scale prediction. But the ratio of pre-sawn ice resistance in total resistance is about 70 % in Fig. 47. It is shown that this difference resulted from the hull forms. The PSV model has a wider beam and smaller bow angle than the Korean icebreaker model; thus, this bow form has more efficient icebreaking performance during the ice and hull interaction than does the Korean icebreaker model. Figures 48 and 49 show the model test in level ice and pre-sawn ice conditions, and Figures 50 and 51 show a photograph of the bow and stern in the model test.

Table 6 Ice model test results for the design draft condition (corrected values)

Test No.	V (m/s)	R^{level} (N)	$R^{pre-sawn}$ (N)
1	0.238	89.74	30.43
	0.357	109.02	44.80
	0.476	132.03	56.88
2	0.238	69.07	-
	0.357	93.49	
	0.476	117.88	
3	0.238	196.21	-
	0.357	228.69	
	0.476	273.57	
4	0.238	146.11	-
	0.357	185.76	
	0.476	211.14	
5	0.238	116.22	41.16
	0.357	139.19	57.79
	0.476	170.78	73.21
6	0.116	97.17	65.54
	0.349	127.27	85.64
	0.581	159.59	119.50

$x = 1.55$, $a = 0.66$, $b = 0.34$ in the correction for Test No. 1 to 5

$x = 1.37$, $a = 0.66$, $b = 0.34$ in the correction for Test No. 6

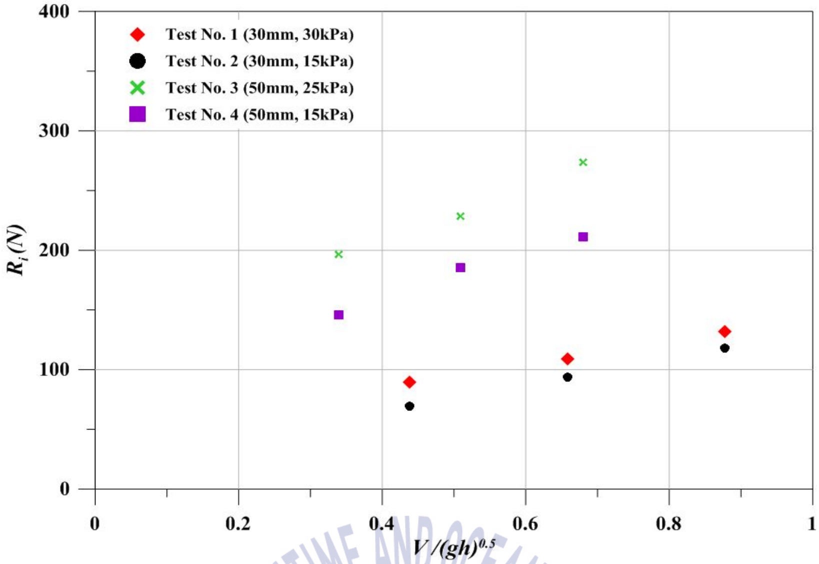

Fig. 45 The characteristics of ice resistance of the Korean icebreaker model for different ice thicknesses and strengths

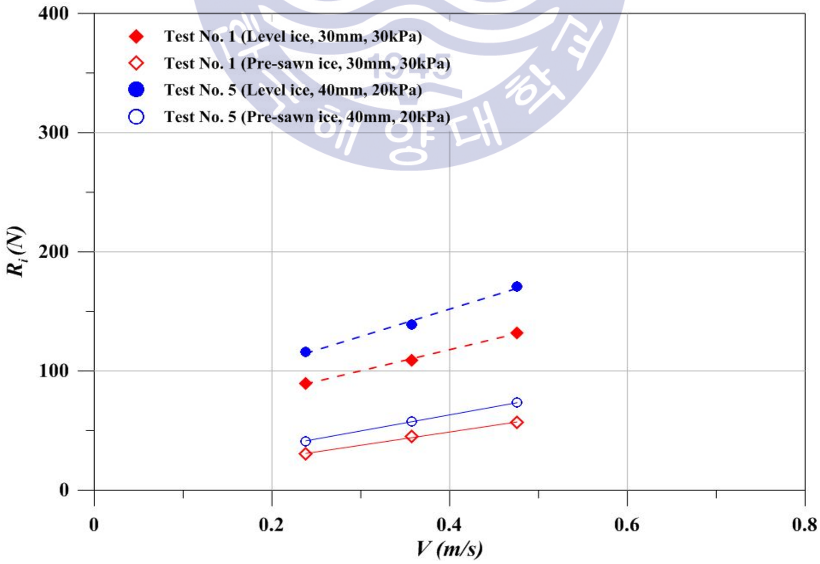

Fig. 46 Level ice and pre-sawn ice resistance results of the Korean icebreaker model for two different ice thicknesses and strengths

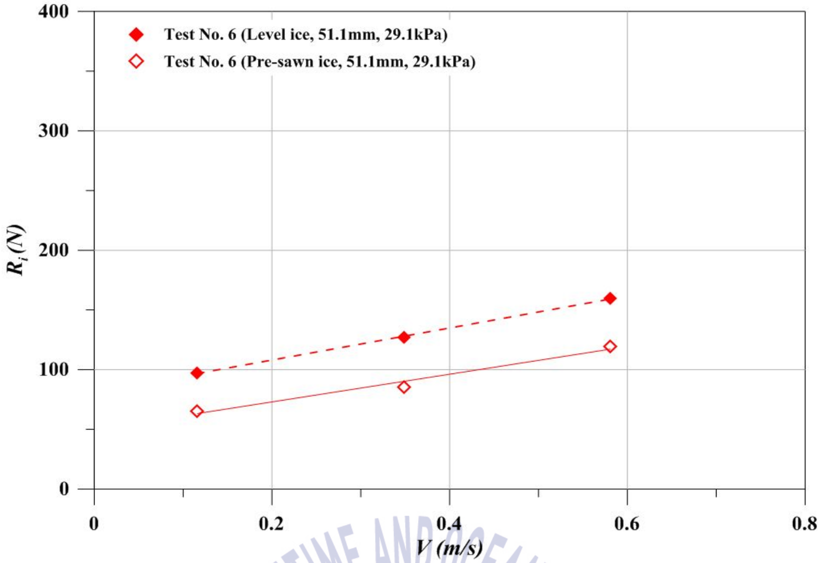

Fig. 47 Level ice and pre-sawn ice resistance results of the Arctic PSV model

(a) Level ice condition

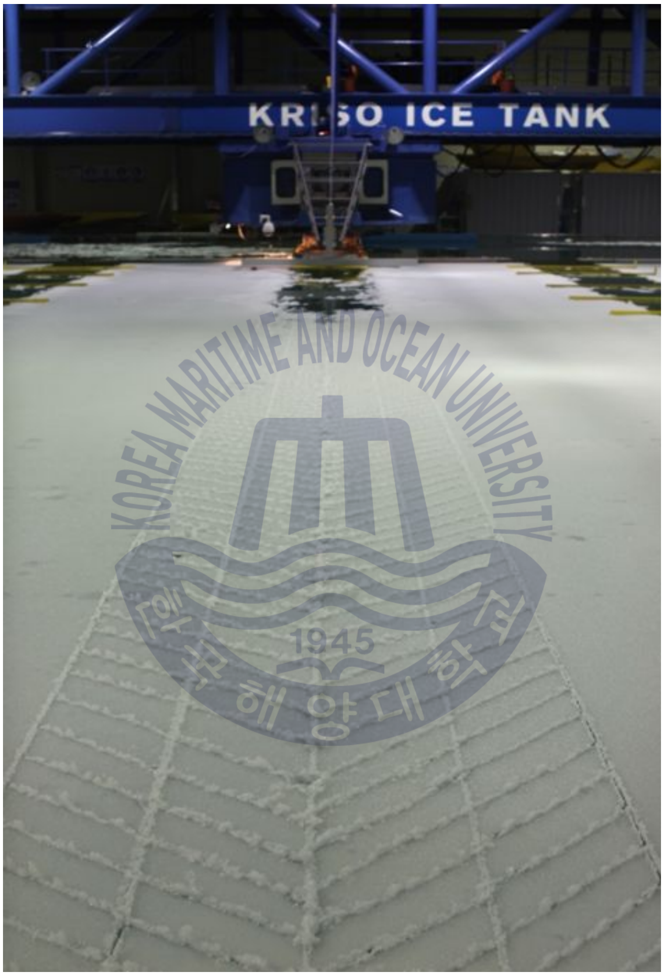

(b) Pre-sawn ice condition

Fig. 48 Model test in level ice and pre-sawn for the Korean icebreaker model

(a) Level ice condition

(b) Pre-sawn ice condition

Fig. 49 Model test in level ice and pre-sawn ice for the Arctic PSV model

(a) Bow

(b) Stern

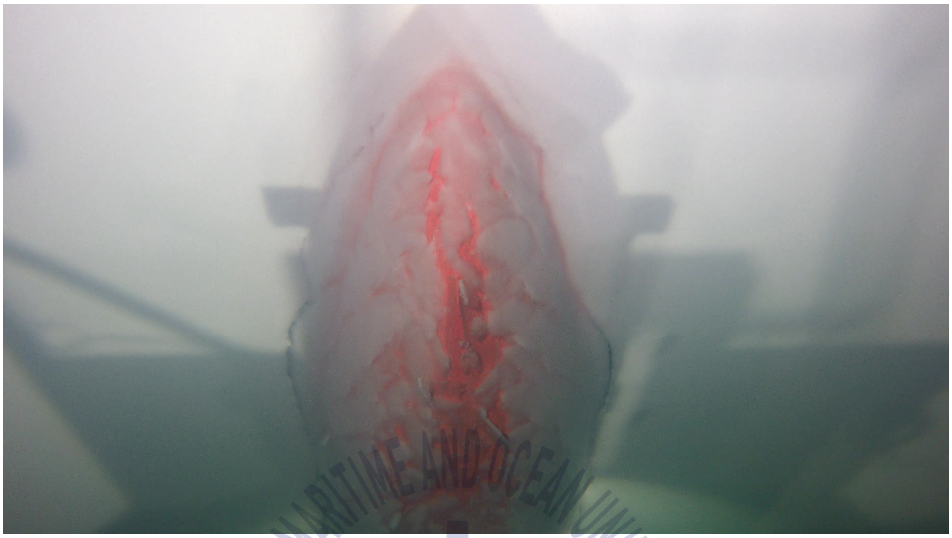

(c) Bow (underwater condition)

(d) Stern (underwater condition)

Fig. 50 Photographs of running model ship of the Korean icebreaker in the towed propulsion test

(a) Bow

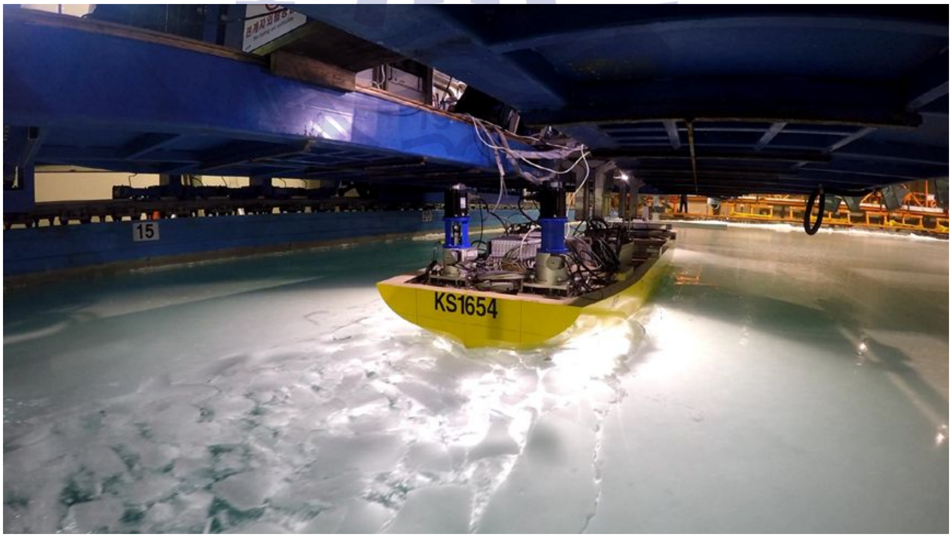

(b) Stern

(c) Bow (underwater condition)

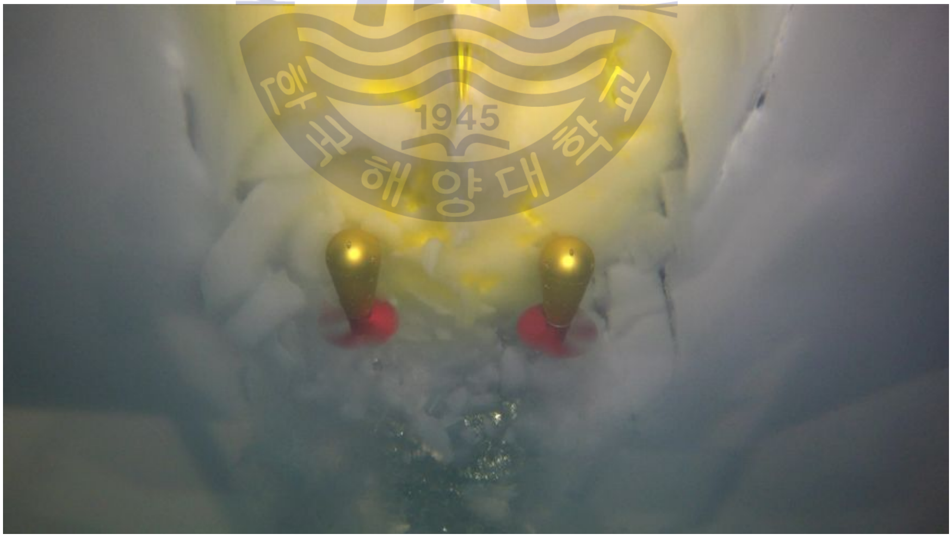

(d) Stern (underwater condition)

Fig. 51 Photographs of running model ship of the Arctic PSV in the towed propulsion test

4.2.4 Comparison of Ice Resistance between Predictions and Test Results

The predictions for the present model and the model test results are shown in Figs. 52 to 56. When the ice thickness is 30 mm and the ice strength is 30 kPa, a good relationship is obtained from k=1.31 and e=−0.35 in Fig. 52. At 30 mm thick and 15 kPa strength, the predictions show good agreement with the model test results for k=1.50 and e=−0.25 expect 0.476 m/s (see Fig. 53). When k and e are 0.99 and −0.55, the predictions show relatively good agreement with the model test results expect 0.357 m/s in Fig. 54. In this case, a good correlation between the predictions and the model test results will be shown by a small values of k and e. In Fig. 55, the predictions show good agreement with the model test results for k=1.14 and e=−0.45.

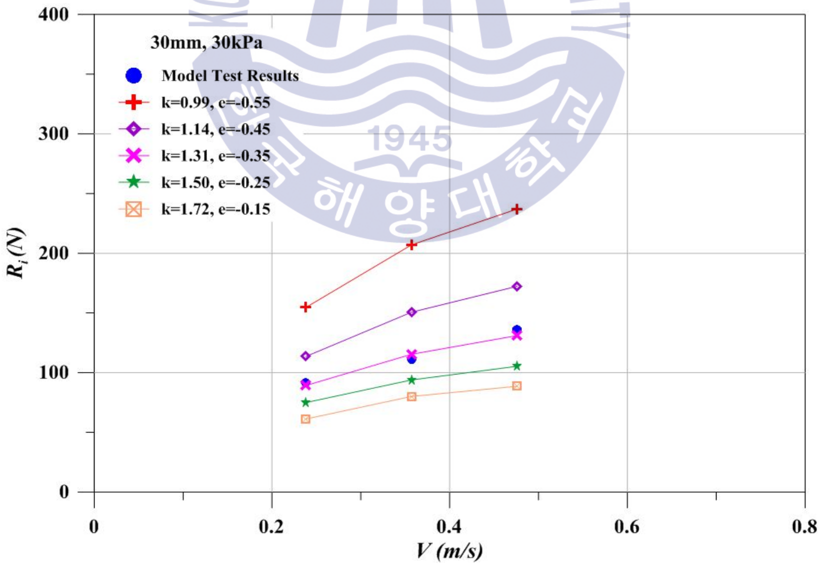

Fig. 52 Comparison of predictions and model test results for pressure-area effect parameters (Test No. 1)

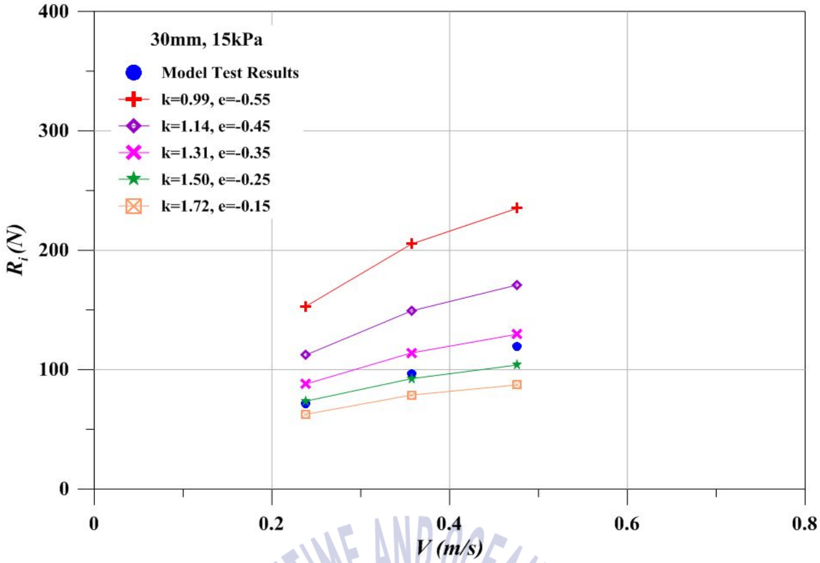

Fig. 53 Comparison of predictions and model test results for pressure-area effect parameters (Test No. 2)

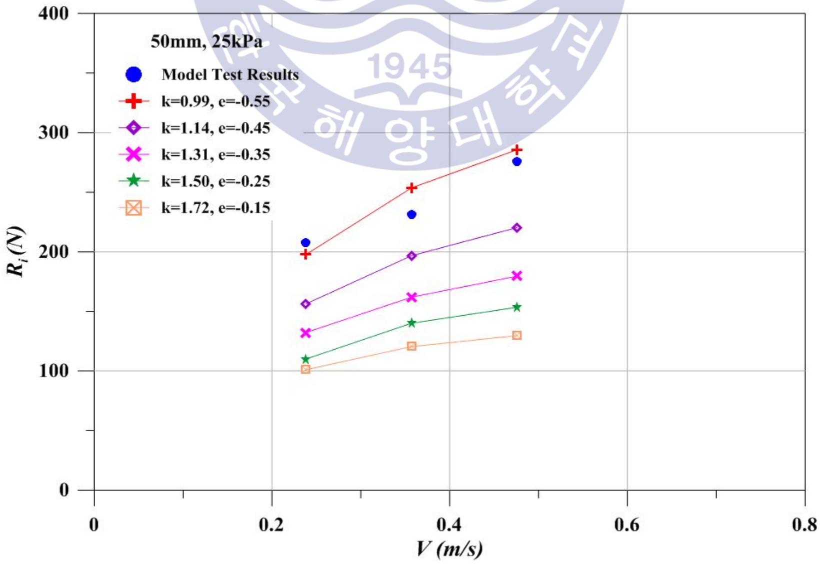

Fig. 54 Comparison of predictions and model test results for pressure-area effect parameters (Test No. 3)

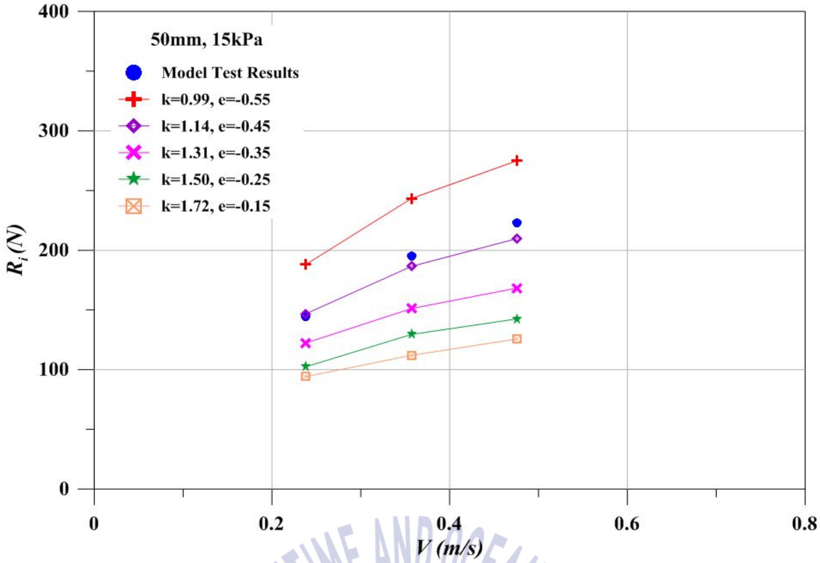

Fig. 55 Comparison of predictions and model test results for pressure-area effect parameters (Test No. 4)

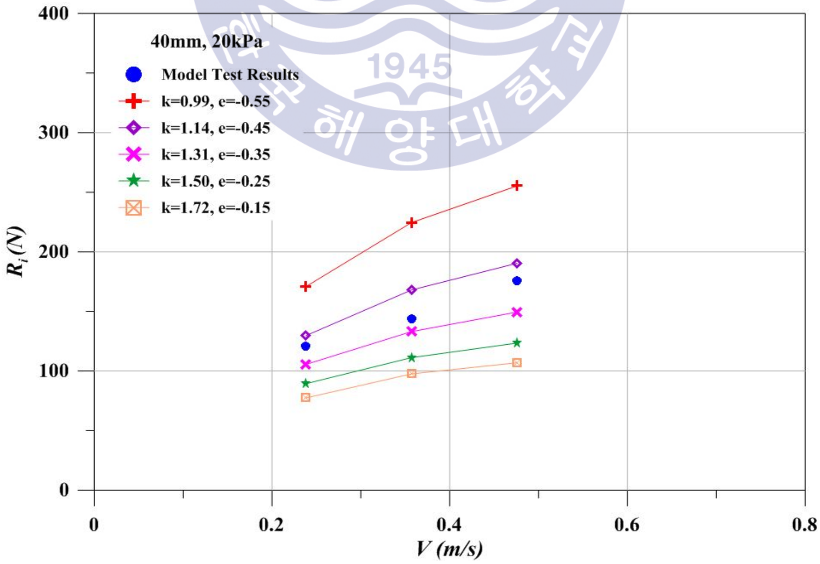

Fig. 56 Comparison of predictions and model test results for pressure-area effect parameters (Test No. 5)

In Fig. 56, when k is 1.14 and e is −0.45, the predictions show relatively good agreement with the results of the model test, expect 0.357 m/s. Based on Figs. 52 to 56, the predictions can be strongly affected by the pressure-area effect. When the ice is thick, the contact area increases during ice and hull inter-actions, and the ice pressure dramatically decreases. In particular, when the k and e increase, conversely, the ice resistance decreases. The values of k and e are intimately associated with the magnitude of ice resistance. The comparisons of model test results and calculated results derived from Lindqvist's model and present model are depicted in Figs. 57 to 59. When k is 1.53 and e is between −0.49 and −0.25, the predictions show relatively good agreement with the model test results.

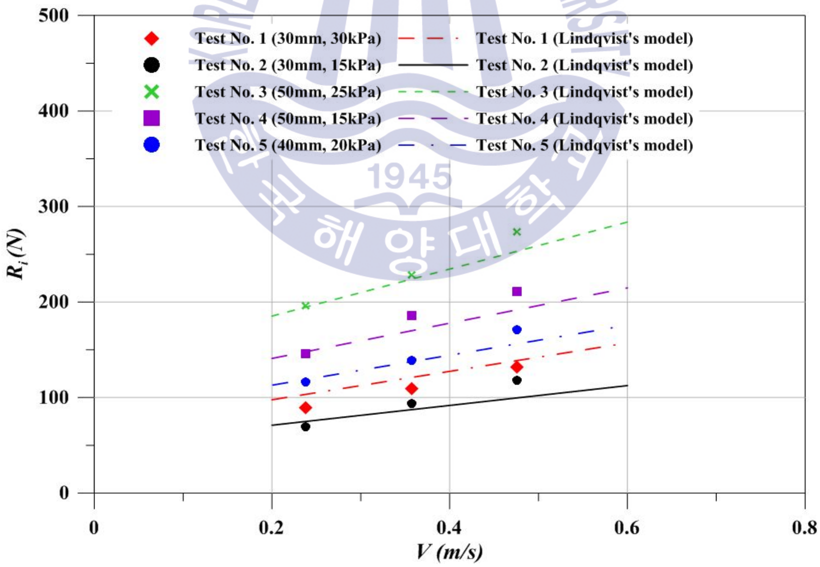

Fig. 57 Comparison of model test results and calculated results using Lindqvist's model for the Korean icebreaker model

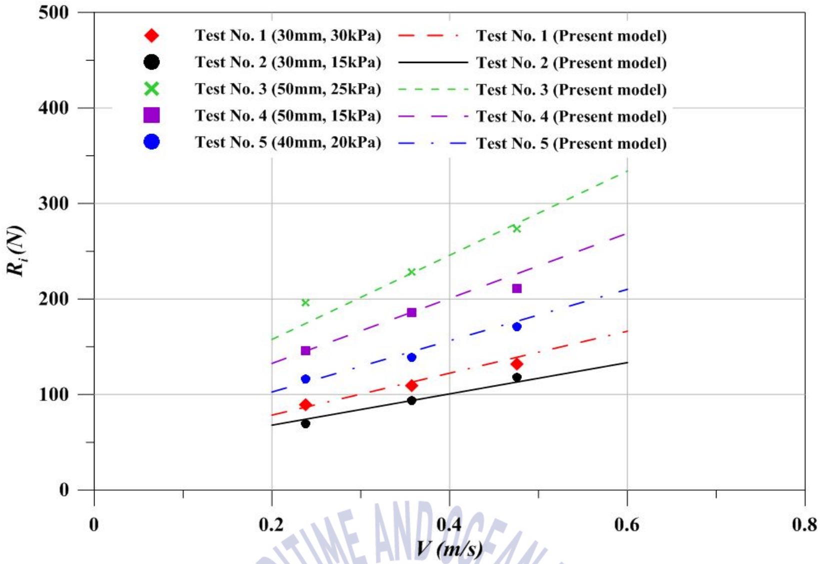

Fig. 58 Comparison of model test results and calculated results using present model for the Korean icebreaker model

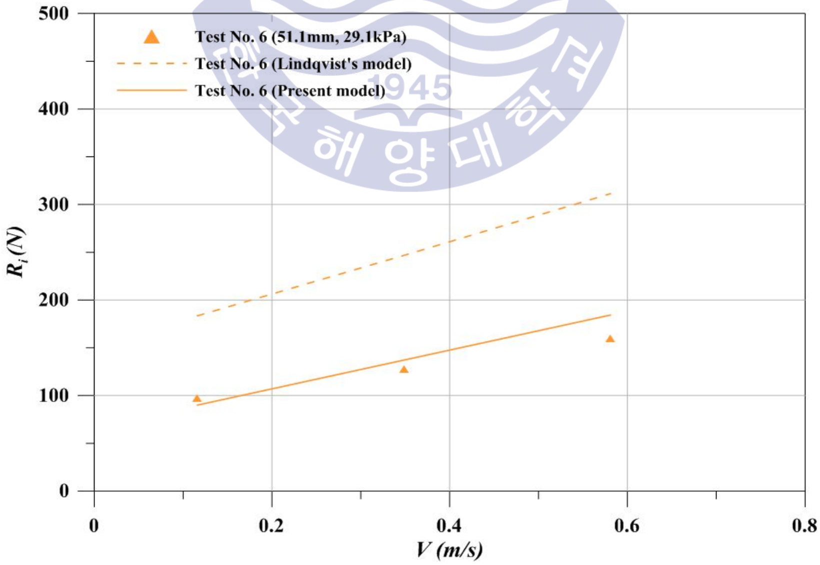

Fig. 59 Comparison of model test results and calculated results using both Lindqvist's model and present model for the Arctic PSV model

In addition, the deviation, δ, is calculated to examine uncertainty in the predictions. The accuracy of the predictions can be quantified by calculating the deviation as follows:

$$\delta = \left[\frac{R^{1,2}_{predictions} - R_{measured}}{R_{measured}} \right] \times 100 \tag{53}$$

where $R^{1}_{predictions}$ denotes the predictions derived from the present model and $R^{2}_{predictions}$ denotes the predictions derived from the Lindqvist's model, respectively. $R_{measured}$ denotes the ice model test results.

A large deviation demonstrates that the predictions are widely scattered, a small deviation indicates that the predictions are closely scattered around the model test results, and a negative deviation indicates that the predictions are less than the model test results. The calculated deviations for the present model and the Lindqvist's model are summarized in Tables 7 and 8. Herein, the deviation of the present model is slightly smaller than that in the Lindqvist's model. There are large deviations in some cases, as shown in Table 7. This can be caused by model test uncertainties. Actually, the model test results show a some variance in Fig. 57 and thus led to large deviations.

Table 7 Calculated deviation for the present model and the Lindqvist's model for the Korean icebreaker model

Test No.	V (m/s)	$R^1_{predictions}$ (N)	$R^2_{predictions}$ (N)	$R_{measured}$ (N)	Deviation, δ (%)	
1	0.238	86.99	103.32	89.74	-3.1	15.1
	0.357	112.58	121.01	109.02	3.3	11.0
	0.476	139.25	138.69	132.03	5.5	5.0
2	0.238	74.33	74.94	69.07	7.6	8.5
	0.357	93.29	87.28	93.49	-0.2	-6.6
	0.476	113.29	99.62	117.88	-3.9	-15.5
3	0.238	174.46	194.65	196.21	-11.1	-0.8
	0.357	226.84	223.92	228.69	-0.8	-2.1
	0.476	279.37	253.20	273.57	2.1	-7.4
4	0.238	145.67	147.95	146.11	-0.3	1.3
	0.357	185.79	169.91	185.76	0.0	-8.5
	0.476	226.72	191.88	211.14	7.4	-9.1
5	0.238	113.02	118.88	116.22	-2.8	2.3
	0.357	144.49	137.55	139.19	3.8	-1.2
	0.476	177.00	156.22	170.78	3.6	-8.5
average, $\lvert\delta\rvert$					3.7	6.9

$k = 1.53$ and $e = -0.33$ for Test No. 1

$k = 1.53$ and $e = -0.25$ for Test No. 2

$k = 1.53$ and $e = -0.49$ for Test No. 3

$k = 1.53$ and $e = -0.42$ for Test No. 4

$k = 1.53$ and $e = -0.37$ for Test No. 5

In Table 8, a large deviation occurs in Lindqvist's model (see Fig. 59), because Lindqvist's model considered the wedged bow shape. As mentioned before, the breaking resistance constitutes a large portion of the total resistance in ice. In this case, when calculating the crushing and breaking components for the spoon bow shape, large deviations can occur. There are some differences between the predicted results from the present model and the ice model test results because of the parameters of the pressure-area effect, but the predicted results show small deviation; thus, present model can give reasonable results in ice resistance prediction.

Table 8 Calculated deviation for the present model and the Lindqvist's model for the Arctic PSV model

Test No.	*V (m/s)*	$R^1_{predictions}$ *(N)*	$R^2_{predictions}$ *(N)*	$R_{measured}$ *(N)*	*Deviation, δ (%)*	
6	0.116	93.02	183.46	97.17	-4.3	88.8
	0.349	131.06	246.88	127.27	3.0	94.0
	0.586	187.37	311.38	159.59	17.4	95.1
average, $\lvert\delta\rvert$					8.2	92.6

$k = 1.53$ and $e = -0.34$ for Test No. 6

The ship performance in ice can be determined by the relationship between ice thickness and ship speed as an h-v curve. Herein, h denotes the ice thickness and v denotes the ship speed. The simulated h-v curve for the Korean icebreaker Araon is given in Fig. 60.

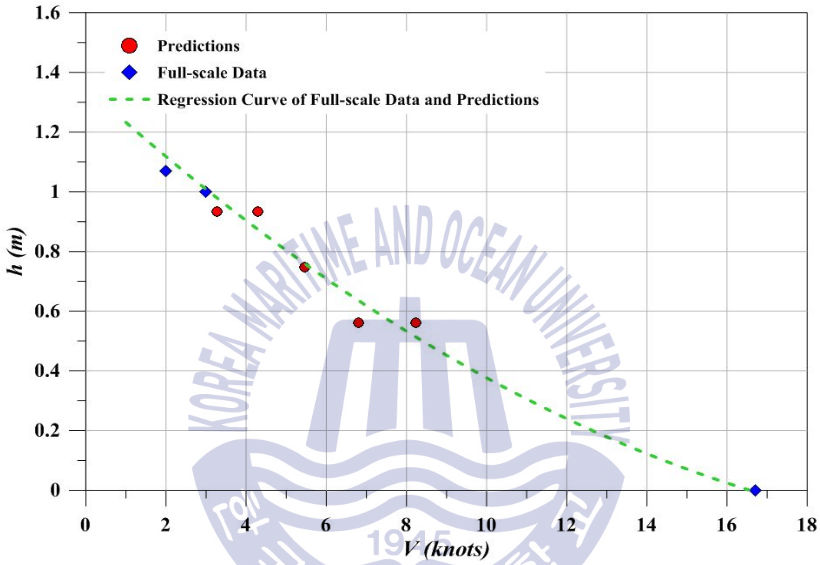

Fig. 60 The simulated h-v curve for the Korean icebreaker Araon

The ice trial of the Korean icebreaker, Araon was conducted by the Arctic and Antarctic Research Institute (AARI) in the Antarctic Ocean in 2010 (AARI, 2010). In Fig. 60, the simulated results denote that the Korean icebreaker, Araon practically satisfies the design icebreaking capacity in continuous icebreaking mode.

Chapter 5 Conclusions and Recommendations

Ice resistance prediction methods are investigated, and a numerical model is developed based on the icebreaking patterns and ice-hull contact conditions. This model can determine the ice resistance of a ship during head-on collisions with level ice and incorporates the crushing, breaking, and submersion components associated with ship performance in ice. In this chapter, the main findings are summarized.

5.1. Conclusions

1) The magnitude of the ice resistance is related to ice thickness and strength. When the ice is thick, the differences of ice resistance for ice strength are much larger than for thin ice. It is shown that ice thickness is a more significant variable in ice resistance prediction than the strength of the ice.

2) The icebreaking pattern can be associated with the ice thickness and ship speed, and it can significantly affect ship resistance in ice. The relation between the depth of ice cusps and the characteristic length of ice can be assumed to be a linear relation, while the depth of ice cusps and the ship speed are inversely proportional. These relations should be attributable to the icebreaking phenomena. When the ship speed is low, the ice and hull contact area slowly increases, so the loading area will also slowly increase,

but at higher speeds, the contact area will increase in a shorter time. In such a case, the depth of the ice cusps will decrease. As a result, the depth of the ice cusps has a decreasing tendency in the higher speed regions.

3) The proportion of the breaking resistance component is commonly higher than other resistance components, but this ratio can be affected by the hull form. In the wide beam and sharp bow form, the breaking resistance is lower than expected. Accordingly, hull form information should be considered in the breaking resistance calculation. In addition, the magnitude of crushing and breaking components can be affected by the number of ice cusp formations. When the number of ice cusps increases, the crushing and breaking components also increase. This phenomenon is caused by the ice-hull interaction. During the icebreaking process, these components are associated with the contact area. When the contact area increases, the momentum energy also increases; therefore, these components will increase during this phase. However, there are no significant connections between the parameters in the pressure-area effect and the number of ice cusps.

4) The failure phenomena of ice sheets consist of two main aspects—the crushing/shearing and the bending/buckling of an ice wedge. With respect to the failure of the wedge plate, the empirical parameter should be determined. It is strongly associated with the magnitude of the ice resistance components. In particular, the empirical parameter may be affected by the strength number and the Froude number, because the empirical parameter should be related to the strength of the ice. Therefore, both the strength number and the Froude number should be considered in the

calculation. In the simulation, ice-hull contact conditions mainly involve triangular crushing, while quadrilateral crushing rarely occurs. In the full-scale condition, the dominant phenomenon should be triangular crushing.

5) The pressure-area effect is an important aspect of the prediction of ice resistance. When the ice is thick, the contact area increases during ice and hull interactions, and the ice pressure dramatically decreases. In particular, when the k and e increase, conversely, the ice resistance decreases. The values of k and e are intimately associated with the magnitude of ice resistance. When k is 1.53 and e is between -0.49 and -0.25, the predictions show relatively good agreement with the ice model test results. Based on the h-v curve, the Korean icebreaker, Araon practically satisfies the performance requirements in the design condition.

Finally, defining the icebreaking pattern and the parameters used in the present study will be useful for future studies of ship performance in ice. The detailed procedures of the model test can also help in analyzing the model test results. In addition, the developed numerical model can contribute to the tests in the KRISO ice tank by helping to predict the ice resistance of vessels, given various ice conditions and hull forms.

5.2. Recommendations

This study is intended to facilitate the prediction of ice resistance for vessels in level ice conditions, using the icebreaking patterns and the ice-hull contact conditions. The developed model focuses on predicting ship resistance in ice and only considers a 3-DOF mode. In particular, new semi-empirical icebreaking patterns are derived from the model tests results in the ice tank of KRISO, the pressure-area effect is considered, and reference pressure and area are determined from the full-scale ice trial data for the Korean icebreaker, Araon. To determine the failure criteria of ice, the relationship between the strength number and the Froude number is used. Recommendations for future studies are summarized below.

1) The maneuvering performance in ice is also a significant issue; therefore, future studies should focus on evaluating maneuvering performance and ice resistance prediction.

2) The icebreaking pattern can be characterized by ice properties, hull forms, and a ship’s operating conditions; therefore, the datasets of ice cusp formation can provide more accurate information about the characteristics of the icebreaking pattern.

3) Contact force is very sensitive to the pressure-area relationship; therefore, further model/full-scale data is needed to determine the coefficients in the pressure-area equation. Ice load measurements in the model-scale using a tactile sensor will facilitate understanding of the pressure-area effect.

4) Further verifications of the present ice resistance prediction method for various hull forms are needed to improve the degree of accuracy of the present model, and a correlation analysis between the model and full-scale data should be conducted to verify the effectiveness of the present model.

References

Aksnes, V., 2010. A simplified interaction model for moored ships in level ice. *Cold Regions Science and Technology*, Vol. 63, pp. 29-39.

Arctic and Antarctic Research Institute (AARI), 2010. *Full-scale ice trials of the Korean research icebreaker Araon*, St. Petersburg. 127 pp.

Daley, C.G., 1999. Energy based ice collision forces. *Proceedings of the 15th International Conference on Port and Ocean Engineering under Arctic Conditions* (POAC), Vol. 2, pp. 674-686.

Enkvist, E., 1972. *On the Ice Resistance Encountered by Ships Operating in the Continuous Model of Icebreaking*. Swedish Academy of Engineering Sciences, Finland-Helsinki.

Enkvist. E., 1983. A survey of experimental indications of the relation between the submersion and breaking components of level ice resistance to ships. *Proceedings of the 7th International Conference on Port and Ocean Engineering under Arctic Conditions* (POAC), pp. 484-493.

Edwards, R.Y., Major, R.A., Kim J.K., German, J.G., Lewis, J.W., & Miller, D.R., 1976. Influence of major characteristics of icebreaker hulls on their powering requirements and maneuverability in ice. *Society of Naval Architects and Marine Engineers (SNAME) Transactions*, Vol. 84, pp. 364-407.

Edward, R.Y., & Nawwar, A.M., 1978. *Compilation and Analysis of Recent Icebreaking Model Test Data of a World-wide Variety of Hull Forms*, ACL Report 211C for Transport Canada R&D Centre under TP1294 Contract.

Ettema, R., Sharifi, M.B., Geogakakos, K.P., & Stem, F. 1991. Chaos in continuous-model icebreaking. *Cold Regions Science and Technology*, pp. 131-144.

Erceg, S., Ehlers, S., Polach, R. B., & Leira, B. 2014. A numerical model to initiate the icebreaking pattern in level ice. *Proceedings of the 33rd International Conference on Ocean, Offshore and Arctic Engineering*. American Society of Mechanical Engineers.

Hu, J., & Zhou, L., 2015. Experimental and numerical study on ice resistance for icebreaking vessels. *International Journal of Naval Architecture and Ocean Engineering*. Vol(7). pp. 626-639.

International Towing Tank Committee (ITTC), 2005. *Testing and extrapolation methods ice testing resistance in level ice*, Technical Report.

International Towing Tank Committee (ITTC), 2014. *Testing and extrapolation methods ice testing resistance in level ice,* Technical Report.

Jeong, S.Y., 2008. *A Study on Ice Load Estimation for Icebreaking Cargo Vessels and Ice Transit Model*. Masters of Science Thesis. Korea Maritime and Ocean University.

Jeong, S.Y., Choi, K., Cho, S.R., Kang, K.J., & Lee, C.J., 2013. A study of the resistance prediction method in level ice. *Proceedings of the 22nd International Conference on Port and Ocean Engineering under Arctic Conditions* (POAC), POAC13_075.

Jeong, S.Y., Choi, K., Kang, K.J., Cho, S.R., & Lee, C.J., 2014. A semi-empirical method of ice resistance prediction in level ice. *Proceedings of the 11th International Conference and Exhibition on Performance of Ships and Structures in Ice* (ICETECH), ICETECH14-141-RF.

Juva, M., & Riska, K., 2002. *On the power requirement in the Finnish-Swedish ice class rules*, Research Report No. 47. Technical Report, Winter Navigation Research Board, Finland and Sweden.

Kashteljan, V.I., & Ryvlin, A.Ya., 1966. The Influence of Natural Characteristic of Solid Ice in Evaluation of its Resistance to Icebreaker Passage. *Problems Artiki i Atarktik*i. Vol.22.

Kashteljan, V.I., Poznyak, I.I., & Ryvlin, A.Ya., 1968. *Ice resistance to motion of a ship*. Sudostroyeniye, Leningrad.

Kerr, A.D., 1975. *The Bearing Capacity of Floating Ice Plates Subjected to Static or Quasistatic Loads, a Critical Survey*, Research Report, Vol. 333. Cold Regions Research and Engineering Laboratory, Hanover, New Hampshire, USA.

Korea Research Institute of Ships and Ocean Engineering (KRISO), 2015. *Model Tests in Brash Ice For Ice Class 1B and 1A for a Hanjin 1,900 TEU Container Carrier,* Daejeon: KRISO.

Kotras, T.V., Baird, A.V., & Naegle, J.W., 1983. Predicting ship performance in level ice. *Society of Naval Architects and Marine Engineers (SNAME) Transactions*, Vol. 91, pp. 329-349.

Lewis, J.W., & Edwards, R.Y. Jr., 1970. Methods for predicting icebreaking and ice resistance characteristics of icebreakers. *Society of Naval Architects and Marine Engineers (SNAME) Transactions*, Vol. 78, pp. 213-249.

Lewis, J.M, Bulat, V., Glen, I.F., & Kotras, T., 1983. *A semi-empirical ice resistance model,* Vol. 1 Main Report.

Lindqvist, G., 1989. A straightforward method for calculation of ice resistance of ships. *Proceedings of 10th International Conference on Port and Ocean Engineering under Arctic Conditions* (POAC), Lulea, Sweden, 12-16 June 1989, pp. 722-735.

Lau, M., Molgarrd, J., Williams, F.M., & Swamidas, A.S.J., 1999. An Analysis of Ice Breaking Pattern and Ice Piece Size around Sloping Structures. *Proceedings of the 11st International Conference on Port and Ocean Engineering under Arctic Conditions* (POAC).

Liu J.C. Lau, M., & Williams, F.M., 2006. Mathematical Modeling of Ice-Hull Interaction for Ship Maneuvering in Ice Simulations. *International Conference and Exhibition on Performance of Ships and Structures in Ice* (IceTech) 06-126-RF, pp. 1-8.

Liu, J., 2009. *Mathematical modeling ice-hull interaction for real time simulations of ship manoeuvring in level ice*. Ph.D. Memorial University of Newfoundland, Newfoundland, NL, Canada.

Lubbad, R., & Løset, S., 2011. A numerical model for real-time simulation of ship-ice interaction. *Cold Regions Science and Technology*, Vol. 65, pp. 111-127.

Lee, T.K., Lee, J.H., Kim, H., & Rim, C.W., 2013. Field measurement of local ice pressures on the ARAON in the Beaufort Sea. *International Journal of Naval Architects and Ocean Engineering*, 3, pp. 208-215.

Milano, V.R., 1973. Ship resistance to continuous motion in ice. *Society of Naval Architects and Marine Engineers (SNAME) Transactions*, Vol. 81, pp. 274-306.

Martio, J., 2007. *Numerical simulation of vessel's maneuvering performance in uniform ice. Informally published manuscript*, Ship Laboratory, Helsinki University of Technology, Espoo, Finland. pp. 1-30.

Naegle, J.N., 1980. *Ice-resistance prediction and motion simulation for ships operating in the continuous mode of icebreaking*. Ph.D. Thesis, University of Michigan.

Noble, P., Tam, W.K., Menon, B., & Bayly, I.M., 1979 Ice Forces and Accelerations on a Polar Class Icebreaker. *Proceedings of the 5th International Conference on Port and Ocean Engineering under Arctic Conditions* (POAC).

Noble, P., & Bulat, W., 1981. Icebreaker Bow Form-A Parametric Variation. *Proc. Society of Naval Architects and Marine Engineers (SNAME). Ice Tech.*

Popov, Yu., Faddeyev, O., Kheisin, D., & Yalovlev, A., 1969. *Strength of Ships Sailing in Ice*. Leningrad: Sudostroenie Publishing House. pp.227.

Riska, K., Wilhelmson, M., Englund, K., & Leiviskä, T., 1997. *Performance of merchant vessels in the Baltic,* Research report no 52. Espoo: Helsinki university of technology, ship laboratory, Winter Navigation Research Board.

Spencer, D., & Jones, S.J., 2001. Model-scale/full-scale correlation in open water and ice for canadian coast guard "R-Class" icebreakers.

Journal of Ship Research, 45(4), pp. 249-261.

Sawamura, J., Riska, K., & Moan, T. (2009). Numerical simulation of breaking patterns in level ice at ship' s bow. P*roceedings of the 19th International Offshore and Polar Engineering Conference* (ISOPE), Osaka, Japan, pp. 600–607.

Sawamura, J., Tsuchiya, H., Tachibana, T., & Osawa, N. (2010). Numerical modeling for ship maneuvering in level ice, *Proc. of the 20th IAHR international symposium on ice. 2010.*

Su, B., Riska, K., & Moan, T., 2010. A numerical method for the prediction of ship performance in level ice. *Cold Regions Science and Technology*, 60(3), pp. 177-188.

Tan, X., Su, B., Riska, K., & Moan, T., 2013. A six-degrees-of- freedom numerical model for level ice-ship interaction, *Cold Regions Science and Technology*, Vol. 92, pp. 1-16.

Vance, G.P., 1975. A scaling system for ships modelled in ice. *Proc. Society of Naval Architects and Marine Engineers (SNAME). Ice Tech. Symposium*, Montreal, Paper H1, 28pp.

Valanto, P., 2001. The resistance of ships in level ice. *Society of Naval Architects and Marine Engineers (SNAME) Transactions*, Vol. 109, pp. 53–83.

Varsta, P., 1983. *On the mechanics of ice load on ships in level ice in the Baltic Sea*. Ph.D. Thesis, Technical Research Centre of Finland, Espoo, Finland.

White, R.M., 1970. Prediction of icebreaker capability. *Royal Institute of Naval Architects (RINA) Transaction*, Vol. 112, No. 2, pp. 225-251.

Wang, S., 2001. *A dynamic model for breaking pattern of level ice by conical structures*. Ph.D. Thesis, Department of Mechanical Engineering, Helsinki University of Technology, Finland.

Yamaguchi, H., Suzuki, Y., Uemura, O., Kato, H., & Izumiyama, K., 1997, Influence of Bow Shape on Icebreaking Resistance in Low Speed Range. *Proceedings of the 16th International Conference on Ocean, Offshore and Arctic Engineering* (OMAE), Vol. 4, pp. 51-61.

Zhou, L., Riska, K., Moan, T., & Su, B., 2013. Numerical modeling of ice load on an icebreaking tanker: comparing simulations with model tests. *Cold Regions Science and Technology*, Vol. 87, pp. 33-46.

Appendix A. Photographs of Icebreaking Patterns for Icebreaking Model Ships

Photograph of Icebreaking Pattern	
Test No. 1	Hull Form 1

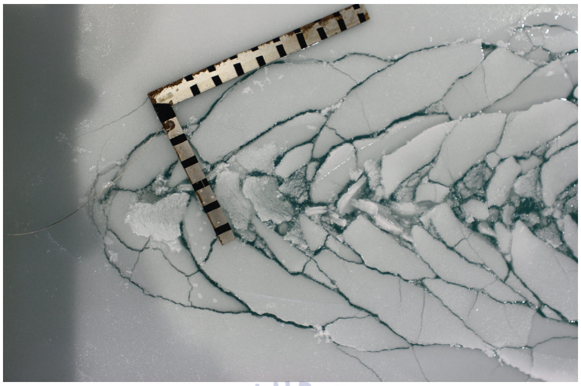

0.238 m/s

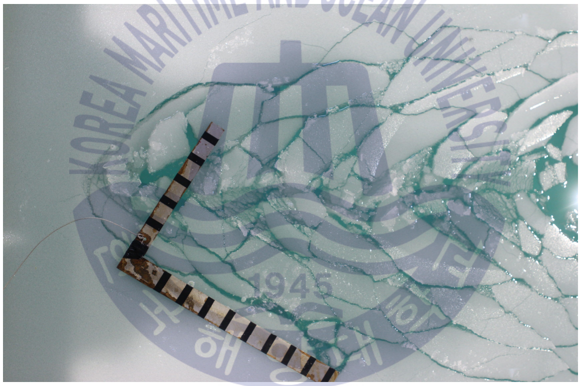

0.357 m/s

0.476 m/s

Photograph of Icebreaking Pattern	
Test No. 2	Hull Form 1

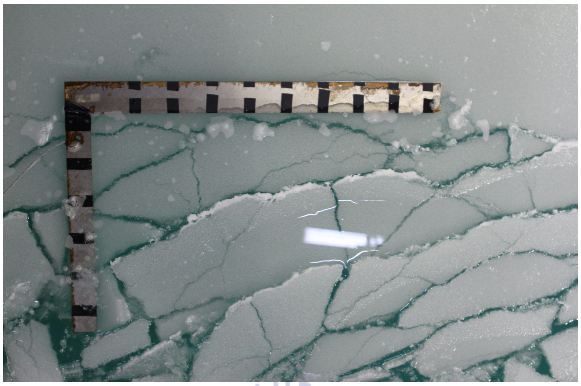

0.238 m/s

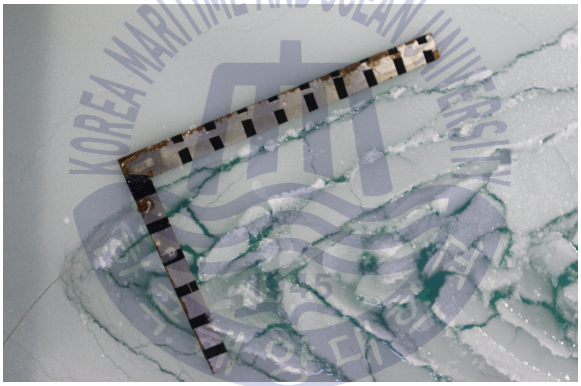

0.357 m/s

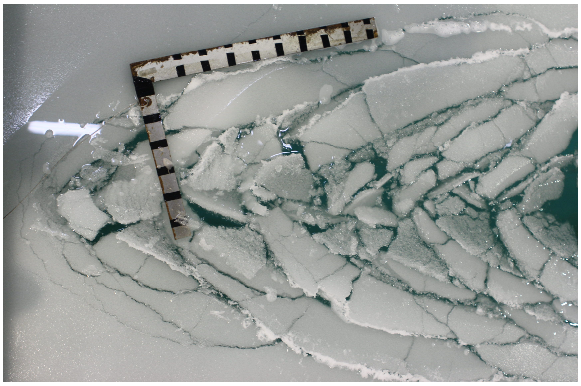

0.476 m/s

Photograph of Icebreaking Pattern	
Test No. 3	Hull Form 1

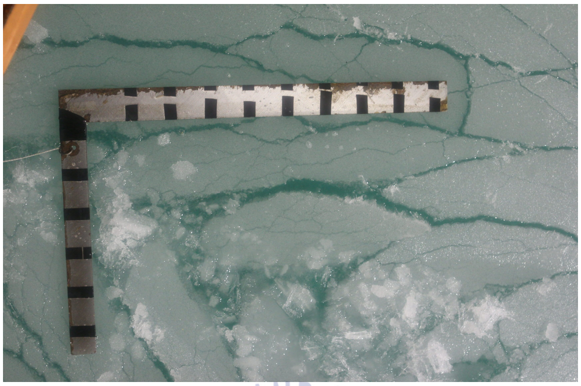

0.238 m/s

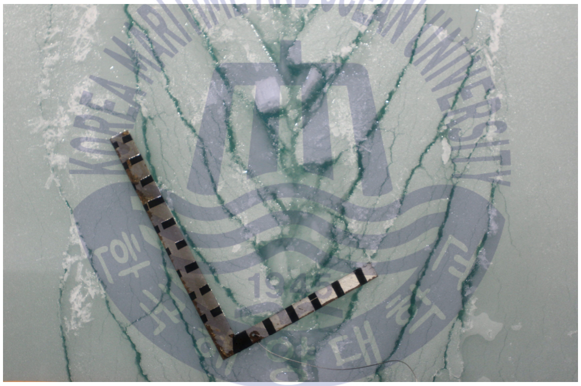

0.357 m/s

0.476 m/s

Photograph of Icebreaking Pattern	
Test No. 4	Hull Form 1

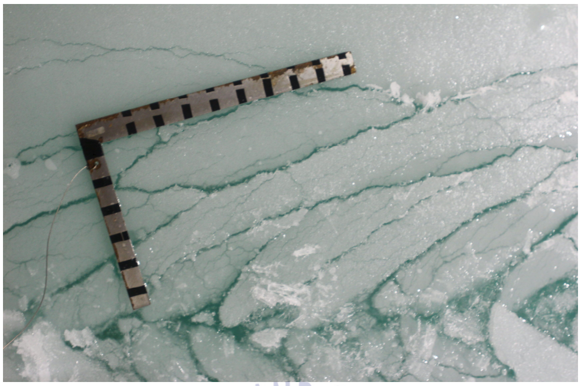

0.238 m/s

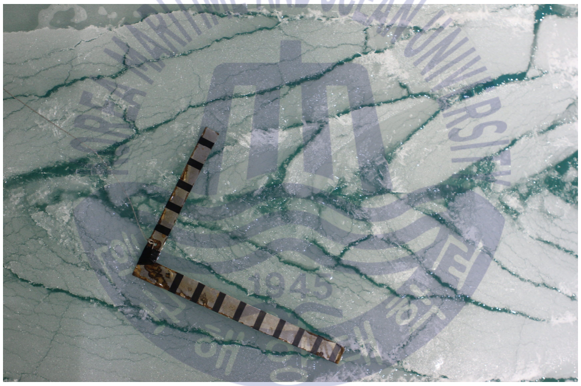

0.357 m/s

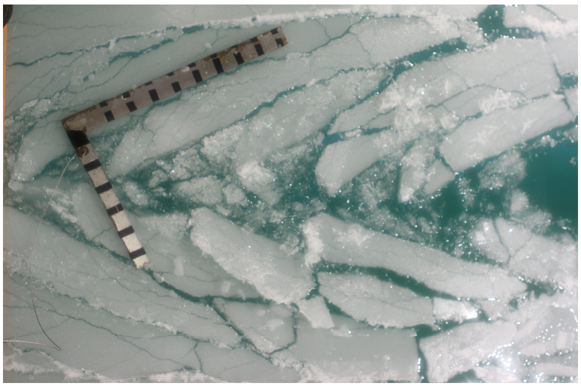

0.476 m/s

Photograph of Icebreaking Pattern	
Test No. 5	Hull Form 1

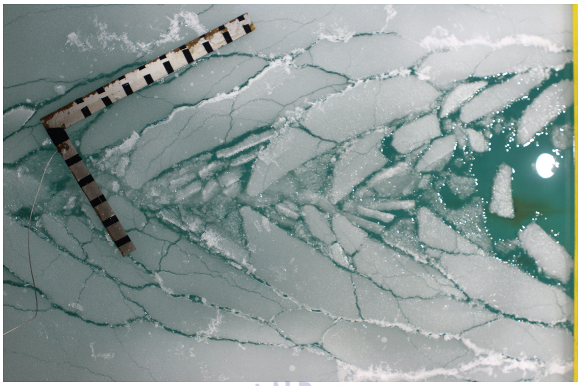

0.238 m/s

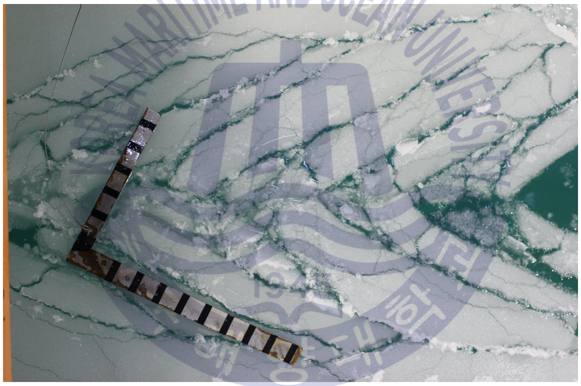

0.357 m/s

0.476 m/s

Photograph of Icebreaking Pattern	
Test No. 6	Hull Form 2

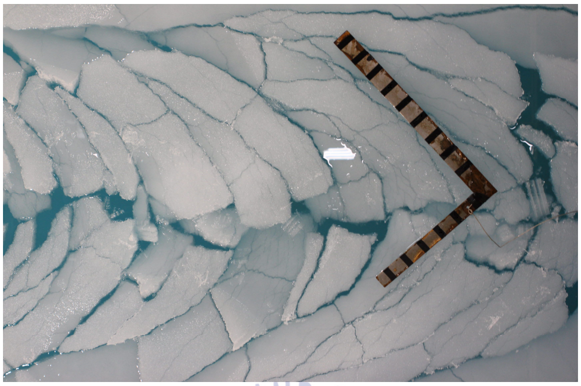

0.116 m/s

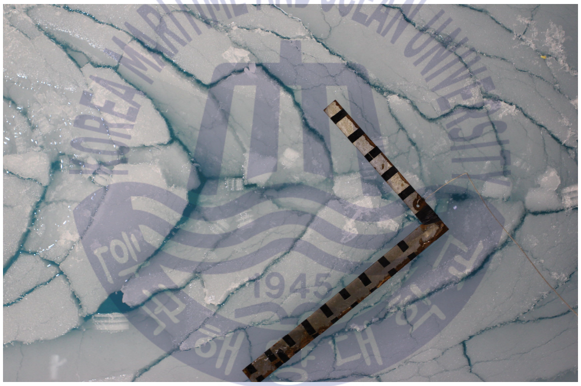

0.349 m/s

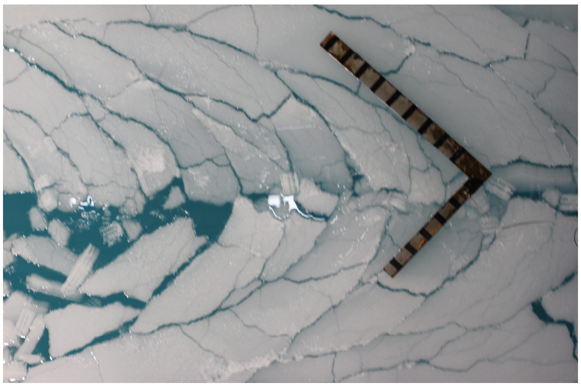

0.581 m/s

Photograph of Icebreaking Pattern	
Test No. 7	Hull Form 3

0.138 m/s

0.211 m/s

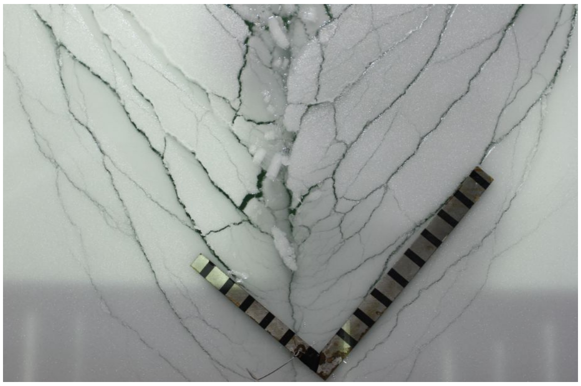

0.289 m/s

Appendix B. Difference between KRISO Method and HSVA Method in Correction

Difference Between KRISO Method and HSVA Method in Correction	
Test No. 1 (Hull Form 1)	Test No. 2 (Hull Form 1)

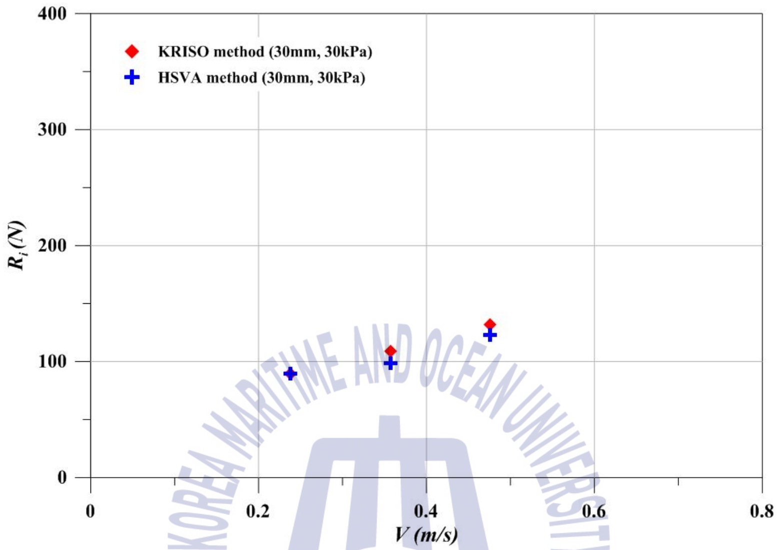

Test No. 1

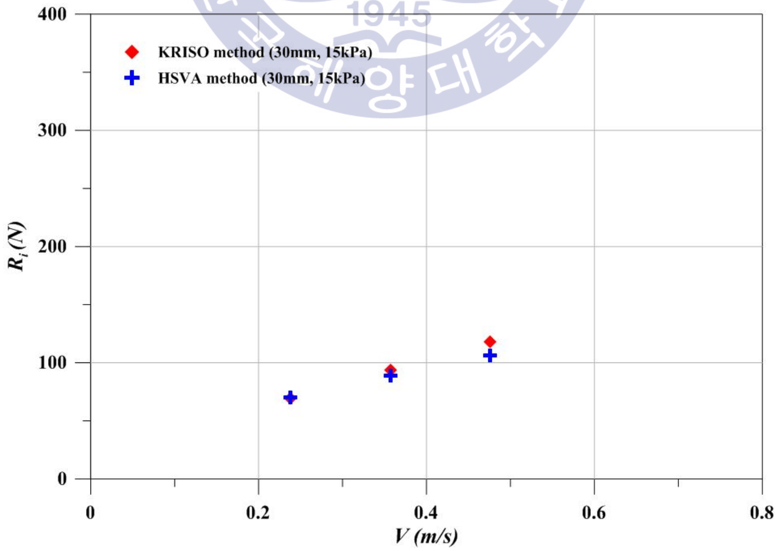

Test No. 2

Difference Between KRISO Method and HSVA Method in Correction	
Test No. 3 (Hull Form 1)	Test No. 4 (Hull Form 1)

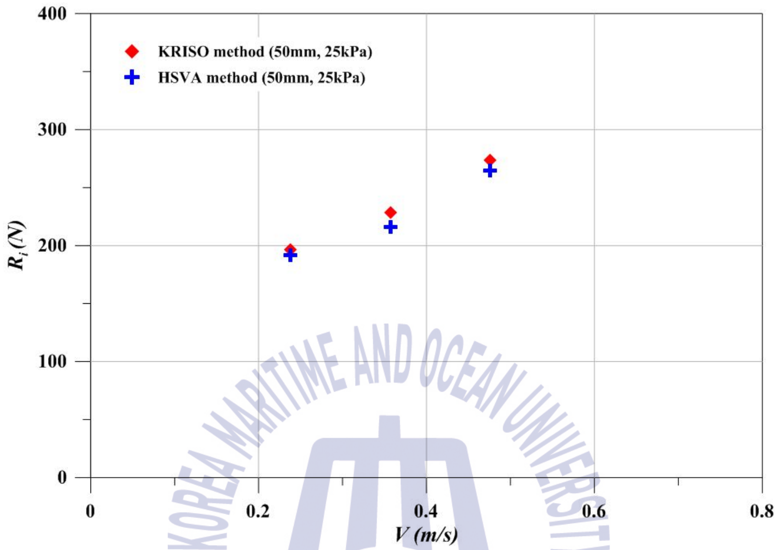

Test No. 3

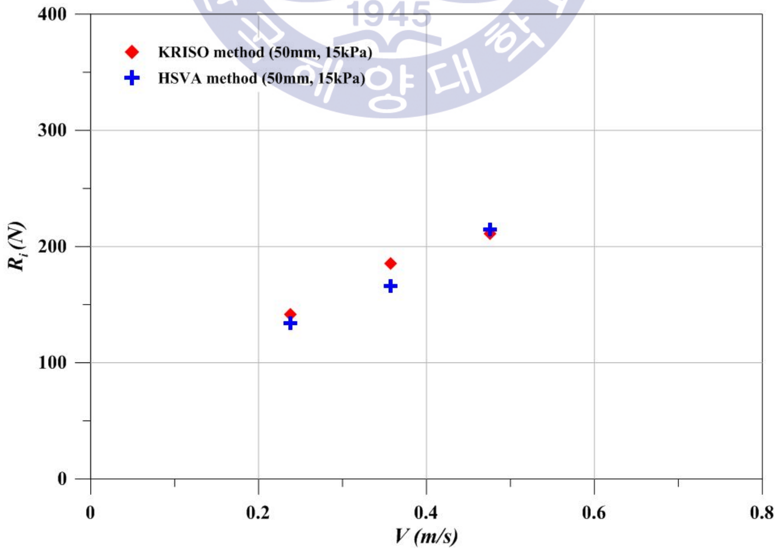

Test No. 4

Difference Between KRISO Method and HSVA Method in Correction	
Test No. 5 (Hull Form 1)	Test No. 6 (Hull Form 2)

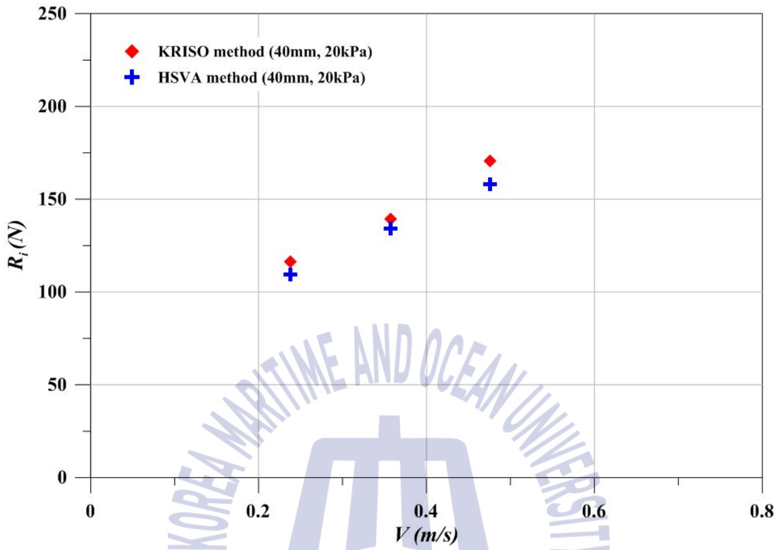

Test No. 5

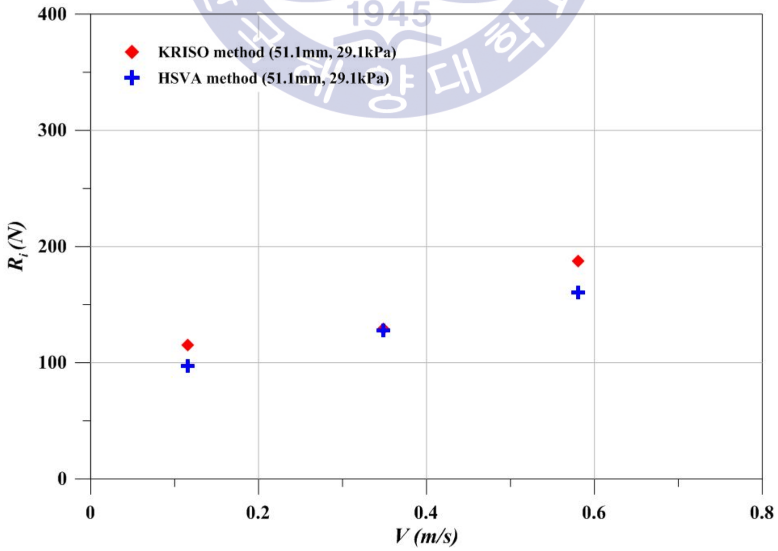

Test No. 6